UNIVERSITY OF COPENHAGEN
NIELS BOHR INSTITUTE, FACULTY OF SCIENCE

Mikkel Langgaard Lauritzen

# Modeling the Greenland Ice Sheet's Flow and Mass Loss From Past to Present

PHD THESIS

Niels Bohr Institute
University of Copenhagen

September 2024

this thesis has been submitted to the phd school of
the faculty of science, University of Copenhagen

**Thesis title:** Modeling the Greenland Ice Sheet's Flow and Mass Loss From Past to Present

**Author:** Mikkel Langgaard Lauritzen

**Supervisor:** Professor Christine Schøtt Hvidberg

**Assessment Committee:** Associate Professor Anders Svensson (chair)
University of Copenhagen

Professor Nanna Bjørnholt Karlsson
Geological Survey of Denmark and Greenland

Professor Heiko Goelzer
Norwegian Research Centre

**Name of department:** Physics of Ice, Climate and Earth, Niels Bohr Institute, Faculty of Science, University of Copenhagen

**Submitted on:** 11 October 2024

**Defended on:** Not available

**ISBN:** Not available

The work presented in this thesis is original and was conducted by Mikkel Langgaard Lauritzen during the PhD enrollment period from 2021–2024.

*In loving memory of my grandmother, Ruth.*

# Acknowledgments

This thesis is the culmination of three fantastic years in the Physics of Ice, Climate, and Earth (PICE) section at the Niels Bohr Institute, University of Copenhagen. It has been a roller coaster of an experience and I have so many people to thank for guiding me through this wonderful adventure.

First and foremost, I would like to express my profound gratitude to my supervisor, Christine, for taking me under her wing and introducing me to glaciology and ice sheet modeling. You have been enthusiastic and motivating throughout my PhD studies, always believed in me, and encouraged me to explore my own ideas. You taught me how to navigate in academia and your networking abilities are genuinely inspirational.

Secondly, I would like to thank Tollý for hosting my stay at the University of Iceland in Reykjavík during the autumn of 2022. You have been a wonderful host, and I must return for more glacier adventures and time in the geothermal pools.

From the blistering cold of drilling and processing ice cores, celebrated at every possible milestone with whiskey at EastGRIP, to solving differential equations and enjoying wine with Jesus at Karthaus, I am truly humbled and grateful for all the fantastic people in this field I have had the privilege to meet, a list too long to include here.

All my colleagues at PICE have made it a pleasure to come to work every day, and I would like to thank my office mates and the entire PhD cohort for sharing thoughts, ideas, and concerns. Special thanks go out to Niels and Grant for founding the PICyclE club. The bike rides we had were not always enjoyable, but they were indeed a unique type of fun.

I also want to thank all of my friends from outside of academia. The list is too long to include here, but thank you for giving me a break every once in a while by taking me skiing, running, cycling, playing football, or just out for a beer. You helped keep me sane during stressful times, and your friendship is invaluable to me. Special thanks to my flatmates, Luca, Magnus, Alex, Alex, and Rasmus, for cooking wonderful dinners and sharing many good times.

Finally, and most importantly, I would like to thank my entire family for your unwavering love and support. You mean the world to me, and I promise I will now have more time to visit. To my grandmother, who didn't see the end of my adventure, I dedicate this thesis to you.

Mikkel Langgaard Lauritzen

October, 2024

# Abstract

The Greenland Ice Sheet is currently losing mass at a rate that threatens to alter the state of the Arctic climate system and force coastlines around the world to retreat. This mass loss rate is expected to change in the future, as it has changed since the Last Glacial Maximum (LGM). During that period, the Greenland Ice Sheet was much larger, extending far beyond its present-day boundaries, while global sea levels were about 130 meters lower than they are today. Computational ice flow modeling provides a method to explore the evolution of the ice sheet across past, present, and future climate scenarios. These simulations are crucial due to their high societal relevance, such as providing accurate sea level rise predictions to secure coastlines effectively. This thesis contains three studies using the Parallel Ice Sheet Model (PISM) to improve the understanding of the Greenland Ice Sheet's dynamics and mass loss under different climate forcings.

In the first study, we investigate the influence of inter-annual temperature variability, which is expected to increase in the future, on the Greenland Ice Sheet mass loss. To do this, we force PISM with different realizations of the variability observed in the reanalysis data from NOAA-CIRES from 1851–2014. We find that including the inter-annual temperature variability causes the simulated steady-state ice sheet volume to decrease by 1.9±0.4 cm of sea level equivalent and by 11.5±1.4 cm when the variability is doubled. The sensitivity is most significant in the northern basins, where 40% of the total mass reduction takes place. Our results stress the need to include temperature variability in projections of future mass loss.

In a second study, we calibrate a positive degree day (PDD) model of PISM to the surface mass balance (SMB) of the regional climate model RACMO for the 1960-1989 climatology over Greenland. Using a Markov chain Monte Carlo algorithm we find that the PDD model successfully captures the Greenland-wide integrated SMB using uniform PDD parameters of $f_\mathrm{s} = 7.35 \pm 1.61$ mm $\mathrm{K}^{-1}$ $\mathrm{d}^{-1}$ and $f_\mathrm{i} = 10.21 \pm 2.65$ mm $\mathrm{K}^{-1}$ $\mathrm{d}^{-1}$ for snow and ice respectively. The inferred probability density function of PDD parameters is useful for long paleoclimatic simulations, where the mass balance varies with the ice sheet's topography.

In a third and final study, we investigate the Greenland Ice Sheet evolution from the LGM and throughout the Holocene period to the present day. Measurements of oxygen isotope ratios reveal substantial thinning at four different ice core sites throughout the last 11.7 ka comprising the Holocene period. We use these surface elevation histories to constrain an ensemble of 841 model simulations where we vary critical flow and climate forcing parameters to provide confidence in the modeled ice sheet evolution. We find that the Greenland Ice Sheet has contributed 5.3±0.3 m to the global mean sea level rise since the LGM. Furthermore, we find that the ice bridge that connected the Greenland Ice Sheet to the Innuitian Ice Sheet collapsed 4.9±0.5 ka ago and that the ice sheet is still responding to its Holocene deglaciation. This ongoing response has increased sea levels by 23±26 mm SLE $\mathrm{ka}^{-1}$ in the last 500 years, which should also be considered when making future mass-loss projections.

# Sammenfatning

Grønlands indlandsis mister i øjeblikket masse med en hastighed, der truer med at ændre tilstanden af det arktiske klimasystem og tvinge kystlinjer verden over til at trække sig tilbage. Denne massetabs rate forventes at ændre sig i fremtiden, som den har gjort det siden den sidste istids maksimum (LGM). I den periode var Grønlands indlandsis meget større og strakte sig langt ud over sine nuværende grænser, mens det globale havniveau var cirka 130 meter lavere end det er i dag. Modeller for isflydning tilbyder en metode til at udforske indlandsisens udvikling gennem fortidige, nutidige og fremtidige klimascenarier. Disse simuleringer er afgørende på grund af deres store samfundsmæssige betydning, som for eksempel at levere præcise forudsigelser af havniveaustigninger for effektivt at sikre kystlinjerne. Denne afhandling indeholder tre studier, der bruger Parallel Ice Sheet Model (PISM) til at forbedre forståelsen af Grønlands indlandsis' dynamik og massetab under forskellige klimapåvirkninger.

I det første studie undersøger vi indflydelsen af den årlige temperaturvariabilitet, som forventes at stige i fremtiden, på massetabet fra Grønlands indlandsis. For at gøre dette kører vi PISM med forskellige realiseringer af variabiliteten observeret i reanalyse data fra NOAA-CIRES fra 1851–2014. Vores resultater viser at inddragelse af den årlige temperaturvariabilitet fører til en reduktion i den simulerede steady-state isvolumen med 1,9±0,4 cm havniveauækvivalent, og med 11,5±1,4 cm når variabiliteten fordobles. Følsomheden er størst i de nordlige regioner, hvor 40% af den samlede masse reduktion finder sted. Vores resultater understreger behovet for at inkludere temperaturvariabilitet i forudsigelser af fremtidigt massetab.

I det anden studie kalibrerer vi PISM's positive grad-dags (PDD) model til overflade massebalancen (SMB) af den regionale klimamodel RACMO for klimatologien over Grønland fra 1960-1989. Ved brug af en Markov-kæde Monte Carlo-algoritme finder vi, at PDD-modellen succesfuldt simulerer SMBen integreret over Grønlands ved brug af uniforme PDD-parametre på $f_\mathrm{s} = 7,35 \pm 1,61$ mm K$^{-1}$ d$^{-1}$ og $f_\mathrm{i} = 10,21 \pm 2,65$ mm K$^{-1}$ d$^{-1}$ for hhv. sne og is. Den fundne sandsynlighedstæthedsfunktion for PDD-parametre er brugbar for lange paleoklimatiske simulationer, hvor massebalancen varierer med isens topografi.

I det tredje og sidste studie undersøger vi udviklingen af Grønlands indlandsis fra LGM og gennem hele Holocæn-perioden til nutiden. Målinger af oxygenisotopforhold viser at indlandsisen bliver betydelig tyndere ved fire forskellige iskerne-steder gennem de sidste 11,7 ka, som udgør Holocæn-perioden. Vi bruger disse overfladehøjdehistorier til at indsnævre et ensemble af 841 modelsimulationer, hvor vi varierer kritiske flyde- og klimaparametre for at styrke tilliden til den modellerede iskappeudvikling. Vores studie viser at Grønlands indlandsis har bidraget med 5,3±0,3 m til den globale gennemsnitlige havniveaustigning siden LGM. Desuden finder vi, at isbroen, der forbandt Grønlands indlandsis med den inuititiske iskappe, kollapsede for 4,9±0,5 ka siden, og at indlandsisen stadig reagerer på sin Holocæne klimahistorie. Denne fortsatte reaktion har forøget havniveauet med 23±26 mm SLE ka$^{-1}$ i de sidste 500 år, hvilket også bør tages i betragtning ved fremtidige forudsigelser af massetab.

# Contributions

The following three manuscripts which have been published, submitted, and are due to be submitted in an international scientific journal are presented in this thesis:

1. Mikkel Lauritzen, Guðfinna Aðalgeirsdóttir, Nicholas Rathmann, Aslak Grinsted, Brice Noël, and Christine S. Hvidberg (Aug. 9, 2023). "The Influence of Inter-Annual Temperature Variability on the Greenland Ice Sheet Volume". In: *Annals of Glaciology*, pp. 1–8. DOI: `10.1017/aog.2023.53`
2. Mikkel Lauritzen, Brice Noël, and Christine S. Hvidberg (in prep.). "Bayesian Calibration of a Positive Degree Day Model".
3. Mikkel Langgaard Lauritzen, Anne Munck Solgaard, Nicholas Mossor Rathmann, Bo Møllesøe Vinther, Aslak Grindsted, Brice Noël, Guðfinna Aðalgeirsdóttir, and Christine Schøtt Hvidberg (July 24, 2024). "Modeled Greenland Ice Sheet Evolution Constrained by Ice-Core-Derived Holocene Elevation Histories". In: *EGUsphere*, pp. 1–29. DOI: `10.5194/egusphere-2024-2223`

During my PhD I also contributed to the following manuscript when I was stationed at the East Greenland Ice-Core Project and although I had a lot of fun splicing fiber optics and planting geophones in the snow the resulting work is not presented in this thesis:

- Andreas Fichtner, Coen Hofstede, Brian L. N. Kennett, Niels F. Nymand, Mikkel L. Lauritzen, Dimitri Zigone, and Olaf Eisen (May 16, 2023). "Fiber-Optic Airplane Seismology on the Northeast Greenland Ice Stream". In: *The Seismic Record* 3.2, pp. 125–133. DOI: `10.1785/0320230004`

# Contents

# Chapter 1

# Introduction

Glacial ice is formed in areas where snow accumulation exceeds the amount of ablation (melt and sublimation) over many years. Year after year, as another layer of snow is added, the pressure of overlying snow increases, and the snow compactifies into ice. Eventually, the ice becomes so thick that it starts to slowly deform under its own weight, bringing ice from areas of accumulation to lower-lying areas of ablation. The biggest bodies of glacial ice are called ice sheets, intermediate-sized bodies are called ice caps or ice fields, depending on the underlying terrain, and the smallest are called glaciers.

Located in the North Atlantic Ocean, the Greenland Ice Sheet is the second largest body of ice on Earth with a global sea level rise potential of $7.42 \pm 0.05$ m including its peripheral glaciers (Morlighem et al., 2017). It covers 80% of Greenland's total land mass with an area of $1.8 \times 10^6$ km$^2$ and is up to 3.2 km thick at the interior. At its outlet glaciers, ice slides and accelerates to speeds of up to 50 meters a day (Joughin et al., 2020) and discharges into the ocean, where it calves off, accounting for approximately half of the ice sheet's mass loss today (The IMBIE Team, 2020; Fox-Kemper et al., 2021). The rest is lost through ablation.

Over millions of years, Earth has undergone periods of warming and cooling forced by changes in solar insolation and plate tectonic activity and amplified or reduced by various feedback mechanisms within the Earth system (Milanković, 1941). During the Quaternary ice age, constituting the last 2.6 million years, the Earth is believed to have been covered by ice at its poles with an ice extent that has varied in so-called glacial-interglacial cycles (Lisiecki and Raymo, 2005). About 1 million years ago, the pattern of glacial cycles changed from occurring roughly every 41,000 years to approximately every 100,000 years. The 41,000-year cycle corresponds closely with variations in Earth's axial tilt, while the 100,000-year cycle aligns with changes in Earth's orbital eccentricity. However, the precise connection between these orbital parameters and the timing of ice ages continues to be unclear (Raymo and Huybers, 2008). The latest transition occurred 11,700 years ago when the Last Glacial Period gave way to the current Holocene interglacial (Andersen et al., 2004). During this period, temperatures over Greenland increased until reaching a thermal maximum between 10,000 and 7,000 years ago. Subsequently, there was a long-term decreasing trend in temperatures that persisted until the industrial era (Vinther et al., 2009).

Currently, rapid rises in global temperature can be mainly attributed to an increase in atmospheric greenhouse gases (Gulev et al., 2021; Eyring et al., 2021). June 2024 marked a new high with the global mean temperature being 1.5 °C higher than that of the pre-industrial (1850-1900) level (Copernicus, 2024). In the Arctic, temperatures are increasing nearly four times as fast as the global level mean (Rantanen et al., 2022) and in response, glaciers and the Greenland Ice Sheet have retreated and thinned (Hugonnet et al., 2021; The IMBIE Team, 2020) and are projected to continue towards new equilibria at alarmingly fast rates (Hock et al., 2019; Goelzer et al., 2020) with some vanishing all together. As global warming progresses, it is expected to cause not only a rise in temperatures but also an increase in the frequency and intensity of extreme weather events, including both heatwaves and cold spells (Seneviratne et al., 2021). Such enhanced climate variability is likely to accelerate the melt rates of ice sheets even further (Mikkelsen et al., 2018; Beckmann and Winkelmann, 2023; Lauritzen et al., 2023).

Variations in Greenland Ice Sheet mass loss affect the temperature and salinity of the surrounding North Atlantic Ocean, initiating a complex interplay with the North Atlantic climate system. An increase in the ice sheet's melt rate could slow down the Atlantic meridional overturning circulation (Rahmstorf et al., 2015) or potentially even force it to collapse (Ditlevsen and Ditlevsen, 2023), which would further decrease sea surface temperatures. These reduced temperatures in the subpolar gyre south of Greenland have, in turn, been shown to impact the atmospheric circulation in the region (Gervais et al., 2019). Signals of climate variability, identified in ice cores (Vinther et al., 2003; Appenzeller et al., 1998), in turn affect the precipitation patterns over the Greenland Ice Sheet (Bjørk et al., 2018), thereby completing a feedback loop of interconnected mechanisms. Exactly how the melting and discharge of the Greenland Ice Sheet affect the climate in the North Atlantic region, and vice versa, remains a topic of active research.

To better understand the behavior of ice flow and its response to past and future changes in climate, ice sheet and glacier models have been developed. These models represent simplified versions of reality and vary in complexity from simple equilibrium models with no spatial resolution (e.g. Oerlemans, 2003) to complex thermo-mechanical, three-dimensional dynamical models. These advanced models are coupled with sub-models that include processes at the boundary, such as Earth deformation and interactions with the ocean and atmosphere. The increase in complexity comes at a cost: full three-dimensional models are computationally expensive and involve many parameters with complex nonlinear behavior. In recent years, thanks to a rise in computational resources, large ensembles of models have been run to quantify the uncertainty of model parameters. For instance, Edwards et al. (2019) revisit the marine ice cliff instability hypothesis of Pollard et al. (2015), quantifying the uncertainty in projections of future sea level rise.

Running large ensembles of models does not, however, ensure that the range of future model scenarios reflects our beliefs, as the models are not necessarily calibrated to observations (Aschwanden et al., 2021). Since the dawn of the satellite era, the amount of data available to constrain and validate ice sheet models has improved significantly. Satellite missions employing gravimetry and laser altimetry, combined with in-situ observations, provide estimates of mass loss (The IMBIE Team, 2020), while synthetic aperture radar offers high-resolution surface velocity estimates (e.g. Solgaard et al., 2021). Within the ice sheet, ground-penetrating radar maps the stratigraphy and the bedrock topography to constrain ice thickness (Morlighem et al., 2017), and borehole measurements reveal temperature profiles and heat fluxes at the base (e.g. Johnsen et al., 1995). With the increase in computational resources, integrating these datasets with ice sheet modeling is becoming ever more feasible. Recent advancements have been made to constrain ice sheet models to gravimetry-derived mass loss (Aschwanden and Brinkerhoff, 2022; Nias et al., 2023), refining projections of sea level rise and informing policy decisions related to climate adaptation.

Calibrating ice sheet models to recent mass losses comes with a risk of overlooking the ice sheet's long-term memory, though, and calls for proper calibration over longer time scales. Observational data used to constrain the ice sheet prior to the advent of satellite technology have been limited. However, evidence for past glaciations has been gathered from various geological features such as moraine lines, which mark the former edges of the ice sheet (Lesnek et al., 2020; Leger et al., 2024). Furthermore, deep ice cores carrying isotopic signals — traditionally used to derive past climates — have also been shown to contain information about historical ice sheet surface elevations (Vinther et al., 2009). Additionally, present-day uplift rates resulting from glacial isostatic adjustment indicate past variations in ice mass, which can further constrain ice sheet evolution (Schumacher et al., 2018). With the increase in computational power and the availability of longer timescale constraints, the time appears ripe for paleoclimatic calibrations of the Greenland Ice Sheet (Lauritzen et al., 2024).

## 1.1 Aim and outline

The aim of this PhD thesis is to improve our understanding of the melt and flow dynamics of the Greenland Ice Sheet in response to present-day and Holocene climate forcings, utilizing a state-of-the-art ice sheet model.

The thesis begins with an introductory review in chapter 2, which covers the fundamentals of ice flow modeling and the Bayesian inference and sampling techniques employed for model calibration. Chapter 3 presents the first manuscript, exploring the impact of inter-annual temperature variability on the steady-state volume and projected mass loss of the Greenland Ice Sheet. The second manuscript, presented in chapter 4, focuses on calibrating a positive degree day model to match the surface mass balance of Greenland. The third manuscript, which constitutes the main body of this thesis, is presented in chapter 5, detailing the calibration of the Greenland Ice Sheet model throughout its Holocene history using elevation reconstructions from ice cores. Finally, the insights gained from the free projects is discussed in chapter 6, followed by a final conclusion that synthesizes my three years of research in chapter 7.

# Chapter 2

# Background

This chapter introduces the basics of computational ice sheet modeling. First, the conservation laws of the continuum model are introduced, and then the rheology of ice, which relates the rate of deformation to the applied forces, is discussed. Next, the boundary conditions needed to determine the ice flow are explored before the often-used shallow approximations are introduced. The chapter then goes through the evolution of the ice flow, and its coupling to the atmosphere, ocean, and underlying deforming earth. Finally, the chapter goes through the basics of Bayesian inference and the statistical tools we use to infer the best model parameters from observations to increase the predictive skill of ice sheet modeling.

## 2.1 Ice flow modeling

On the microscopic scale, ice is composed of a discrete number of ice crystals, which in turn are made out of water molecules. At this level, it is the hydrogen bonds that hold the ice together, while the gravitational force drives it apart. On the macroscopic level of glacial-sized ice, however, we are much less interested in the behavior of individual grains of ice and more interested in the bulk behavior. At this scale, we can consider the ice to be smooth and approximate it as a continuum. Ice flow models are consequently formulated in the language of continuum mechanics and are based on the conservation of mass, momentum, and energy.

### 2.1.1 Conservation laws

Although ice is lost and gained at the boundary of the ice sheet, there are no sinks or sources within the ice. This conservation of mass is formulated in terms of the continuity equation,

$$\frac{\partial \rho}{\partial t} + \nabla \cdot (\mathbf{v}\rho) = 0, \tag{2.1}$$

where $\rho$ is the ice density and $\mathbf{v}$ is the flow velocity vector field. The density of ice changes throughout the firn layer as fresh snow, with a density of 50 kg $m^{-3}$, transitions into solid ice, with a density of approximately 917 kg $m^{-3}$ (Cuffey and Paterson, 2010). Assuming that the density is constant below the firn, the continuity equation becomes:

$$\nabla \cdot \mathbf{v} = 0. \tag{2.2}$$

In the continuum formulation, Newton's second law of motion, stating that linear momentum is conserved, becomes Cauchy's momentum equation,

$$\frac{D\mathbf{v}}{Dt} = \frac{1}{\rho}\nabla \cdot \boldsymbol{\sigma} + \mathbf{f}. \tag{2.3}$$

Here $\boldsymbol{\sigma}$ is Cauchy's stress tensor and $\mathbf{f}$ is the sum of body forces, while $\frac{D}{Dt}$ denotes the material derivative. Typical ice flow is characterized as slow or 'creeping' and the term on the left-hand side is much smaller than each of the terms on the right-hand side, i.e. the ice has a low Reynolds number. Consequently, the momentum balance becomes that of Stokes flow,

$$\nabla \cdot \boldsymbol{\sigma} = -\rho \mathbf{g}, \tag{2.4}$$

where the only macroscopic force acting on the ice is gravity and $\mathbf{g}$ is the gravitational acceleration.

Keeping track of the temperature distribution within the ice is important, as the rate of deformation increases as the temperature approaches the melting point. Furthermore, meltwater at the base of the ice acts as a lubricant and allows the ice to slide at speeds that are orders of magnitude faster than those due to internal deformation. The first law of thermodynamics states that the energy of a closed system is conserved. This together with Fourier's law of heat conduction yields the heat equation,

$$\rho c \frac{DT}{Dt} = \nabla \cdot (\kappa \nabla T) + \dot{W}_s + \dot{W}_L, \tag{2.5}$$

where $\kappa$ is the thermal conductivity, $c$ is the specific heat capacity, $\dot{W}_s$ is the heat generated from strain, and $\dot{W}_L$ is the latent heat from melt and refreezing of ice. The conduction of heat is slow and the advective term here cannot be neglected.

### 2.1.2 Rheology of ice

Rheology is the study of deformation and flow of matter. To determine the ice flow we need a constitutive relation relating the strain to the stress field. Through compression tests of polycrystalline ice, Glen (1952) established that ice behaves as a non-Newtonian fluid; the greater the stress, the softer it gets, similar to the deformation of metals close to their melting point. The rheology is usually assumed to be isotropic such that the deformation subject to a given stress is invariant under rotations within the ice. This assumption, together with the assumption that ice is incompressible, implies that the deformation only depends on the deviation from the isotropic stress (e.g. Nye, 1957). The deviatoric stress tensor is given by

$$\boldsymbol{\tau} = \boldsymbol{\sigma} + p\mathbf{1}, \qquad p = -\frac{1}{3}\operatorname{tr}\boldsymbol{\sigma}, \tag{2.6}$$

where $p$ is the isotropic pressure and $\mathbf{1}$ is the identity matrix. The non-linear dependence on the applied stress can then be captured by the Nye-Glen power law,

$$\dot{\boldsymbol{\varepsilon}} = A\tau_e^{n-1}\boldsymbol{\tau}, \qquad \tau_e^2 = \frac{1}{2}\operatorname{tr}\boldsymbol{\tau}^2. \tag{2.7}$$

Here $\tau_e$ is the effective stress or the second invariant of the stress tensor and $\dot{\boldsymbol{\varepsilon}}$ is the strain rate tensor whose components are derivatives of the flow velocity,

$$\varepsilon_{ij} = \frac{1}{2}\left(\partial_i v_j + \partial_j v_i\right). \tag{2.8}$$

With the strain rate tensor at hand, the heat generated from strain can be written $\dot{W}_s = \operatorname{tr}\boldsymbol{\tau}\dot{\boldsymbol{\varepsilon}}$. The creep exponent $n$, which determines the non-linearity of the flow, and the rate factor $A$ are usually deduced through laboratory measurements and field observations. For inferring the deviatoric stress from observed velocities and for computational purposes, the inverse relation of eq. 2.7 is sometimes useful,

$$\boldsymbol{\tau} = 2\eta\dot{\boldsymbol{\varepsilon}}, \qquad \eta = A^{-1}\dot{\varepsilon}_e^{\frac{1}{n}-1}, \qquad \dot{\varepsilon}_e^2 = \frac{1}{2}\operatorname{tr}\dot{\boldsymbol{\varepsilon}}^2, \tag{2.9}$$

where $\eta$ is the viscosity and $\dot{\varepsilon}_e$ the effective strain.

The initial experiments of Glen (1952) indicated a creep exponent of $n = 4$, but more measurements updated his estimate to $n = 3.2$ (Glen, 1955) and the value of $n$ has been a source of discussion within the literature ever since. Values from 2-4 have been measured and inferred from observations, with many studies citing $n = 3$ to be the value that fits observed deformation best (Cuffey and Paterson, 2010).

More recent laboratory experiments reveal, however, that the deformation rates of ice cannot be accurately captured by a constitutive relation as simple as eq. 2.7 over a wide range of applied stresses. Goldsby and Kohlstedt (2001) identify four different mechanisms responsible for the deformation of ice; diffusion, basal sliding, grain boundary sliding, and dislocation. The deformation due to each of these mechanisms can then be described by flow laws of the type of eq. 2.7 with creep exponents from 1 to 4. The total rate of deformation given by $\dot{\boldsymbol{\varepsilon}} = \dot{\boldsymbol{\varepsilon}}_{\text{diff}} + (\dot{\boldsymbol{\varepsilon}}_{\text{basal}}^{-1} + \dot{\boldsymbol{\varepsilon}}_{\text{gbs}}^{-1})^{-1} + \dot{\boldsymbol{\varepsilon}}_{\text{disl}}$ then match the measured rates with a much better agreement over a wide range of applied stresses. A recent study by Kuiper et al. (2020) find that grain boundary sliding with a creep exponent of $n = 1.8$ cannot be ignored at the NEEM ice core while Ranganathan and Minchew (2024) find that the dominant mechanism of deformation in fast-flowing ice streams and sheets is dislocation creep with a creep exponent of $n = 4$.

The rate factor, $A$, is found to vary orders of magnitude with the temperature, hence the need to keep track of the temperature field. It is usually taken to obey an Arrhenius relationship,

$$A = A_0 \exp\left(-\frac{Q}{RT^*}\right), \tag{2.10}$$

where $Q$ is the creep activation energy, $R$ is the gas constant, and $T^*$ is the pressure adjusted temperature. Usually, two values of $Q$ are used, $Q^+$ and $Q^-$, as ice becomes much softer with an increase in temperature above $-10\,^\circ\mathrm{C}$ most likely due to increased grain boundary sliding when ice starts to "premelt" (Cuffey and Paterson, 2010). Apart from dependence on temperature, the rate factor has been found to vary with grain size, water content, number of impurities, and ice crystal orientation (Lliboutry and Duval, 1985). In glacier-sized ice flow modeling it is, however, yet infeasible to account for all these dependencies at once. An enhancement factor, $E$, is usually added to eq. 2.10 and tuned to make up for this (Cuffey and Paterson, 2010).

### 2.1.3 Boundary conditions

To close the set of equations governing the ice flow, we need to supply suitable boundary conditions. At the top surface of the ice there is only negligible pressure from the atmosphere and if the ice is terminating into the ocean, the stresses are balanced by the hydrostatic pressure from the ocean, i.e.

$$\boldsymbol{\sigma} \cdot \mathbf{n} = \begin{cases} \mathbf{0} & \text{At the ice-atmosphere interface} \\ \rho_w g z \mathbf{n} & \text{At the ice-ocean interface} \end{cases}, \tag{2.11}$$

where $\mathbf{n}$ is normal vector to the surface, $\rho_w$ is the water density, and $z$ is the water depth.

At the base of the ice sheet, the story is a bit more intricate where the basal stresses are balanced by friction. Basal movement of the ice is usually either attributed to the ice sliding on top of a "hard bed" or to basal till deformations within a "soft bed", which carries the overlying ice with it. As the bottom of the ice is unfortunately mostly inaccessible to us, several sliding laws have been devised to form a relation between the properties of the basal till, the basal stress, and the resulting slip, which is the combined effect of sliding and till deformation. One commonly used slip law is the pseudo-plastic power law,

$$\boldsymbol{\tau_b} = \tau_c u_{\mathrm{th}}^{-q} |\mathbf{v}_{\mathrm{b}}|^{q-1} \mathbf{v}_{\mathrm{b}}, \tag{2.12}$$

where $\boldsymbol{\tau_b}$ is the tangential component of the normal force and $q$ is the sliding exponent. The yield stress, $\tau_c$, might then be fitted to achieve a good fit with the observed surface velocity, but the parameter reflects the physical properties of the bed that may vary with time. Instead, the yield stress is found to satisfy the Mohr-Columb rule (Cuffey and Paterson, 2010),

$$\tau_c = \tan(\phi) N_{\mathrm{till}}. \tag{2.13}$$

Here $\phi$ is the till friction angle which varies between 10° and 40° and reflects the differences in clay contents of the till. The effective pressure on the till $N_{\mathrm{till}}$ depends on the saturation of the

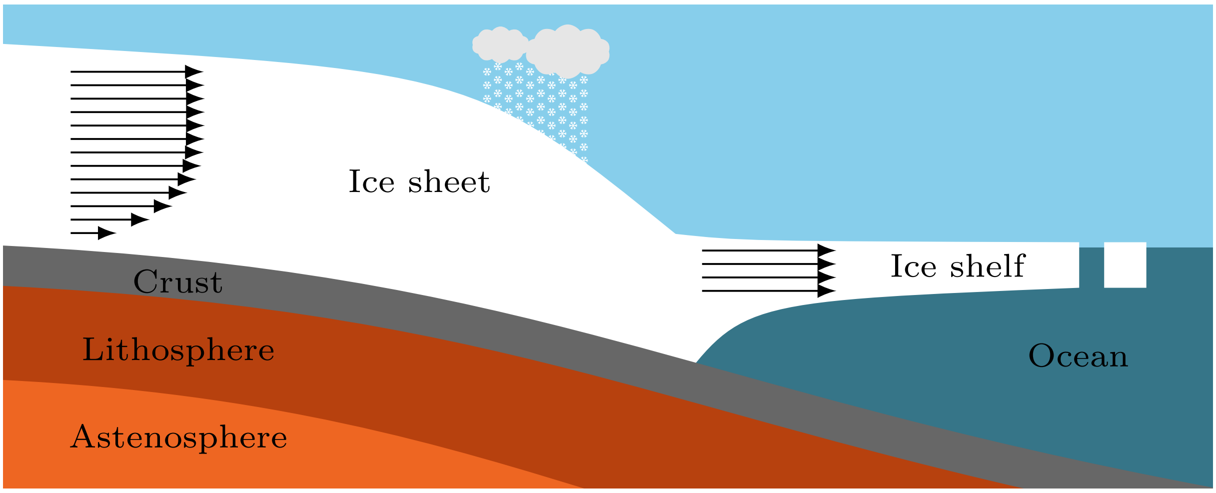

**Figure 2.1:** Schematic cross section depicting an ice sheet viscously deforming under its own weight. In the interior, where the SIA applies, the ice is frozen to the ground, and the driving stress is locally balanced by horizontal shearing. As the ice approaches the margin, it begins to slip, and longitudinal membrane stresses become increasingly dominant, making the SSA the more valid approximation. In the ice shelf section, basal drag is absent and the driving stress is balanced by longitudinal stress gradients and the hydrostatic pressure exerted by the ocean. The base of the grounded ice sheet rests on a crust of varying friction, which overlies the lithosphere and asthenosphere that deforms visco-elastically over centuries to millennia.

till and the overburden pressure of the ice (Bueler and van Pelt, 2015).

For the temperature field, eq. 2.5 is solved by applying a Dirichlet boundary condition at the surface, specifying the temperature, while a Neumann boundary condition is used at the base of the lithosphere, specifying the heat flux.

### 2.1.4 Shallow approximations

In principle, the Stokes equations (2.4) together with the constitutive relation (2.7) and appropriate boundary conditions (2.11,2.12) is enough to calculate the ice flow velocities for a given ice sheet configuration. However, solving the full Stokes equations for a continental-sized ice sheet is computationally demanding, especially for longer paleo simulations as four three-dimensional fields $(v_x, v_y, v_z, p)$ have to be solved, and approximations to the stress balance are therefore often applied to lighten these demands. These approximations rely on the small aspect ratio of ice sheets as the thicknesses of the Greenlandic and Antarctic ice sheets are small compared to their horizontal extents.

The most fundamental approximation used is the hydrostatic approximation. It assumes that the horizontal derivatives of the vertical shear stresses are small compared to the vertical derivative of the vertical normal stress, i.e. $\partial_x \sigma_{xz}, \partial_y \sigma_{yz} \ll \partial_z \sigma_{zz}$. With this assumption, the vertical component of the stress balance can be vertically integrated to compute the pressure at a given height,

$$p = \tau_{zz} + \rho g(s - z), \tag{2.14}$$

with $s$ being the surface elevation of the ice sheet where the pressure is assumed to be zero. The pressure can then be eliminated from the momentum balance, reducing the number of equations from three to two,

$$\underbrace{\partial_i \tau_{ji} + \partial_j \left(\tau_{xx} + \tau_{yy}\right)}_{\text{SSA}} + \underbrace{\partial_z \tau_{jz}}_{\text{SIA}} = \rho g \partial_j s, \qquad i, j \in \{x, y\}, \tag{2.15}$$

where the summation convention applies. This reduces the problem from four to three fields. Further assuming that the horizontal derivatives of the vertical velocities are small compared to the vertical derivatives of the horizontal velocities reduces the problem to solving two unknown fields $(v_x, v_y)$ and yields the Blatter-Pattyn approximations (Blatter, 1995; Pattyn, 2003). The right-hand side of eq. 2.15 is the driving stress of the ice flow; gradients in isostatic pressure caused by surface gradients and driven by gravity. The left-hand side are the forces needed to balance the driving stress. The dominant balancing forces differ within an ice sheet resulting in different types of flow (see Fig. 2.1).

The shallow ice approximation (SIA) assumes, apart from the Blatter-Pattyn approximations, that the membrane stresses (longitudinal and horizontal shear stresses) are negligible compared to the vertical shear stresses (Morland and Johnson, 1980). This is valid where ice is frozen to the bed and the deformation is dominated by the vertical shear[1].

Neglecting the horizontal gradients of eq. 2.15, the velocity can easily be solved locally for a column of ice using the inverse constitutive equation (2.9) and neglecting the horizontal derivatives of the vertical motion,

$$\mathbf{v}(z) - \mathbf{v}_b = -2(\rho g)^n \left|\nabla s\right|^{n-1} \nabla s \int_b^z \mathrm{d}z' A (s - z')^n, \tag{2.16}$$

where the velocity and the gradient are horizontal. The temperature dependence of the creep rate, $A$, requires the remaining integral to be solved numerically. The basal velocity $\mathbf{v}_b$ is usually assumed to be zero where the SIA is valid.

Complementary, the shallow-shelf/shelfy-stream approximation (SSA) assumes that the vertical shear is negligible compared to the membrane stresses (Morland, 1987; MacAyeal, 1989). This is valid in the ice shelves and the fast-flowing ice streams where the basal friction is small. Casting eq. 2.15 in terms of the velocity fields through the inverse constitutive equation (2.9) and vertically integrating yields

$$\partial_i \left(\bar{\eta} h (\partial_j v_i + \partial_i v_j)\right) + 2\partial_j \left(\bar{\eta} h (\partial_x v_x + \partial_y v_y)\right) + \tau_{b,i} = \rho g h \partial_j s, \qquad i, j \in \{x, y\}, \tag{2.17}$$

where $h$ is the local ice thickness, $\bar{\eta}$ is the depth-integrated viscosity and $\tau_{b,i}$ is the basal drag which can be replaced with an appropriate slip law like eq. 2.12. The horizontal gradients in the stress balance result in a non-local stress balance in the sense that the driving stress is balanced by ice speeding up and spreading or buttressing downstream.

---

[1] This is not valid within a few ice sheet thicknesses from the divide where vertical shearing is absent. Here the ice underneath the divide becomes very hard which results in observable Raymond bumps in radargrams where isochrones forms arches at the divide (Raymond, 1983; Conway et al., 1999).

With the SIA or SSA velocities now at hand, assuming that we can figure out how to solve the remaining differential equation (2.17), we can vertically integrate the continuity equation (2.2) to arrive at a prognostic equation for the evolution of a column of ice

$$\frac{\partial h}{\partial t} = -\nabla \cdot (h\bar{\mathbf{v}}) + b_s + b_b, \tag{2.18}$$

where $\bar{\mathbf{v}}$ is the depth-integrated velocity of either SIA or SSA and $b_s$ and $b_b$ are the mass balances at the surface and at the bottom respectively which we will also have to determine.

To take advantage of the two shallow approximations, Bueler and Brown (2009) devised a hybrid scheme in which they combined the depth-integrated velocities found using the non-sliding SIA and the SSA as a weighted average,

$$\bar{\mathbf{v}}_{\text{hybrid}} = f(|\bar{\mathbf{v}}_{\text{SSA}}|)\bar{\mathbf{v}}_{\text{SIA}} + (1 - f(|\bar{\mathbf{v}}_{\text{SSA}}|))\,\bar{\mathbf{v}}_{\text{SSA}}, \tag{2.19}$$

with weights given by

$$f(x) = 1 - \frac{2}{\pi}\arctan\left(\frac{x^2}{v_c^2}\right), \qquad v_c = 100\ \text{ma}^{-1}. \tag{2.20}$$

This ensures a smooth transition of the velocities, although Winkelmann et al. (2011) argued that a simple sum of the two solutions would also be smooth as each solution is already smooth. Other approximations to the Blatter-Pattyn model exist, each with its right and limitation (e.g. Robinson et al., 2022).

The heat equation (2.5) also has a shallow approximation as the horizontal temperature gradients are much smaller than the vertical. The horizontal conduction can therefore be neglected. The horizontal advection is however important as it transports colder ice from the interior to the warmer exterior parts (e.g. Cuffey and Paterson, 2010).

## 2.2 Mass balance processes

To determine the ice sheet evolution through time, we need to supply the prognostic equation (2.18) with specific mass balances at the surface and the base of the ice sheet.

### 2.2.1 Surface mass balance

At the surface of the ice sheet, mass is gained through accumulation (precipitation), lost through ablation (melt and sublimation), and transported by the wind in snow drifts. Some of the melted snow and ice flows in rivers on top of the ice sheet to the margin where it is lost or through big moulins. Some of the melt refreezes in the firn while some of it can be stored in big firn aquifers where it can even be stored throughout winter (Miller et al., 2022). Needless to say, correctly determining the surface mass balance is no easy task.

Although present-day surface mass balances can be derived from satellite radar altimetry, firn densification makes the mass balance estimates uncertain, and in-situ observations are needed to correct biases. Furthermore, radar altimetry does not tell us about mass balances in the future and in the past, for this we need models.

In general, the energy budget on the top of an ice sheet is made up of electromagnetic radiation from the sun and the snow and ice itself, heat transferred from the atmosphere through turbulent mixing close to the surface, and latent heat gained or lost when rain freezes or ice sublimates. Energy balance models try to model this energy exchange and calculate the melt, sublimation, and refreezing within the firn or on top of the ice. The reflectivity of electromagnetic waves (albedo) depends both on the frequency of the radiation and the condition of the ice or snow.

A regional climate model (RCM) can be used to simulate the precipitation, wind, and heat convection over an ice sheet given appropriate boundary conditions from a global general circulation model and can be coupled with an energy balance model (e.g. Noël et al., 2015).

The positive degree day (PDD) model provides the simplest way to model melt. It assumes that the net energy surface flux is simply proportional to the surface air temperature as if the atmosphere was a simple heat conductor and Fourier's law applied. Although this is not the mechanism for heat transfer, Braithwaite and Olesen (1989) found a correlation of 0.96 between measured ablation in West Greenland and the degree day index, $D$, defined by

$$D(\Delta t) = \int_{\Delta t} \mathrm{d}t T \max(T - T_m, 0), \tag{2.21}$$

where $\Delta t$ is the time interval of interest, $T$ is the temperature, $T_m$, is the melting point. The melt is then assumed proportional to the degree day index with different constants of proportionality for snow and ice, reflecting the difference in snow and ice albedo.

### 2.2.2 Basal mass balance

At the base of the ice sheet, the heat transferred from the underlying bedrock to the ice *is* by conduction. Additionally, heat is generated by the work done against the basal friction and transported by basal water flow which could be modeled although it's often neglected. When the base is at the pressure melting point, a positive energy balance results in melt while a negative one results in refreezing. A typical geothermal heat flux is about $50\,\mathrm{mW\,m^{-2}}$ which is about $3.5\times10^{-5}$ of the mean solar insolation and corresponds to $5\,\mathrm{mm\,a^{-1}}$ of temperate ice melt.

### 2.2.3 Sub shelf mass balance

Water exerts an upward buoyant force on ice, equal in magnitude to the downward gravitational force that would have been exerted on the water displaced by ice; this is Archimedes' principle. When the water depth increases above the height of ice displacing water the ice starts to float. That happens when

$$z_{\mathrm{sl}} - b > h\frac{\rho_i}{\rho_w}, \tag{2.22}$$

where $z_{\mathrm{sl}}$ is the sea-level height, and $\rho_i$ and $\rho_w$ are the density of ice and water respectively. Where the ice is floating, the base of the ice does not exchange heat with the bedrock but with the underlying lake or ocean instead. At equilibrium, the ice and water are at the freezing point while colder ice results in the freezing of water, and warmer water results in the melting of ice. The freezing point decreases with salinity and pressure while the density increases and typical sea water has a surface freezing point of $-1.8\,^{\circ}\mathrm{C}$.

Without any ocean currents, the pressure dependence causes ice to melt at the base of the ice shelf near the grounding line. The melted ice is buoyant freshwater that rises and refreezes at the surface. This process is known as the ice pump and draws in water masses causing an overturning circulation beneath the ice shelf (Lewis and Perkin, 1986). The amount of melt depends on the temperature and salinity of the open ocean water and the amount of meltwater routed from underneath the ice sheet, which amplifies the ice pump effect.

Ocean models capable of modeling this process do exist but require the ability to resolve narrow fjords and knowledge of the ocean temperature and salinity, which may in turn be modeled by an ocean circulation model (e.g. Olbers and Hellmer, 2010). Instead, simple empirical ocean melt parametrizations are sometimes used like that of Aschwanden et al. (2019) who based on observations varied ocean melt along Greenland's coast with latitude.

### 2.2.4 Calving

At the ice shelves, ice fractures and breaks off into icebergs in what is known as calving events when it is subjected to large stresses. The biggest calving events occur in Antarctica where icebergs as big as $11\,000\,\mathrm{km}^2$ have been observed (Slominska et al., 2012).

Accurately modeling calving would require modeling the evolution of rifts through fracture mechanics, but as this is a subgrid process, parametrizations using the ice-ripping stress field are often used.

Common calving laws include the eigen calving law in which the calving rate is assumed proportional to the product of the horizontal principal strain rates. However, this law predicts no or limited calving in the narrow fjords of Greenland, where the transverse principal strain is close to zero or negative (compressional). Instead, Morlighem et al. (2016) proposes a calving law in which the calving rate is proportional to the Von Mises stress and the velocity. This is unphysical in that it breaks with Galilean symmetry, but it produces realistic terminus withdrawal.

## 2.3 Earth deformation

In a crude description Earth consists of spherical layers; an atmosphere, an outer crust, a mantle, and a core, each of which can be subdivided and each with different rheologies[2] (e.g. Lowrie and Fichtner, 2020). The outer crust is a thin film of low-density rock that floats on top of a higher-

---

[2] The crust is made up, partly by the cryosphere; the name given to the joint masses of all ice including permafrost.

density mantle like an iceberg in water. Because the crust is buoyant, changes in load on the crust force it to respond by rising and sinking in what is known as isostatic adjustment.

The displacement of the mantle differs from that of water, and its rheology is less well-known. The upper mantle can be divided into two or more layers characterized by their response to stress. The upper part of the upper mantle, the lithosphere, is cold and solid and responds through elastic deformation and flexing, pushing the underlying asthenosphere away. Within the asthenosphere the rock is close to the melting point and deforms viscously, again analogous to ice. Because of the rigidity of the lithosphere, the response of a point load is distributed over a large lateral distance resulting in peripheral bulges. The amount and rate of isostatic adjustment depend on the viscosity of the asthenosphere and on the flexural rigidity of the lithosphere which in turn depends on its thickness and elastic properties. The timescale at which elastic and viscous deformation is comparable, known as the Maxwell time, is on the order of a few hundreds of years for the upper mantle (Peltier et al., 1981).

The lithosphere is believed to have deformed hundreds of meters in glacial isostatic adjustment since the last glacial and is still responding by rising up to $15\,\mathrm{mm\,a^{-1}}$ where the Laurentide Ice Sheet used to be (Schumacher et al., 2018). This deformation acts a as negative feedback to glacial retreat and can possibly explain the shape of the 100.000 year cycle observed in oxygen isotope records (Oerlemans, 1981).

## 2.4 Numerical solution of the equations

To solve the stress balance (2.4) time and space is discretized to solve the equations numerically. This is usually done by the finite difference method or the finite element method. In the finite difference method the differential operators are approximated using a Taylor expansion and evaluated on a grid turning the differential equations into algebraic equations which are then solved iteratively. In the finite element method, the solution is approximated rather than the differential operators. This starts with a partial integration of the stress balance equation (2.4) multiplied by a weight function to form a 'weak' formulation of the problem. The domain is then discretized, and a set of $N$ linearly independent test functions defined on this mesh is used to approximate the solution. This approach transforms the problem into $N$ linear algebraic equations, which are then solved algebraically to find the approximate solution.

### 2.4.1 PISM

Numerous ice sheet models that solve various orders of Stokes flow, using either the finite difference method or the finite element method, have been developed in recent decades and are freely available to use. For the studies presented in this thesis, we use the open-source Parallel Ice Sheet Model (PISM; Bueler and Brown, 2009; Winkelmann et al., 2011) to model the evolution of the Greenland Ice Sheet. PISM includes both a Blatter-Pattyn solver and a hybrid SIA-SSA solver. The SIA is solved for each grid point and given by eq. 2.16 while the SSA is solved either by the finite element method or by finite difference method using Picard iteration to solve the nonlinear system of algebraic equations. The hybrid SIA-SSA solution is then given by eq. 2.19. The time integration used in PISM is the explicit Euler scheme and an adaptive time step is used limited by both the SIA and the SSA solutions to ensure stability.

PISM is well suited for longer paleoclimatic simulations with changing ice sheet geometry as PISM uses a sub-grid parametrization of the grounding line, allowing grid cells to be partly filled such that there are no abrupt changes in basal friction and melt (Gladstone et al., 2010). Rather than solving the heat equation (2.5) directly, PISM tracks the enthalpy of the ice from which both the temperature and the liquid water fraction within the ice can be determined (Aschwanden et al., 2012). Additionally, PISM incorporates a two-layer earth deformation model, originally developed by Lingle and Clark (1985), and efficiently solves the linear differential equation for vertical displacement at the lithosphere-asthenosphere interface in Fourier space (Bueler et al., 2007).

PISM was installed on the Danish National Life Science Supercomputing Center, Computerome. The architecture of this high-performance computing cluster limits the efficiency of a single simulation distributed across multiple computational nodes. However, the architecture is ideal for large ensemble studies, enabling us to explore ice sheet simulations within a statistical framework.

## 2.5 Bayesian inference

This section provides a short review of Bayesian inference, for a more thorough description see e.g. Tarantola (2005) or Fichtner (2021). As outlined in the previous sections, the ice sheet evolution depends on the viscosity of ice, the basal friction, the mass balance, the Earth deformation as well as the initial state of the ice sheet. All of this is described by the full set of model parameters $\mathbf{m}$[3]. With our ice sheet model at hand, we are then able to determine the evolution of an ice sheet given the model parameters $\mathbf{m}$, i.e. we can solve the forward problem,

$$\mathbf{d} = G(\mathbf{m}). \tag{2.23}$$

Here $G$ is the forward model operator that simulates the ice sheet evolution given the model parameteres, m, and returns some observable, $\mathbf{d}$, which could be a time series of mass loss, bedrock uplift rates, surface velocities or something else. Given some observation it might then be interesting to find the model parameters that are consistent with this observation, i.e. finding a solution to the inverse problem,

$$\mathbf{m} = G^{-1}(\mathbf{d}). \tag{2.24}$$

Depending on the number of model parameters and observations and on the function $G$ the inverse problem might be non-unique. It might be an under-determined problem in which several model parameters will reproduce the observation or an over-determined problem in which no set

---

[3] The initial state of the ice sheet is not a model parameter per se, but will be treated like so in this section as it is no different in terms of influencing the observations.

of model parameters will be consistent with the observations and $G^{-1}$ does not exist. Even if $G^{-1}$ does exist, there is no guarantee it will be robust towards noisy data.

As any real-world observation comes with some uncertainty the nature of the inverse problem changes. The introduction of uncertainty invites us to treat the problem in terms of probabilities. We would like to know the probability density function of the model parameters conditioned on some uncertain observations. According to Bayes' theorem this *posterior* probability density function is given by

$$\rho(\mathbf{m}|\mathbf{d}^{\text{obs}}) = \frac{\rho(\mathbf{d}^{\text{obs}}|\mathbf{m})}{\rho(\mathbf{d}^{\text{obs}})}\rho(\mathbf{m}). \tag{2.25}$$

This is the solution to the inverse probabilistic problem inferred from the observations $\mathbf{d}^{\text{obs}}$. Here, $\rho(\mathbf{m})$ is the *prior* probability density function. It should contain all the information we know about the model parameters before making the observation. The choice of prior is inherently subjective and should be chosen with care as it can dominate the posterior for poorly constrained parameters. Usually there is always some knowledge of the parameters beforehand, such as their sign and magnitude or from previous independent inferences. Otherwise one might attempt to construct an uninformed prior although this is somewhat ambiguous. Naively, one might think that if the viscosity prior $\rho(\eta)$ is taken to be uniform within some range it would be uninformed. However, the prior of the inverse of the viscosity, the fluidity, $\rho(\eta^{-1})$ would then not be uniform and thus informed[4].

$\rho(\mathbf{d}^{\text{obs}}|\mathbf{m})$ is the *likelihood* and depends on the nature of the observations $\mathbf{d}^{\text{obs}}$. Often, the data is noisy and can be thought of as a random variable. The difference $\mathbf{d}^{\text{obs}} - G(\mathbf{m})$ will then also behave like a random variable and become a function of the model parameters $\mathbf{m}$. In this thesis the data is taken to be normally distributed and the likelihood takes the form

$$\rho(\mathbf{d}^{\text{obs}}|\mathbf{m}) = \frac{1}{\sqrt{(2\pi)^k \det \boldsymbol{\Sigma}}} \exp\left(-\frac{1}{2}(\mathbf{d}^{\text{obs}} - G(\mathbf{m}))^T \boldsymbol{\Sigma}^{-1}(\mathbf{d}^{\text{obs}} - G(\mathbf{m}))\right), \tag{2.26}$$

where $\boldsymbol{\Sigma}$ is the covariance matrix and $k$ is the size of $\mathbf{d}^{\text{obs}}$.

The denominator $\rho(\mathbf{d}^{\text{obs}})$ is known as the *evidence*. It is a scalar quantity that is usually disregarded as it only normalizes the posterior.

### 2.5.1 Sampling methods

Usually, we are less interested in the posterior distribution itself and more interested in the expectation value of some function of $\mathbf{m}$,

$$\mathrm{E}\left[f(\mathbf{m})\right] = \int_{\mathbb{M}} \mathrm{d}\mathbf{m} f(\mathbf{m})\rho(\mathbf{m}|\mathbf{d}^{\text{obs}}). \tag{2.27}$$

---

[4] Jeffry's prior aims to remedy this by being invariant under this transformation. It will however not be invariant under other transformations and is thus still subjective.

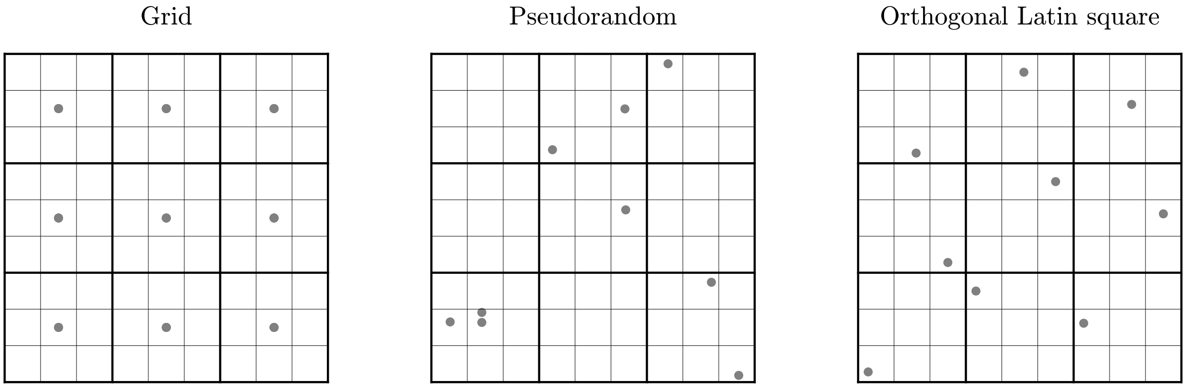

**Figure 2.2:** Three different sampling techniques within the unit square with 9 samples each. The Latin square sampling divides each univariate parameter space into intervals of equal probability. Orthogonal Latin square sampling further divides the joint parameter space into subspaces of equal probability.

This might be the expectation value of the parameters themselves or it could be the expectation value of $G$ or some other observable in the model. Determining this requires determining the likelihood for all model parameters in the parameter space $\mathbb{M}$. As $\mathbb{M}$ is usually an infinite set and $G$ does not have a closed-form expression, this is not possible and we need to estimate the posterior by drawing samples from $\mathbb{M}$.

When $G$ is sufficiently simple and computationally inexpensive, drawing a large number of random samples becomes feasible to estimate the posterior distribution; this process is known as Monte Carlo sampling. In Markov chain Monte Carlo (MCMC) sampling, the samples are generated in a sequence where each sample depends on the position of the previous one. The objective is that the distribution of the samples in the chain converges to the posterior distribution when the sequence equilibrates. The most famous algorithm in this category is the Metropolis-Hastings algorithm where a random walk in the parameter space is performed. Here, subsequent samples are either accepted or rejected based on the probability at that point compared to the previous point (Metropolis et al., 1953; Hastings, 1970).

When the model $G$ is sufficiently complex and requires several computation hours as in the case of ice sheet modeling, MCMC algorithms are not feasible and great care is needed in selecting the samples as they can be costly.

Latin hypercube sampling (LHS; McKay et al., 1979) is a stratified sampling technique that ensures a uniform exploration of the parameter space to reduce the variance in the estimates compared to random sampling if the integrand is monotone. In LHS each univariate parameter space is stratified into $n$ strata and the samples are then drawn such that there is one sample in each stratum for every dimension in the parameter space. This ensures that every parameter is sampled uniformly across its entire range to account for their main effect. This is especially efficient for high-dimensional sampling spaces where some parameters might explain a larger amount of the variance in $G$ than others; the stratification in the subspace of important parameters ensures that these are explored while the simultaneous stratification of the unimportant parameters makes little difference. Additionally, $r$-order orthogonal Latin hypercube sampling also stratifies each $r$-dimensional subspaces into $r$-dimensional strata, from which one sample is selected (Tang, 1993). This ensures that the sampling captures the multivariate effects of $G$, making it possible to pick out the main correlations. An example of a second order orthogonal Latin square with $n = 9$ samples can be seen in Fig. 2.2.

Lately, LHS has been extensively used in the literature to quantify the uncertainty of Ice flow modeling (e.g. Larour et al., 2012; Edwards et al., 2019; Aschwanden et al., 2019; Hill et al., 2021; Nias et al., 2023).

# Chapter 3

# Inter-annual temperature variability

This chapter contains the following paper:

Mikkel Lauritzen, Guðfinna Aðalgeirsdóttir, Nicholas Rathmann, Aslak Grinsted, Brice Noël, and Christine S. Hvidberg (Aug. 9, 2023). “The Influence of Inter-Annual Temperature Variability on the Greenland Ice Sheet Volume”. In: *Annals of Glaciology*, pp. 1–8. DOI: `10.1017/aog.2023.53`

which was received on 1 March 2023, revised on 19 May 2023, and accepted on 17 June 2023. The bibliography for the manuscript is included in the main bibliography at the end of the thesis.

# The influence of inter-annual temperature variability on the Greenland Ice Sheet volume

Mikkel Lauritzen[1], Guðfinna Aðalgeirsdóttir[2], Nicholas Rathmann[1],
Aslak Grinsted[1], Brice Noël[3], and Christine S. Hvidberg[1]

[1] *Niels Bohr Institute, University of Copenhagen, Copenhagen, Denmark*
[2] *Institute of Earth Sciences, University of Iceland, Reykjavík, Iceland*
[3] *Department of Geography, Laboratoire de Climatologie et Topoclimatologie, University of Liège, Liège, Belgium*

**Abstract**

The Greenland Ice Sheet has become an increasingly larger contributor to sea level rise in the past two decades and is projected to continue to lose mass. Climate variability is expected to increase under future warming, but the effect of climate variability on the Greenland Ice Sheet volume is poorly understood and is adding to the uncertainty of the projected mass loss. Here we quantify the influence of inter-annual temperature variability on mass loss from the Greenland Ice Sheet using the PISM model. We construct an ensemble of temperature-forcing fields that accounts for inter-annual variability in temperature using reanalysis data from NOAA-CIRES over the period 1851–2014. We investigate the steady state and transient response of the Greenland Ice Sheet. We find that the simulated steady-state ice sheet volume decreases by 1.9±0.4 cm of sea level equivalent when forced with a varying temperature forcing compared to a constant temperature forcing, and by 11.5±1.4 cm when the variability is doubled. The northern basins are particularly sensitive with a change in volume of 0.9–1.1%. Our results emphasize the importance of including temperature variability in projections of future mass loss.

## 1 Introduction

With about two-thirds of global mean sea level rise being due to ice mass loss in the period 1900–2018 and the rest being mainly attributed to thermal expansion (Frederikse et al., 2020; Fox-Kemper et al., 2021), the knowledge of future glacier and ice sheet mass loss is of utmost importance. The Greenland Ice Sheet holds an ice volume of 7.4 meters of global mean sea level equivalent (SLE) (Morlighem et al., 2017) and has contributed $10.8 \pm 0.9\,\mathrm{mm}$ to the mean sea level rise between 1992 and 2018, with 49.7% of the mass loss caused by dynamic discharge into the ocean and the rest by melt and runoff (The IMBIE Team, 2020; Fox-Kemper et al., 2021). Polar amplification has caused the Arctic to warm nearly four times as fast as the rest of the

Earth (Rantanen et al., 2022) and with the global temperatures expected to rise further due to increased anthropogenic forcing, the sea level contribution from the Greenland Ice Sheet will continue to increase in the coming centuries.

Global warming also induces increased variability of climate, including more extreme events of both warm and cold temperatures, which are expected to be more frequent in the future (Seneviratne et al., 2021). Increased climate variability is expected to cause the ice sheet to melt even faster than today (Mikkelsen et al., 2018; Beckmann and Winkelmann, 2023). Atmospheric warming causes the surface melting to increase when the temperature is above the freezing point, while a similar cooling would not affect the melting for temperatures below the freezing point. Consequently, a surface temperature varying around the freezing point will tend to cause the melting to increase and lead to net mass loss. However, the response of the ice sheet mass balance to increased temperature variability is complex and highly non-linear, and if the snow accumulation rate increases in warmer climates, higher variability could also result in a larger ice sheet (Albrecht et al., 2020a). An earlier study investigated this asymmetric response to temperature fluctuations using a simplified, perfectly plastic ice sheet model and concluded that the Greenland Ice Sheet would become 0.5–1 m SLE smaller when including the inter-annual temperature variability than without this variability (Mikkelsen et al., 2018). It is unclear what the influence of including temperature variability would be in a model of the Greenland Ice Sheet that includes ice dynamics and discharge. Most models in the Ice Sheet Modelling Intercomparison Project for the IPCC's sixth Assessment Report (ISMIP6) had a mass loss lower than the observed in the historical period below (Aschwanden et al., 2021), and in some cases, this was traced back to a lack of variability in the climate model forcing over the historical period (Goelzer et al., 2020). Another recent study found that the Greenland Ice Sheet volume decreased when extremely warm summers were included in the temperature forcing (Beckmann and Winkelmann, 2023), but the effect of cold spells was not included.

In this paper, we examine the effect of inter-annual variability in atmospheric temperatures on the present-day Greenland Ice Sheet geometry and volume by using a thermodynamically coupled three-dimensional ice sheet model to account for ice-dynamical feedbacks. Our goal is to revise the previous results for a simplified ice sheet model (Mikkelsen et al., 2018) by using a dynamic ice flow model with realistic geometry and mass balance forcing. This is needed to assess the importance of including climate variability in ice sheet simulations over the historical period and can inform efforts to develop a new protocol for projections of ice sheet mass loss in ISMIP7 (Aschwanden et al., 2021).

We construct an ensemble of temperature-forcing time series that mimics the mean annual temperature variability found in the NOAA-CIRES 20th Century Reanalysis (20CR), version 2c (Compo et al., 2011) following the method of Mikkelsen et al., 2018. We add this variability to the seasonal mean temperatures of the period 1960–1989 from the RACMO model (Noël et al., 2019). We then perform an ensemble of ice sheet simulations, where each ensemble member is forced with a corresponding temperature-forcing time series ensemble member. We compare this simulated ice sheet ensemble to a control run forced with constant climate without inter-annual temperature variability to assess the impact on the ice sheet volume, and we identify the most sensitive ice sheet areas. The spatial differences in the response to the inter-annual temperature forcing are then analyzed in six regional sectors of the GrIS. Finally, we investigate how temperature variability influences the response of the ice sheet to an abrupt warning.

## 2 Methods

### 2.1 The ice sheet flow model

To determine the influence of inter-annual temperature variability on the modeled present-day Greenland Ice Sheet we use the three-dimensional Parallel Ice Sheet Model (PISM) (www.pism.io). PISM is an open-source thermodynamically coupled ice sheet model that applies two shallow approximations to the Stokes equation, both assuming a small ice-sheet aspect ratio. The Shallow Ice Approximation (SIA) assumes that the horizontal shear stresses and the longitudinal deviatoric stresses are negligible compared to the vertical shear stresses. This assumption holds well for most of the interior of the Greenland Ice Sheet where there is limited basal sliding. The Shallow Shelf Approximation (SSA), on the other hand, assumes that the shear stresses are negligible compared to the longitudinal or membrane stresses of the ice flow (Schoof, 2006). In the hybrid model incorporated in PISM, the horizontal velocity of the ice is given by a weighted average of the SIA velocity and the SSA velocity using the SSA as a sliding law (Bueler and Brown, 2009). The constitutive relation for the rheology of ice used in PISM is based on Glen's flow law (Glen, 1955), modified by Nye (Nye and Perutz, 1997) and Lliboutry and Duval (Lliboutry and Duval, 1985), or formally the Glen-Paterson-Budd-Lliboutry-Duval law:

$$\dot{\epsilon}_{ij} = EA(T, P, w)\tau_e^{n-1}\tau_{ij}, \tag{3.1}$$

where $n$ is the flow law exponent, which we take to be 3 for both shallow approximations, $\tau_e$ is the effective deviatoric stress and $\tau_{ij}$ are the components of the deviatoric stress tensor. $A$ is the ice softness which is given piecewise for cold and temperate ice by two Arrhenius functions of the pressure, $P$, temperature, $T$, and liquid water fraction, $w$, (Aschwanden et al., 2012). The enhancement factor, $E$, is set to 3 for the SIA and 1 for the SSA. The study by Aschwanden et al. (2016) recommended an SIA enhancement factor of $E = 1.25$ for the Greenland Ice Sheet when tuned to match the ice flow velocity of the outlet glaciers, but we use their recommended set of parameters for $E = 3$, which overall provides the best fit to the Greenland Ice Sheet ice volume, see discussion. The basal sliding velocity $\mathbf{u}_b$ from the SSA is related to the basal shear stress $\tau_b$ and the yield stress through a power friction law, where we use a pseudo-plasticity exponent $q$ of 0.6 following Aschwanden et al. (2016). The yield stress is given by the Mohr-Columb model and is modified by a till friction angle to make the till softer in lower-lying regions. We parameterize the till friction angle as a continuous function of the bed topography that increases linearly from 5° to 40° between 700 m below and 700 m above sea level following Aschwanden et al., 2016. For bed topography, we use IceBridge BedMachine Greenland, version 4 (Bamber et al., 2013), while the geothermal heat flux distribution is taken from Shapiro (2004). Our model setup does not account for calving through a representation of the physical processes, instead, we remove

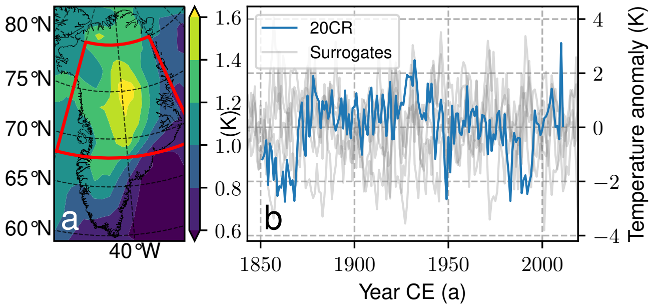

**Figure 3.1:** (a) Standard deviation of the annual mean temperature in the 20CR dataset, for the period 1851–2014 (Compo et al., 2011). (b) Anomalies compared to the mean of the whole period of the spatially averaged annual mean temperatures over the red box in (a) together with five of the modeled auto-regressive surrogates used to mimic the variability in the experiments.

all ice that exceeds the present-day boundary using the prescribed front retreat option in PISM, similar to the "retreat implementation" used in ISMIP6 (Nowicki et al., 2020).

## 2.2 Climate forcing

For the surface boundary conditions, we use the 2-meter air temperature field and precipitation field from RACMO2.3p2 at 5.5 km spatial resolution (Noël et al., 2019). We use a 12-month climatology based on the multi-year monthly averages of temperature and precipitation for the period 1960–1989, in which the Greenland Ice Sheet volume is considered to be close to equilibrium (The IMBIE Team, 2020). This is used as the climate forcing in the model initialization. The temperature and precipitation fields are used to calculate the surface mass balance (SMB). All precipitation is taken to be snow accumulation for temperatures below 0 °C, while the fraction of snow is taken to linearly decrease to zero between 0 °C and 2 °C. Surface melt is calculated with a positive degree-day scheme which assumes that the amount of melt is proportional to how much the temperature exceeds the freezing temperature. The positive degree day factors used are $3.3\,\mathrm{mm\,K^{-1}\,d^{-1}}$ for snow and $8.8\,\mathrm{mm\,K^{-1}\,d^{-1}}$ for ice. In addition to the inter-annual variability and the seasonal cycle, the temperatures also fluctuate daily, so while the monthly mean temperature might be below freezing, some days it will be above, resulting in melting. Therefore, it is assumed that the daily temperature is given by a normal distribution around $\bar{T}$ with variance over the month of $\sigma^2_{\mathrm{pdd}}$. The number of positive degree-days, $D$, for a time interval $\Delta t = t_2 - t_1$ is given by

$$D(\Delta t) = \int_{t_1}^{t_2} dt \int_0^{\infty} dT \exp\left(-\frac{(T - \bar{T}(t))^2}{2\sigma^2_{\mathrm{pdd}}}\right). \tag{3.2}$$

We use a constant uniform positive degree day standard deviation of $\sigma_{\mathrm{pdd}} = 5\,\mathrm{K}$ (Payne et al., 2000). To adjust the temperature for changes in surface altitude throughout the simulation, we use a lapse rate of $6.5\,\mathrm{K\,km^{-1}}$.

## 2.3 Including inter-annual temperature variability in the forcing field

To assess the effect of inter-annual temperature variability on the Greenland Ice Sheet volume evolution, an ensemble of 50 temperature time series with a length of 10 ka, denoted surrogates, are constructed based on the statistics of the 20CR over the period 1851–2014 (Compo et al., 2011). These are then added to the 12-month climatology from RACMO with mean monthly temperatures averaged over 1960-1989, which does not include inter-annual variability. The resulting climate-forcing fields represent the 1851–2014 inter-annual temperature variability over Greenland, and we use these climate-forcing fields to investigate the effect of realistic climate variability in a model of the Greenland Ice Sheet. By using an ensemble of idealized, detrended forcing fields, we can assess the modeled ice sheet response and take into account the stochastic nature of the climate variability.

The inter-annual temperature variations of the temperature surrogates, $T$, are modeled as a function of time, $t$, according to the first-order auto-regressive model, (Hasselmann, 1976; Frankignoul and Hasselmann, 1977)

$$T_t = c + \phi T_{t-1} + \varepsilon_t, \tag{3.3}$$

where $\phi$ is the auto-regressive parameter and $\varepsilon_t$ is white noise drawn from a Gaussian distribution with zero mean and variance $\sigma_\varepsilon^2$. We use the statistics of the full period of the 20CR to generate the 10 ka timeseries. The variability found in the 20CR dataset is non-uniform over Greenland as shown in Fig. 3.1 (a), so we follow the procedure by Mikkelsen et al. (2018) and average over a box spanning from 68 to 80°N and from 25 to 60°W. We then de-trend this time series by subtracting its least squares linear fit and set $c = 0$, such that the temperature surrogates have zero mean. From the resulting time series, we estimate the parameters in (3.3) to be $\phi = 0.67$ and $\sigma_\epsilon = 0.92\,\mathrm{K}$. The 50 temperature surrogates constructed using these parameters all have a standard deviation of 1.24 K. The de-trended time series and a subset of the constructed temperature surrogates used to force the positive degree day model are shown in Fig. 3.1 (b). To account for the variability being non-uniform, we scale the time series to match the temporal standard deviation in each grid point, i.e. we compute the outer product of the standard deviation map in Fig. 3.1 (a) and the generated time series divided by their standard deviation. In addition to the 50 surrogates based on the 20CR data, we also construct an ensemble of 50 surrogates with twice the standard deviation representing another background climate state with more pronounced extreme events denoted 20CRx2.

## 2.4 Model initialization

The ice sheet model is initialized prior to the experiments with the inter-annual temperature time series. As a first step in the model initialization, the ice sheet model is run for 50 ka forced with the 12-month climatology at 9.6 km resolution followed by a 20 ka run at 4.8 km resolution to obtain a state-state Greenland Ice Sheet close to equilibrium. The steady-state volume fluctuates around equilibrium with a standard deviation of 2.95 mm SLE for the 9.6 km resolution and 0.33 mm mm SLE for the 4.8 km resolution. As mentioned above, we restrict

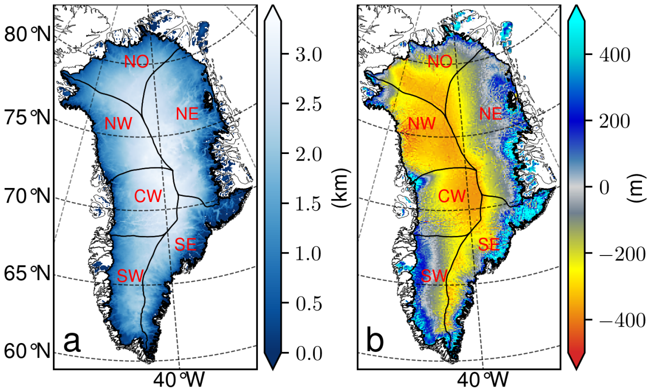

**Figure 3.2:** (a) Observed ice sheet thicknesses of the Greenland Ice Sheet (Morlighem et al., 2017). (b) Changes in modeled ice sheet thickness after initializing it for 50 ka at a resolution of 9.6 km followed by 20 ka at a resolution of 4.8 km.

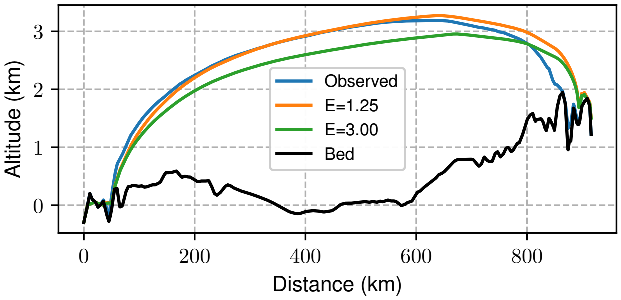

**Figure 3.3:** Cross sections of the Greenland Ice Sheet surface elevation at 73° N going East for the initialized ice sheet model at different enhancement factors.

the ice sheet to the domain of the present-day ice sheet and remove all ice beyond the present-day margin. This boundary condition leads to a larger amount of ice discharge compared to observations but is required to keep the geometry of the ice sheet close to the observations. The resulting steady-state Greenland Ice Sheet has decreased in volume to 7.07 m SLE relative to the observed present-day GrIS. It is thinner in the interior and thicker close to the margin compared to the observed Greenland Ice Sheet as shown in Fig. 3.2 with an overall RMSE of the elevation difference between modeled and observed thickness of 247 m.

The overall shape of the ice sheet depends on the SIA enhancement factor, $E$. As mentioned above, we use $E = 3$ in our study, which overall provides the best fit to the Greenland Ice Sheet, but we also made an additional set of runs using $E = 1.25$ to test the effect of the enhancement on our results. As shown in Fig. 3.3, decreasing the softness to $E = 1.25$ in the steady-state run results in an ice sheet that is thicker than both the observed ice sheet and the one modeled with $E = 3$. Consequently, the total SMB over the Greenland Ice Sheet is 21.2 Gt a$^{-1}$ larger with $E = 1.25$ compared to $E = 3$ due to the surface elevation feedback; this results in an equally larger discharge at the front, since we are investigating steady-states.

### 2.5 Experiments

After the model initialization, the simulation is continued with an ensemble of runs where the temperatures are uniformly offset from the 12-month climatology by the two ensembles of temperature surrogates. Like the ensembles of temperature surrogates, we denote the two ensembles of Greenland Ice Sheet simulations, 20CR and 20CRx2. We run the ensembles for 10 kyrs with a resolution of 4.8 km until the ensemble means have reached new steady states. In addition, an unperturbed control run is also considered to assess the effect of the inter-annual temperature variability.

The second experiment starts from the same initialized ice sheet as the above experiment but with an instantaneous and uniform change in temperature forcing of [0, 0.5, 1, 1.5, 2] K in order to assess the response of the Greenland Ice Sheet to changes in temperature with and without inter-annual temperature variability. These simulations are all carried out over 500 years after the instantaneous temperature change.

## 3 Results

### 3.1 Steady state

The evolution of ice volume of the two ensembles is shown in Fig. 3.4. After 10 ka, the ice volumes are 1.9±0.4 and 11.5±1.4 cm SLE smaller relative to the control for the 20CR and 20CRx2 simulations, respectively, where the first number denotes the ensemble mean and the second number the ensemble standard deviation. The volume changes correspond to mean elevation changes of 1.8±0.3 and 10.8±1.3 m for the 20CR and 20CRx2, respectively. This shows that the modeled ice sheet response to variability is strongly non-linear. A doubling of the variability results in an approximately 6 times larger response.

As shown in Fig. 3.5, the temperature-variability-induced mass losses from the SMB and basal mass balance are fully compensated by reduced discharge at the end of the simulation, resulting in the steady states. This result shows that the increased melt in ensemble runs is being compensated for by reduced discharge, i.e. a negative feedback caused by calving dynamics.

The thickness difference between the control run and the ensemble mean is shown in Fig. 3.6 (a) and (b) and the ensemble standard deviations in Fig. 3.6 (c) and (d). The ensemble mean simulated ice sheet is thinner than the control run and the largest difference is in the north region, but for the 20CRx2 the difference is also considerable on the west coast. From this, we see a clear thinning induced by the temperature variability, especially in the North for both ensembles. We divide the Greenland Ice Sheet into the 6 basins (Mouginot and Rignot, 2019) shown in Fig. 3.6, with their respective mean ice thickness changes listed in Table 3.1. The Northern (NO) basin holds 11.6% of the initialized ice volume but contributes to about 40% of the mass loss during the simulations with inter-annual variability in the temperature forcing. In contrast, the Southeast (SE) basin holds 12.8% of the initialized ice volume but contributes only about 1% of the total mass loss during the simulations. Fig. 3.7 shows the SMB for the control run and the

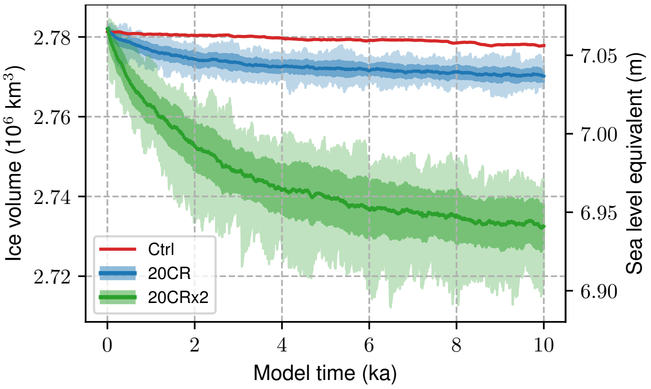

**Figure 3.4:** Evolution of the Greenland Ice Sheet volume over 10 ka including the inter-annual temperature variability of 20CR (blue) and 20CRx2 (green) in the temperature forcing and without the inter-annual temperature variability (red). The blue and green solid lines denote the average of the simulations in each ensemble while the light and dark-shaded areas denote the range and the standard deviation of the ensembles, respectively.

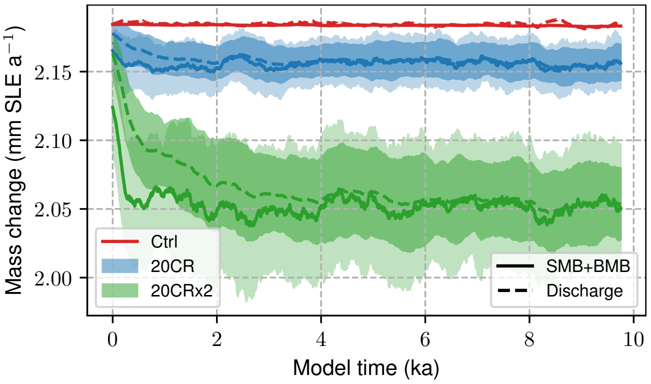

**Figure 3.5:** Evolution of the sum of the surface mass balance and the basal mass balance (SMB+BMB) (solid), and of discharge (dashed) over the Greenland Ice Sheet over 10 ka including the inter-annual temperature variability of 20CR (blue) and 20CRx2 (green) in the temperature forcing and without the inter-annual temperature variability (red). The solid and dashed lines denote the average of the simulations in each ensemble while the light and dark-shaded areas denote the standard deviation of the ensembles of the SMB+BMB and the discharge, respectively. Both observables have been smoothed with a 500 year running mean.

ensemble mean for the first 10 years. The distribution of mass loss negatively correlates with the SMB, i.e., areas with high mass loss correspond to areas with a low SMB.

The effect of including climate variability on the Greenland Ice Sheet volume is similar for the $E = 1.25$ runs compared to the $E = 3$ runs; the mean ensemble ice volume is $2.0 \pm 0.4$ cm smaller for the 20CR run and $8.8 \pm 0.9$ cm smaller for the 20CRx2 run compared to the control simulation with $E = 1.25$.

We also tested a uniform variability over Greenland, following Mikkelsen et al. (2018), which resulted in a slightly larger effect.

## 3.2 Response to instantaneous changes in temperature forcing

The transient behavior of the simulations when forced with an instantaneous change in the temperature forcing, with and without the inter-annual variability is shown in Fig. 3.8 where the average rate of change in mass for the first 100, 300, and 500 years are shown. The mass

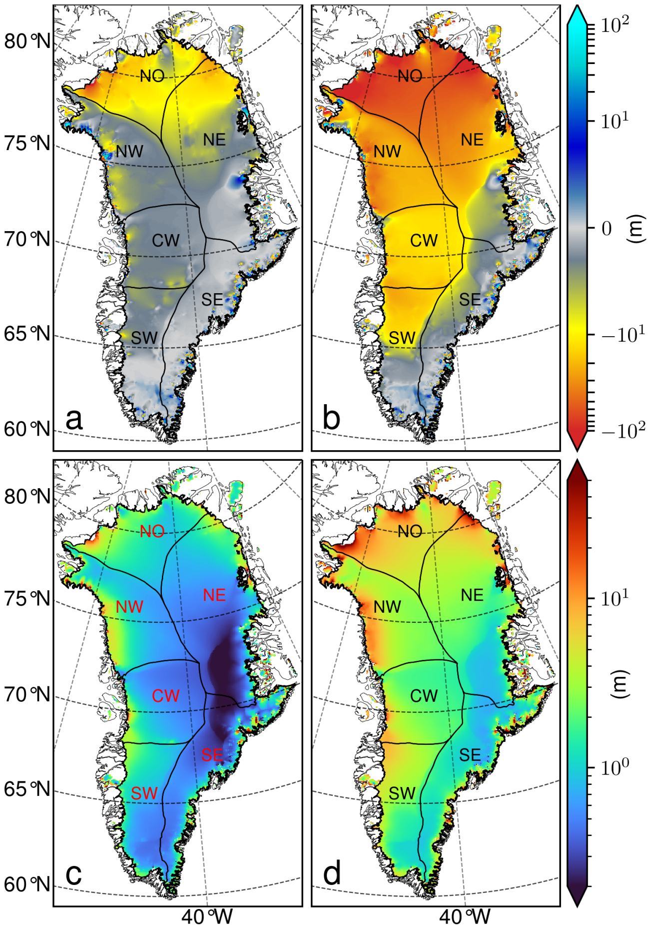

**Figure 3.6:** Ensemble mean ice sheet thickness deviations with respect to the control run for 20CR (a) and 20CRx2 (b) and ensemble standard deviations for 20CR (c) and 20CRx2 (d).

| Basin | Control | | 20CR | | | 20CRx2 | | |
|---|---|---|---|---|---|---|---|---|
| | SLE | Rel | ΔSLE | Δh | Rel | ΔSLE | Δh | Rel |
| NW | 1.10 m | 15.5 % | −2.5±0.7 mm | −3.6±1.1 m | 12.6 % | −16.8±2.6 mm | −24.4±3.8 m | 14.6 % |
| CW | 1.25 m | 17.7 % | −1.8±0.4 mm | −3.1±0.6 m | 9.3 % | −8.2±1.3 mm | −14.0±2.2 m | 7.1 % |
| SW | 0.80 m | 11.3 % | −1.0±0.4 mm | −1.7±0.8 m | 4.9 % | −4.6±1.5 mm | −8.3±2.7 m | 4.0 % |
| SE | 0.90 m | 12.8 % | −0.2±0.4 mm | −0.3±0.5 m | 1.0 % | −1.5±1.0 mm | −2.1±1.4 m | 1.3 % |
| NE | 2.14 m | 30.4 % | −6.0±0.8 mm | −5.0±0.6 m | 31.0 % | −36.4±3.5 mm | −30.3±2.9 m | 31.6 % |
| NO | 0.82 m | 11.6 % | −7.8±0.9 mm | −13.1±1.5 m | 39.8 % | −44.6±4.6 mm | −75.7±7.7 m | 38.7 % |
| Total | 7.06 m | 100.0 % | −19.5±3.6 mm | −1.8±0.3 m | 100.0 % | −115.2±13.9 mm | −10.8±1.3 m | 100.0 % |

**Table 3.1:** The SLE volumes of each basin at the end of the control run and the average volume loss of the two ensembles in SLE (ΔSLE), average elevation deviation (Δh) and percentage of total volume loss (Rel).

loss rate increases with increasing temperature step. For the first 100 years, the average rate of mass loss per degree warming is approximately 0.15 mm SLE $a^{-1}$ $K^{-1}$ for the control run, and 0.014–0.17 mm SLE $a^{-1}$ higher than the control run when adding the inter-annual variability in the temperature forcing depending on the size of the temperature step. For the 20CRx2, the rate of change in mass is almost twice as large as the rate of the control run. For each experiment with an instantaneous change in temperature, the control run lies within the range of the ensemble runs for the first 100 years, close to the lower bound of mass loss rate of the 20CR runs for the 300 and 500 years, and below the mass loss rates of the 20CRx2 runs for the 300 and 500 years.

# 4 Discussion

In this study, we investigate the effect of climate variability on the steady-state volume of the Greenland ice sheet. Most models in the ISMIP6 study had a mass loss lower than observed over the historical period (Goelzer et al., 2020). In some cases, this difference could be explained by the fact that climate forcing over the historical period did not include climate variability on interannual and decadal timescales, but the effect from the historical mass loss being inaccurate was effectively removed by considering only the difference from a control run (Goelzer et al., 2020). In order to improve projections of the ice sheet mass loss, one step could be to include the observed variability in the forcings over the historical period in order to improve the model initialization. Our results provide a quantified assessment of this effect.

The main goal of our study was to revise the previous results for a simplified Greenland Ice Sheet (Mikkelsen et al., 2018) by considering a more appropriate state-of-the-art ice flow model for the GrIS. We found that the total volume of the Greenland Ice Sheet is reduced by 1.9±0.4 cm SLE after 10 ka when including the inter-annual variability of the 20CR in temperature forcing. This is much less than the result of 0.5–1 m in Mikkelsen et al. (2018), showing that a more complex model in our study, including ice-flow dynamical feedback, reduces the effect of temperature variability on the ice sheet volume. Our study differs from Mikkelsen et al. (2018) by the complexity of the ice sheet model. They use a simplified model (Oerlemans, 2003), assuming that ice flows as perfectly plastic material and that the ice sheet is axially symmetric with a bedrock that slopes linearly downward. They coupled their model to atmospheric variations only by changing the equilibrium line altitude linearly according to variations in global temperature and then calculating the corresponding change in the steady-state volume. The simplified ice sheet model used by Mikkelsen et al. (2018) does not have ice-ocean interaction or calving included, a process that plays a significant role for the GrIS, where only half of the mass loss is due to ablation (The IMBIE Team, 2020).

In our model setup, the influence of inter-annual temperature variability on the total mass balance of the Greenland Ice Sheet is reduced by ice discharge, since an increase in the melt due to temperature variability will result in thinning resulting in reduced discharge. The feedback from discharge to the mass loss induced by including inter-annual temperature variability is thus negative. This negative feedback is not accounted for in the study by Mikkelsen et al. (2018),

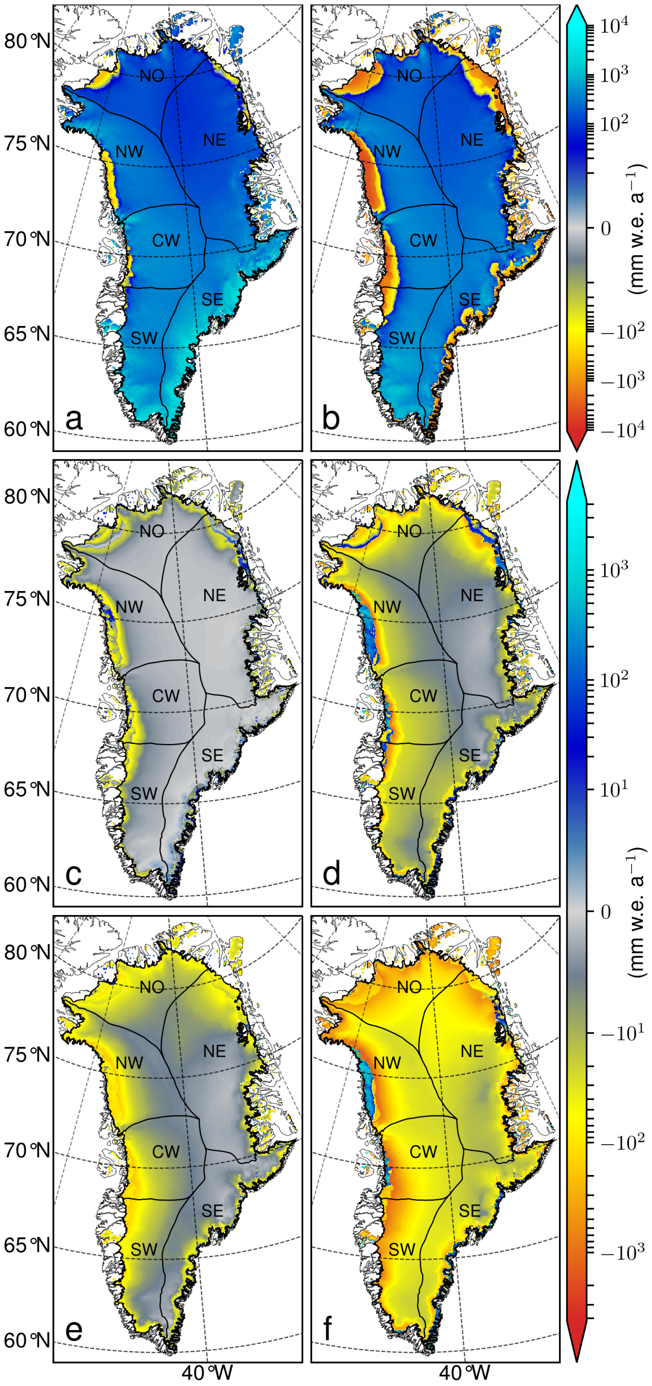

**Figure 3.7:** Mean annual SMB (a) and July SMB (b) for the first 10 years of the control run. Mean ensemble deviations for 20CR compared to the control run of mean annual SMB (c) and July SMB (d). Mean ensemble deviations for 20CRx2 compared to the control run of mean annual SMB (e) and July SMB (f).

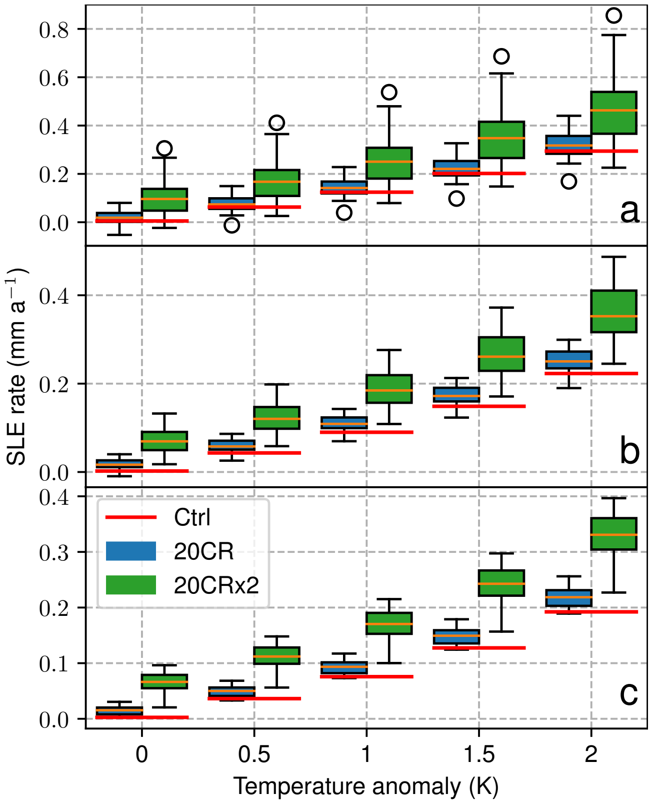

**Figure 3.8:** Average rates of change in volume during the first 100 (a), 300 (b), and 500 (c) years when applying an instantaneous change in temperature with and without inter-annual variability in temperature forcing. For each change in temperature, the boxplots show the ensemble distribution and are slightly shifted along the x-axis for appearance. The red line shows the average rate of change for the control run.

which may explain why they find a larger sensitivity to inter-annual temperature variability than we find here. However, the fixed margin calving scheme implemented in our model is not based on a physical calving criterion but only ensures that the Greenland Ice Sheet does calve at the present-day margin.

We speculate that the response to temperature variability is dampened by the negative feedback between SMB change and ice discharge. Mikkelsen et al., 2018 lacks the important negative feedback from discharge and their result should therefore be considered an upper bound on the sensitivity. Here, we use mask-based calving which results in particularly strong negative feedback as it can accommodate any change in horizontal flux. We, therefore, argue that our results should be taken as a lower bound.

The modeled steady-state ice sheet fluctuates about the equilibrium volume with a standard deviation of 3.05 mm SLE for the 9.6 km resolution run, which reduces to 0.38 mm SLE for the 4.8 km resolution run. Meanwhile, the volume of the ensemble members fluctuates with a mean standard deviation of 3.70 and 10.2 mm SLE for the 20CR and 20CRx2 runs, respectively. It is therefore important to consider simulations at a resolution of at least 4.8 km in order for the mass-loss signal not to be drowned in the fluctuations around the steady state.

The response to the inter-annual temperature variability in ice volume is greatest in the NO basin (Table 3.1, Fig. 3.6) where the volume is reduced by 7.8±0.9 and 45±5 mm SLE for the 20CR and 20CRx2 run, respectively, corresponding to a mean elevation reduction of 13±2 and 76±8 m compared to the control run. This is in stark contrast to the SE basin where the volume reduces by 0.2±0.4 and 1.5±1.0 mm SLE for the 20CR and 20CRx2 simulations, respectively, corresponding to a mean elevation reduction of 0.3±0.5 and 2.1±1.4 m compared to the control run. The spatial distribution of mass loss correlates with the spatial distribution of SMB, which is positive for all basins but balanced by an equally large discharge at the ice front.

In Fig. 3.7 the spatial distribution of the SMB is plotted for the control run and the ensemble means, both for July and the annual mean. For July, the ablation zone reaches far inland in the NW, CW, NO, and NE basins, while it is more narrowly confined closer to the ice sheet margin in the SE basin. When including the inter-annual variability in the temperature forcing, the change in SMB is greatest near the equilibrium line altitude where the asymmetry of the positive degree day scheme is most pronounced. The SE basin accounts for 49.6% of the total SMB, while the NO basin only accounts for 2.8% of the total SMB for the control run. Including the inter-annual variability in temperature forcing decreases the mass balance of the ensemble mean by 0.4% for the SE basin and by 6% for the NO basin for the 20CR ensemble relative to the control run. Those numbers increase to 1.3% and 23% for the 20CRx2 ensembles.

The 20CRx2 ensemble simulations are constructed to have twice the inter-annual temperature variability found in the 20CR temperatures for the period 1851–2014 (Fig. 3.1). In a future warmer climate, the variability of climate may increase, and these simulations are included in order to test the influence of a higher variability than in the recent past. The temperature variability is not uniform over Greenland but is greatest in the Northern areas, which we also found to be the most sensitive. The northern basins have less precipitation than the southern basins, and are thus more sensitive to climate changes that lead to increased surface melting. The SW basin has contributed most to the recent observed mass loss (The IMBIE Team, 2020), but this could be due to a combination of several different factors, not considered in our study that focuses solely on including the temperature variability.

In our study, we did not account for the effect of variation in precipitation. However, we conducted an additional test where we ran an ensemble forced by precipitation anomalies from the RACMO data at 1 km spatial resolution (Noël et al., 2019) constructed in the same manner as the temperature surrogates. We found the effect to be negligible compared to the effect of inter-annual temperature variability. We also found temporal anomalies in temperature and precipitation to be approximately uncorrelated when averaging over Greenland.

Our study invites further work to investigate the effect of spatial variability in temperature and precipitation forcing fields on the ice sheet and its response to climate changes. Future studies could include the feedback of the atmosphere as the Greenland Ice Sheet evolves (i.e, thinning and retreat) in response to temperature and precipitation changes and investigate regional differences in the variability.

# 5 Conclusion

We ran an ensemble of ice sheet simulations to determine the influence of inter-annual temperature variability on the Greenland Ice Sheet volume. Each ensemble member was forced by a realization of temperature anomalies given by an auto-regressive model based on the inter-annual temperature variability found in the 20CR dataset over the period of 1851–2014 and added to a 12-month climatology from RACMO. Furthermore, we tested the influence of temperature variability on projections by considering a series of ensemble runs where we abruptly increased the temperature by a step change of [0.5, 1.0, 1.5, 2.0] K. We repeated the experiments with twice the inter-annual temperature variability found in the 20CR dataset; these simulations are denoted 20CRx2.

Accounting for inter-annual temperature variability in simulations of the Greenland Ice Sheet leads to a smaller steady-state ice sheet volume in our study compared to the simulation forced with a constant climatology (all else being equal), as well as higher mass loss rates with a spread among ensemble members when forced with an abrupt change in temperature. We find that the steady-state volume decreases by $1.9\pm0.4$ and $11.5\pm1.4$ cm SLE for the 20CR and 20CRx2 simulations, respectively, when forced with a variable temperature forcing compared to a constant temperature forcing. For the first 100 years, the average rate of mass loss per degree warming is approximately 0.15 mm SLE $\text{a}^{-1}$ $\text{K}^{-1}$ for the control run, and 0.014–0.17 mm SLE $\text{a}^{-1}$ higher than the control run for the first 100 years when adding the inter-annual variability in the temperature forcing depending on the size of the temperature step.

Our results are based on a complex ice flow model with ice dynamical feedbacks. Compared to previous results with a simpler ice flow model Mikkelsen et al., 2018, we find a smaller sensitivity of the simulated ice sheet to variability in the climate forcing. We argue that our result should be interpreted as a lower bound. In a future warmer climate, the climate variability is projected to increase (Seneviratne et al., 2021), potentially leading to further increase of the ice sheet mass loss.

The sensitivity of the Greenland Ice Sheet to inter-annual temperature variability is found to be spatially dependent. The NO basin, experiencing less precipitation and lower SMB than other Greenland Ice Sheet basins, loses 0.9–1.1% of its total volume, corresponding to 40% of the total mass reduction found between the control run and the ensemble mean.

Our results show that temperature variability in the forcing of the ice sheet model affects both the Greenland Ice Sheet equilibrium volume and its transient response to instantaneous changes in temperature. The present-day Greenland Ice Sheet is the result of past climate changes and variability, and thus projections must take into account the effect on both the initial, present-day ice sheet, as well as in projections of its future evolution. In this regard, including climate variability is important, since it contributes to both the evolution and the uncertainty of future projections of mass loss.

## 6 Acknowledgments

We acknowledge funding from the Independent Research Fund Denmark through the project GreenPlanning (grant no. 0217–00244B). We thank the editor Professor Douglas MacAyeal and an anonymous referee for their comments, which helped improve the manuscript.

## Chapter 4

# Bayesian Calibration of a Positive Degree Day Model

This chapter contains the following paper:

Mikkel Lauritzen, Brice Noël, and Christine S. Hvidberg (in prep.). “Bayesian Calibration of a Positive Degree Day Model”.

which is still a work in progress but is planned to be submitted soon. The bibliography for this manuscript is included in the main bibliography at the end of the thesis.

# Bayesian Calibration of a Positive Degree Day Model

Mikkel Lauritzen[1], Brice Noël[2], and Christine Hvidberg[1]

[1] *Niels Bohr Institute, University of Copenhagen, Copenhagen, Denmark*
[2] *Department of Geography, Laboratoire de Climatologie et Topoclimatologie, University of Liège, Liège, Belgium*

## Abstract

The positive degree day (PDD) model offers an elegant way to model the surface mass balance (SMB) in terms of prescribed temperature and is widely used in glaciology due to its simplicity and effectiveness in estimating melt rates over ice sheets, especially for long paleoclimatic simulations. In this study, we calibrate a PDD model to the SMB of RACMO for the 1960-1989 climatology over Greenland. While the PDD model struggles to precisely delineate the ablation zone during summer using uniform PDD parameters, we find that it successfully captures the Greenland-wide integrated SMB with the PDD parameters $f_\mathrm{s} = 7.35 \pm 1.61$ mm $\mathrm{K}^{-1}$ $\mathrm{d}^{-1}$ and $f_\mathrm{i} = 10.21 \pm 2.65$ mm $\mathrm{K}^{-1}$ $\mathrm{d}^{-1}$ when the refreezing parameter is 0.6.

## 1 Introduction

In the positive degree day (PDD) model, the melt is directly proportional to the accumulated positive degree days. Although it is physically unjustified, the model is empirically supported; for instance, Braithwaite and Olesen (1989) found a high correlation of 0.96 between the positive degree days and observed melt in Western Greenland. Such correlations are especially relevant for long paleoclimatic ice sheet simulations where the surface mass balance (SMB) patterns are likely to evolve with changing ice sheet geometry; a PDD approach is also justified as physically-based models are computationally demanding.

In this paper, we perform a Bayesian calibration of a PDD model against the SMB of the regional climate model RACMO (Noël et al., 2019) to assess its ability to capture the Greenland ice sheet SMB. The PDD model is computationally efficient compared to a regional climate model, making it feasible to densely sample the parameter space using Markov chain Monte Carlo (MCMC) algorithms. In this study, we calibrate the PDD parameters to the modeled SMB of RACMO due to its accurate representation of observed runoff (Fettweis et al., 2020).

# 2 Method

For our setup, we use the PDD model from the Parallel Ice Sheet Model (PISM; Bueler and Brown (2009) and Winkelmann et al. (2011)). In the PDD scheme the modeled melt over a time interval $\Delta t$ is proportional to the degree day factor,

$$D(\Delta t) = \int_{\Delta t} dt \int_0^\infty dT \exp\left(-\frac{(T - \bar{T}(t))^2}{2\sigma_{\mathrm{pdd}}^2}\right), \tag{4.1}$$

where $\bar{T}(t)$ is the mean temperature which is assumed to fluctuate normally within its sampling interval with standard deviation $\sigma_{\mathrm{pdd}}$. Here, we use the default value of $\sigma_{\mathrm{pdd}} = 5$ K.

There are two constants of proportionality: $f_s$ for snow and $f_i$ for ice, applied once all the snow has melted. The mass balance year begins on October 1st, where the initial snow depth is set to zero. Precipitation is considered as snow at temperatures below 0°C and as rain above 2°C, with a linear transition in between. A uniform fraction of the modeled melt refreezes and is retained in the firn while the remainder runs off, contributing to the SMB. We keep the default refreezing fraction of 0.6 in PISM, not varying it as it only scales the PDD parameters, effectively limiting the model to two degrees of freedom.

As input for the PDD scheme, we will use a multi-year monthly average climatology of 2-m air temperature and precipitation from RACMO for the 1960-1989 period interpolated onto a 10 km grid. During this period, the ice sheet is believed to have been in a steady state. This results in a spatio-temporal field of SMB $\dot{m}^{\mathrm{mod}}_{t,x,y}(f_{\mathrm{s}}, f_{\mathrm{i}})$ which we will calibrate to a target SMB denoted $\dot{m}^{\mathrm{obs}}_{t,x,y}$. We choose the 1960-1989 SMB from RACMO (Noël et al., 2019) as our target due to its precise depiction of observed runoff (Fettweis et al., 2020; Mankoff et al., 2020). Integrated over Greenland, the SMB is positive at 43.7 Gt $\mathrm{a}^{-1}$ in this period.

We have opted for two distinct Bayesian calibration strategies. The first strategy involves calibrating the spatially integrated SMB. In this approach, the likelihood function is

$$L_t(f_{\mathrm{s}}, f_{\mathrm{i}}) = \frac{1}{\sigma_t\sqrt{\pi}} \exp\left(\frac{\sum_t \left(\sum_x \dot{m}^{\mathrm{obs}}_{t,x} - \dot{m}^{\mathrm{mod}}_{t,x}(f_{\mathrm{s}}, f_{\mathrm{i}})\right)^2}{2\sigma_t^2}\right), \tag{4.2}$$

where $\sigma_t$ denotes the standard deviation of the spatially integrated mass balance, and $t$ and $x$ denote time and spatial coordinates, respectively. For the other strategy, we calibrate the temporally integrated SMB, reversing the roles of $t$ and $x$. Without a known value for $\sigma_t$ and $\sigma_x$, we treat them as a hyperparameter to be estimated during the analysis. The analysis is carried out within the PROMICE mask (Colgan et al., 2019), specifically excluding peripheral glaciers and focusing on the central ice sheet regions.

We choose the prior distributions of the PDD parameters to be uniform in the interval from 0 to 30 mm $\mathrm{K}^{-1}$ $\mathrm{d}^{-1}$. The hyperparameter priors of $\sigma_t$ and $\sigma_x$ are chosen to be log-normally distributed to ensure that they are positive and that the MCMC algorithm converges.

To sample the posterior distribution of these parameters, we utilize the *emcee* package in Python

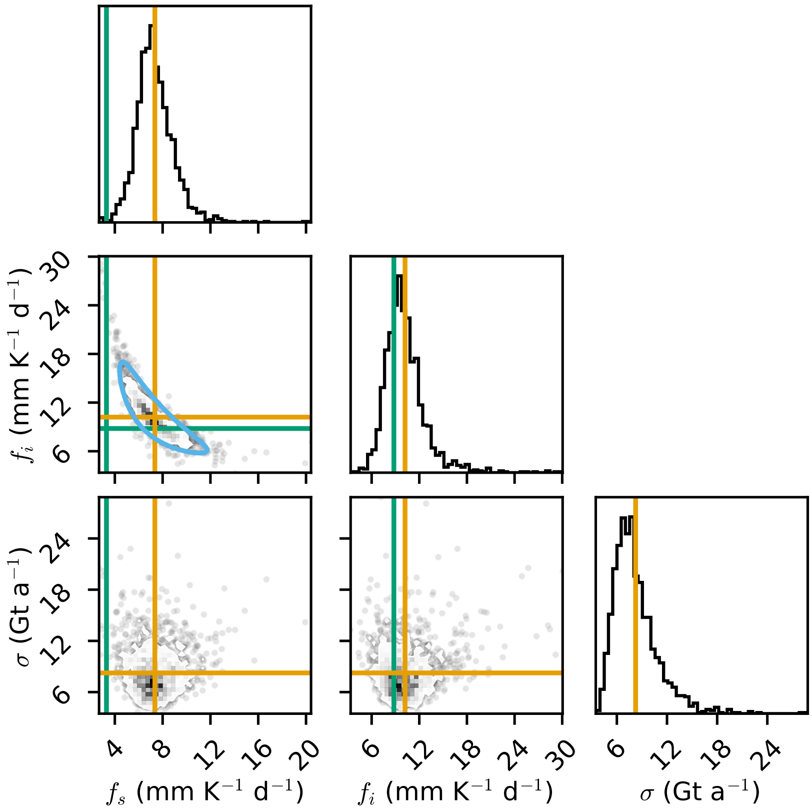

**Figure 4.1:** Parameter distributions of $f_s$, $f_i$, and $\sigma$ generated by the MCMC algorithm. The yellow line indicates the mean, while the green line indicates the default values from PISM. The blue line represents the 1 standard deviation bounds of a multivariate log-normal fit. The units on the y-axes on the diagonal are the inverse of the units on the x-axis.

(Foreman-Mackey et al., 2013). This package enables efficient exploration of the parameter space, facilitating the convergence to the posterior distribution by employing multiple interacting "walkers" that traverse the parameter space, thereby providing a comprehensive sampling. We couple the *emcee* algorithm to PISM with 32 walkers sampling the parameter space.

## 3 Results

For the spatially integrated calibration, the MCMC algorithm converged after 1000 steps with auto-correlations lengths between 61 and 90 for the three parameters. Fig. 4.1 shows the sampled posterior distributions. We estimate the PDD parameters for snow and ice to be $f_\mathrm{s} = 7.35\pm1.61$ mm K$^{-1}$ d$^{-1}$ and $f_\mathrm{i} = 10.21 \pm 2.65$ mm K$^{-1}$, respectively while we find the hyperparameter to be $\sigma = 8.25 \pm 2.68$ Gt a$^{-1}$. The monthly SMB is shown in Fig. 4.2, while the spatially integrated SMB is shown in Fig. 4.3. From October to April, the PDD model has little to no melt, whereas RACMO shows some melting at the coast. The PDD model fails to capture this due to a negligible amount of positive degree days during these months. In the remaining months of the year, the PDD model does not accurately delineate the ablation zone of RACMO. It underestimates the amount of melt within the ablation zone and overestimates it outside.

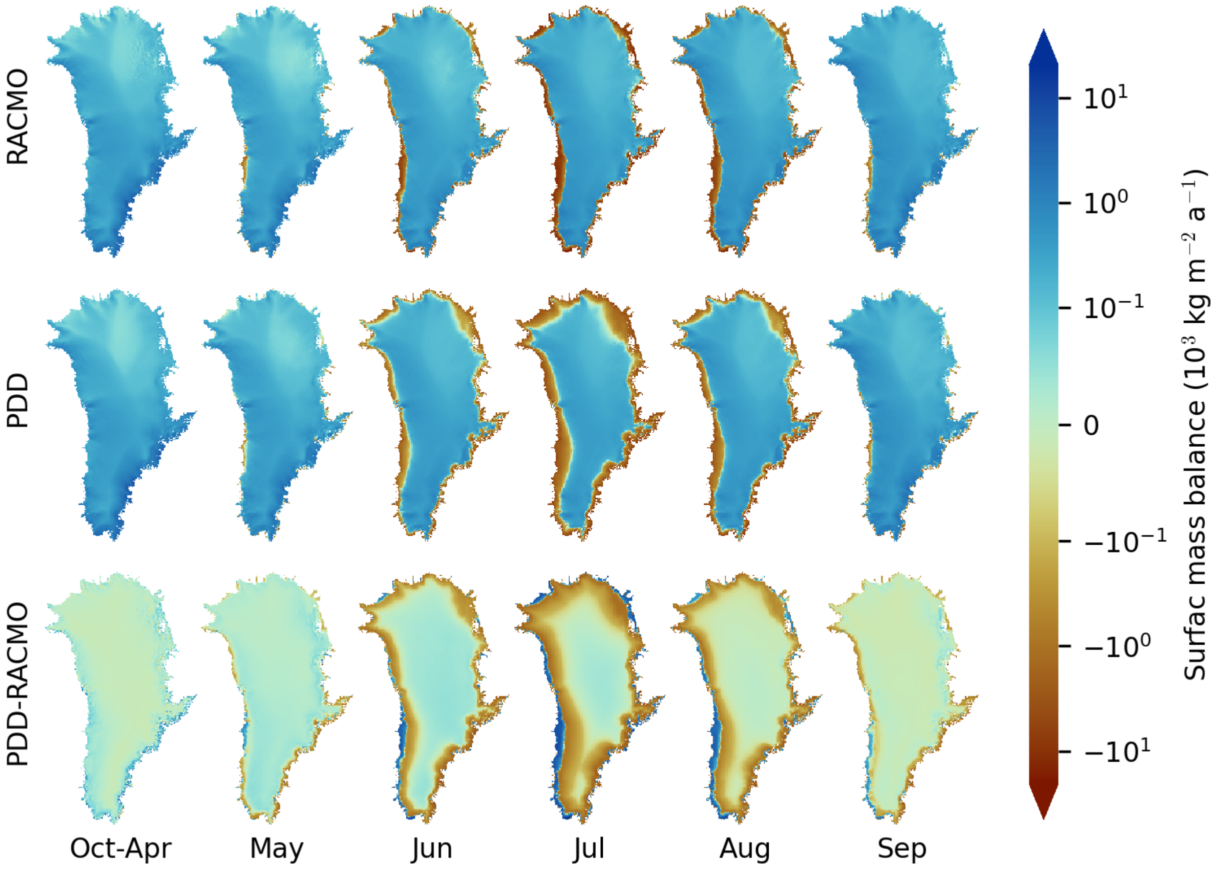

**Figure 4.2:** Mean seasonal SMB over the Greenland Ice Sheet from 1960 to 1989 for RACMO and the PDD model, along with their difference (PDD minus RACMO). The October-April data is presented as a mean, while the May-September data is shown for each individual month.

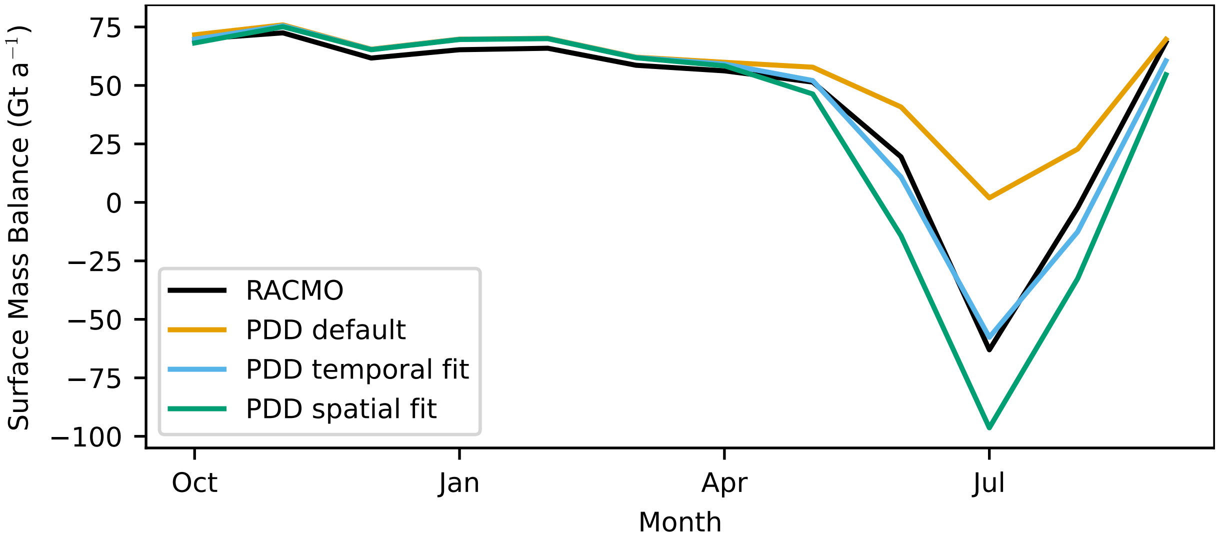

**Figure 4.3:** Mean seasonal SMB from 1960 to 1989 over the Greenland Ice Sheet, compared for the RACMO and PDD models. The PDD model is evaluated with three sets of parameters: the default values from PISM and the two mean values from the Bayesian calibration.

For the temporally integrated calibration, the estimated PDD parameters are larger at $f_\mathrm{s} = 11.60 \pm 6.88$ mm $\mathrm{K}^{-1}$ $\mathrm{d}^{-1}$ and $f_\mathrm{i} = 11.25 \pm 5.12$ mm $\mathrm{K}^{-1}$ $\mathrm{d}^{-1}$. This slightly reduces the error at the ablation zone where the mass balance is underestimated but increases the error further away from the margin. The resulting integrated SMB ends up being larger than that of the target, as shown in Fig. 4.3.

# 4 Discussion

This study assumed the PDD parameters to be uniform across Greenland, suggesting a consistent correlation between melt and degree days. We also opted for a uniform and constant temperature variability parameter, $\sigma_\mathrm{pdd}$, despite findings by Seguinot (2013) indicating its seasonal and spatial variation. Additionally, we set the refreezing parameter at 0.6 uniformly. This assumption is questionable, as there is likely negligible runoff at the center of the ice sheet, whereas refreezing could be substantially lower in the ablation zone. This could explain why the PDD model underestimates melt in these areas. While adjusting the PDD parameters locally might reduce errors in modeled SMB, it would introduce excessive degrees of freedom, potentially leading to "overfitting" of the model to observed data. Such an approach would be impractical for paleoclimatic simulations where changes in the ice sheet's geometry are crucial.

Calibrating the PDD model helps to quantify confidence in its parameters. These parameters, when combined with temperature reconstructions, facilitate long-term paleoclimatic simulations. These past temperature reconstructions carry uncertainties, resulting in additional complexity to the simulations.

Conversely, if the evolution of past ice sheets is sufficiently well constrained, ice sheet modeling could be used to deduce past surface mass balance (SMB) and, in turn, the temperatures using the calibrated PDD model. This inverse approach offers a potential method for understanding historical climate conditions, assuming there is enough accurate historical ice sheet data.

# 5 Conclusion

In this study, we performed a Bayesian calibration of a PDD model to the modeled SMB from RACMO for the 1960-1989 average seasonal climatology over Greenland. With constant and uniform refreezing and intra-monthly temperature variability, we calibrated the PDD parameters for snow and ice to be $f_\mathrm{s} = 7.35 \pm 1.61$ mm $\mathrm{K}^{-1}$ $\mathrm{d}^{-1}$ and $f_\mathrm{i} = 10.21 \pm 2.65$ mm $\mathrm{K}^{-1}$ when integrating the SMB over the Greenland Ice Sheet. These serve as prior beliefs for long paleoclimatic simulations where the mass balance changes with the ice sheet's topography.

# Chapter 5

# Modelling the Greenland Ice Sheet Holocene history

This chapter contains the following paper:

Mikkel Langgaard Lauritzen, Anne Munck Solgaard, Nicholas Mossor Rathmann, Bo Møllesøe Vinther, Aslak Grindsted, Brice Noël, Guðfinna Aðalgeirsdóttir, and Christine Schøtt Hvidberg (July 24, 2024). "Modeled Greenland Ice Sheet Evolution Constrained by Ice-Core-Derived Holocene Elevation Histories". In: *EGUsphere*, pp. 1–29. DOI: `10.5194/egusphere-2024-2223`

which is currently under review at the EGUsphere and might differ slightly from the online version. The bibliography for this manuscript is included in the main bibliography at the end of the thesis.

# Modeled Greenland Ice Sheet evolution constrained by ice-core-derived Holocene elevation histories

MIKKEL LAURITZEN,[1] ANNE SOLGAARD[3], NICHOLAS RATHMANN[1], BO M. VINTHER[1],
ASLAK GRINDSTED[1], BRICE NOËL[4], GUÐFINNA AÐALGEIRSDÓTTIR[2],
AND CHRISTINE S. HVIDBERG[1]

[1] *Niels Bohr Institute, University of Copenhagen, Copenhagen, Denmark*
[2] *Institute of Earth Sciences, University of Iceland, Reykjavík, Iceland*
[3] *Geological Survey of Denmark and Greenland, Copenhagen, Denmark*
[4] *Department of Geography, Laboratoire de Climatologie et Topoclimatologie, University of Liège, Liège, Belgium*

## Abstract

During the Holocene, the Greenland Ice Sheet (GrIS) experienced substantial thinning, with some regions losing up to 600 meters of ice. Ice sheet reconstructions, paleoclimatic records, and geological evidence indicate that during the Last Glacial Maximum, the GrIS extended far beyond its current boundaries and was connected with the Innuitian Ice Sheet (IIS) in the northwest. We investigate these long-term geometry changes and explore several possible factors driving those changes by using the Parallel Ice Sheet Model (PISM) to simulate the GrIS thinning throughout the Holocene period, from 11.7 ka ago to the present. We perform an ensemble study of 841 model simulations in which key model parameters are systematically varied to determine the parameter values that, with quantified uncertainties, best reproduce the 11.7 ka of surface elevation records derived from ice cores, providing confidence in the modeled GrIS historical evolution. We find that since the Holocene onset, 11.7 ka ago, the GrIS mass loss has contributed 5.3±0.3 m to the mean global sea level rise, which is consistent with the ice-core-derived thinning curves spanning the time when the GrIS and the Innuitian Ice Sheet were bridged. Our results suggest that the ice bridge collapsed 4.9±0.5 ka ago and that the GrIS is still responding to these past changes today, having raised sea level by 23±26 mm SLE $\text{ka}^{-1}$ in the last 500 years. Our results have implications for future mass-loss projections, which should account for this long-term, transient trend.

# 1 Introduction

During the Last Glacial Maximum (LGM), approximately 20 ka ago, Earth was covered by large ice sheets, including the Laurentide, the Fenno-Scandian, the Innuitian, and the Greenlandic ice sheets, and the global mean sea level was 125–134 m lower than it is today (Gulev et al., 2021). Geological evidence suggests that the Greenland Ice Sheet (GrIS) extended to the continental shelf and was connected to the Innuitian Ice Sheet (IIS) at the Nares Strait (England et al., 2006).

Towards the end of the last glacial period, the Bølling-Allerød interstadial brought an abrupt warming to the Northern Hemisphere 14.7 ka ago, followed by the cooling of the Younger Dryas stadial 12.9 ka ago (Rasmussen et al., 2006). The Holocene warm interglacial began 11.7 ka ago, bringing temperatures that were locally up to 15°C warmer in Greenland (Andersen et al., 2004). However, temperature reconstructions vary by several degrees, which can significantly affect the modeled GrIS history (Nielsen et al., 2018). Following the Holocene Thermal Maximum, 7-10 ka ago, Greenland temperatures have shown a long-term decreasing trend (Vinther et al., 2009), but anthropogenic forcing has since reversed the course of natural temperature change, resulting in a global increase in temperatures since pre-industrial times (Eyring et al., 2021).

Accurately modeling the historical evolution of the GrIS is essential for evaluating and calibrating ice sheet models. Ice sheet models respond to climate change over a range of different timescales and are rarely in the steady state (e.g. Lauritzen et al., 2023). However, several ice sheet model studies have overlooked a calibration of their temporal evolution and only focused on the evolution of ice temperature, neglecting other delayed responses, such as bedrock dynamics. For example, the ISMIP6 protocol does not require any calibration (Nowicki et al., 2020), and it has been shown that the majority of the ISMIP6 ensemble simulations underestimate the observed IMBIE consensus mass loss from the Greenland Ice Sheet (The IMBIE Team, 2020; Aschwanden et al., 2021). Recent advances have made up for this by calibrating an ice sheet model to satellite-based gravimetry-derived mass loss data of the GrIS (Aschwanden and Brinkerhoff, 2022), but the satellite-based calibration data period only covers 22 years at the time of writing, and there is no guarantee that it gives a sensible long term response.

Calibrating the model to align with present-day observations of ice thickness and velocities risks capturing only the present-day state while being on a wrong state trajectory; that is, neglecting the long-term memory of the ice sheet and the response of the bedrock to past changes in ice load. These differences in past trajectories affect the projected future mass loss in this century as demonstrated by Aðalgeirsdóttir et al. (2014). Beyond the satellite era and back to the early Holocene, no direct observations are available to inform on the ice sheet history, and ice sheet modeling must rely on proxy data from paleo-climatic records for constraining and validating the long-term transient response of the ice sheet (state trajectory) over these considerably longer timescales. Surface elevation histories, derived from deep ice cores at Camp Century (CC), NGRIP, GRIP, and Dye 3 (See Fig. 5.1), provide such constraints for modeling the GrIS through the Holocene (Vinther et al., 2009). These archives offer valuable insights into the ice sheet's dynamics through the past climate and significantly enhance the robustness of model predictions. Previous attempts to model the ice-core-derived elevation history have not been entirely successful, most likely because the studies did not include the dynamic effect from the IIS on the GrIS in the early Holocene. (Lecavalier et al., 2013; Lecavalier et al., 2017).

In this study, we use the Parallel Ice Sheet Model (PISM) to model the GrIS and the collapse of the IIS bridge during the Holocene. By varying 20 key model parameters in an 841 ensemble-member study, we show that it is possible to model the ice-core-derived elevation histories *if* the grounding line is allowed to advance to the continental shelf *and* the modeled GrIS can form a connection to the IIS. We use this setup to constrain the model parameters for the ensemble and to estimate the GrIS temporal evolution with quantified uncertainties. Using the calibrated model, we investigate the ice sheet mass loss throughout the Holocene and determine the current long-term response of the modeled GrIS and bedrock dynamics.

## 2 Paleoclimatic evidence

When water evaporates over the oceans and precipitates over the GrIS, a fractionation process changes the ratio between the oxygen isotopes in the water. This process is temperature dependent, which was first used by Dansgaard et al., 1969 to infer past temperatures from measurements of oxygen isotopes at CC. The temperatures over the GrIS change locally both because of regional temperature changes and due to surface elevation changes. Vinther et al., 2009 were able to derive a GrIS-wide temperature signal by assuming that the Renland and Aggasiz ice core sites are located within restricted ice domes such that the ice thickness does not change. This GrIS-wide temperature signal was then subtracted from the oxygen isotope signals at CC, NGRIP, GRIP, and Dye 3 to derive local surface elevation histories, having adjusted from upstream effects.

We use five different ice-core-based temperature anomaly reconstructions described by Nielsen et al., 2018 to account for the uncertainty in the past temperatures. The temperature reconstructions are shown in Fig. 5.12. Reconstruction number 1 and 2 are based on the GRIP ice core using a linear transfer function from Huybrechts, 2002 and quadratic transfer function from Johnsen et al., 1995, reconstruction number 3 is based on the NGRIP ice core again using the transfer function from Huybrechts, 2002, reconstruction number 4 is the GrIS-wide reconstruction from Vinther et al., 2009. Reconstruction number 5 is based on the NGRIP core using an inversion scheme for the isotope diffusion (Gkinis et al., 2014). Reconstruction number 1 is the reconstruction used by the SeaRISE project (Bindschadler et al., 2013). The Holocene climate in Greenland is relatively stable and started with an abrupt warming of approximately 15°C at the glacial-interglacial transition 11.7 ka ago, followed by the Holocene Thermal Maximum ∼8-5 ka ago with temperatures 2-3°C higher than the 20th century mean, and then a general cooling trend until the late 20th century. The Holocene Thermal Maximum is only captured by reconstructions numbers 3, 4, and 5, while reconstructions 1 and 2 suggest a constant Holocene climate.

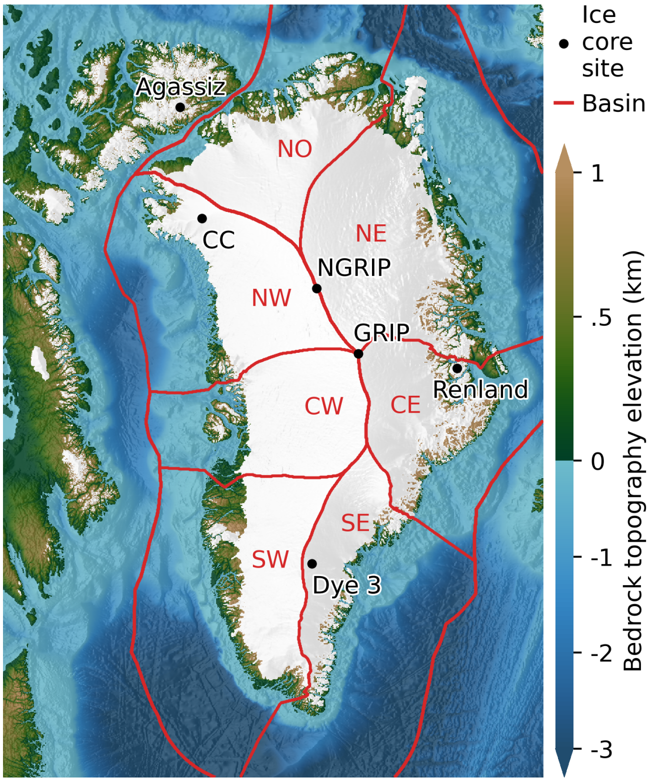

**Figure 5.1:** Model domain showing the present-day bedrock topography elevation from Morlighem, 2022, Jakobsson et al., 2020, and GEBCO Bathymetric Compilation Group, 2023 and the present-day ice cover from Morlighem, 2022 and RGI Consortium, 2023 shown in white. The ice core sites discussed in the text (CC, NGRIP, GRIP, Dye 3, Renland, and Agassiz) are shown on top together with the glacier catchment basins (NW, CW, SW, SE, CE, NE, NO) from Mouginot and Rignot, 2019 and extended out to the Exclusive Economic Zone of Greenland (Flanders Marine Institute (VLIZ), Belgium, 2023) and constitute our extended continental shelf (ECS) domain, see text.

# 3 Model setup

To model the Holocene evolution of the GrIS, we use the open-source Parallel Ice Sheet Model (PISM) version 2.1 (Bueler and Brown, 2009; Winkelmann et al., 2011). PISM is a three-dimensional thermomechanically-coupled ice sheet model that solves both the Shallow Ice Approximation (SIA) and the Shallow Shelf Approximation (SSA) in a hybrid scheme to capture both non-sliding, shearing flow in the slow-moving interior of the GrIS and fast membrane-stress-type flow, sliding over the base in the fast flowing ice streams and outlet glaciers. At the ice-ocean boundary, PISM incorporates sub-grid parameterizations to robustly model grounding line advance and retreat (Gladstone et al., 2010). Model parameters that are introduced in this section will be varied in our ensemble of simulations using the ranges listed in Table 5.1 unless otherwise specified.

## 3.1 Model domain

The model domain is shown in Fig. 5.1 and extends from the continental shelf in the east to the Canadian Arctic Archipelago in the west, covering an area of 6.7 $\times 10^6$ km$^2$. A north polar stereographic projection is used with a standard parallel latitude of 70° N and a central longitude of -45° W corresponding to ESPG 3413. The area is distorted by a maximum of +5% in the north and -11% in the southwest compared to the central longitude and latitude. PISM uses a flat earth approximation and volume is thus not conserved when transforming thickness between projections. All estimated volumes and mass loss rates are given by accounting for the actual grid area.

To allow for a meaningful partitioning of mass between Greenland and Canada, we introduce an Extended Continental Shelf (ECS) mask, which is equal to the Exclusive Economic Zone of Greenland (Flanders Marine Institute (VLIZ), Belgium, 2023). This divides Greenland and Canada at the Nares Strait and Baffin Bay while extending to the continental shelf in the north, east, and south. To also partition the mass loss within the GrIS when the grounding line advances beyond present-day positions, we extend the basins from Mouginot and Rignot, 2019 to the ECS by nearest neighbor extrapolation.

The present-day bedrock topography over Greenland is from BedMachine v5 (Morlighem, 2022), and extended with IBCAO v4.2 (Jakobsson et al., 2020) and GEBCO Bathymetric Compilation Group, 2023 to cover the larger domain, in that order of preference to get the best bedrock available.

At the lateral boundary, a Dirichlet boundary condition of zero ice thickness is used, and the influence of the majority of the Laurentide Ice Sheet is thereby neglected. The north and south are bounded by the open ocean, while Iceland and Svalbard are just visible towards the east. At the base of a 2 km deep bedrock thermal layer, the thermal heat flux from Shapiro, 2004 is applied constantly in time.

## 3.2 Surface mass balance

Determining the surface mass balance (SMB) of the GrIS is challenging, and regional climate models (RCMs), such as RACMO, not only simulate the atmospheric conditions over the GrIS but also incorporate a detailed snowpack model to simulate precipitation, melt, percolation, refreezing, and sublimation processes (Noël et al., 2019).

Given the complexity of including all these processes, it is not feasible to run the RCM over thousands of years, as needed in our study, and we instead apply a Positive Degree Day (PDD) scheme to calculate the surface melting. This approach bases the SMB solely on temperature, $T$, and precipitation, $P$. In the PDD scheme, surface melt is proportional to the extent to which the temperature exceeds the freezing point (e.g. Braithwaite, 1985). We use two constants of proportionality: one for snow, $f_{\mathrm{s}}$, and another for ice, $f_{\mathrm{i}}$.

To force the PDD model, we use a 12-month reference climatology based on the multi-year monthly averages of temperature and precipitation for the period 1960–1989 from the RACMO RCM. Since our model domain is not covered by a single RACMO simulation, we combine different simulations (see Fig. 5.14). We looked at three areas for rainfall data: Greenland, the Northern Canadian Arctic Archipelago, and the Southern Canadian Arctic Archipelago (Noël et al., 2018), treating areas outside these regions as having no rainfall. For temperature, we used RACMO2.3p2 at 5.5 km for Greenland (Noël et al., 2019) and combined it with a broader 11 km simulation (Noël et al., 2015) for the rest of the area. The mean precipitation and summer temperatures from the resulting climatology are shown in Fig. 5.13.

We account for historical temperature changes using the same domain-wide anomalies as in Nielsen et al., 2018, i.e., by adding a domain-wide, spatially uniform temperature anomaly, $\Delta T$, that varies in time, and a lapse rate adjustment, $\Gamma$, of the surface temperature relative to the RCM surface topography. Since the vapor pressure approximately scales exponentially with temperature in the Clausius-Clapeyron relation, we account for historical precipitation changes by scaling the reference precipitation field with a time-dependent scaling factor $\exp(\omega(\phi)\Delta T(t))$. Here, $\omega$ has the latitude dependence

$$\omega(\phi(x,y)) = \begin{cases} \omega_{\downarrow} & \phi \leq \phi_{\downarrow} \\ \omega_{\downarrow} + \dfrac{\phi - \phi_{\downarrow}}{\phi_{\uparrow} - \phi_{\downarrow}}(\omega_{\uparrow} - \omega_{\downarrow}) & \phi_{\downarrow} \leq \phi \leq \phi_{\uparrow} \\ \omega_{\uparrow} & \phi_{\uparrow} \leq \phi \end{cases}, \tag{5.1}$$

where $\phi$ is the latitude and $\phi_{\downarrow} = 60°N$ and $\phi_{\uparrow} = 75°N$. In this way, we allow for different precipitation histories in Northern and Southern Greenland, unlike the uniform scaling used by many previous modeling attempts (e.g. Nielsen et al., 2018).

## 3.3 Ocean forcing

Following Aschwanden et al., 2019 we take the sub-shelf ocean melt to be separable in space and time

$$\dot{m}(x, y, t) = \dot{m}_x(\phi(x, y))\dot{m}_t(t), \tag{5.2}$$

with the spatial dependence controlling the present-day melt rate given by

$$\dot{m}_x(\phi(x, y)) = \begin{cases} \dot{m}_\downarrow & \phi \leq \phi_\downarrow \\ \dot{m}_\downarrow + \dfrac{\phi - \phi_\downarrow}{\phi_\uparrow - \phi_\downarrow}(\dot{m}_\uparrow - \dot{m}_\downarrow) & \phi_\downarrow \leq \phi \leq \phi_\uparrow \\ \dot{m}_\uparrow & \phi_\uparrow \leq \phi \end{cases}, \tag{5.3}$$

where $\phi_\downarrow = 71°N$ and $\phi_\uparrow = 80°N$ while $\dot{m}_\downarrow$ and $\dot{m}_\uparrow$ are the upper and lower melt values which we will vary. To allow the formation of an ice bridge to Canada, the sub-shelf melt rate is scaled by

$$\dot{m}_t(t) = \begin{cases} 0 & t \leq \tau \\ \dfrac{t - \tau}{\Delta\tau} & \tau \leq t \leq \tau + \Delta\tau \\ 1 & \tau + \Delta\tau \leq t \end{cases}, \tag{5.4}$$

such that there will be no ocean melt for times earlier than $\tau$, while it increases to present-day values in the time $\Delta\tau$ inspired by the rapid change in ocean temperatures found by Clark et al., 2020. In addition to sub-surface melt, ice is calved off at the oceanfront at a rate that is proportional to the tensile von Mises stress and inversely proportional to a characteristic parameter, $\sigma_{\max}$ (Morlighem et al., 2016). Additionally, all ice thinner than $H_{\text{cr}}$ is calved off, and a eustatic sea level forcing from Imbrie and McIntyre, 2006 is applied, changing the ocean level by 130 m in the last 19 ka.

## 3.4 Ice dynamics

The constitutive relation that relates the strain rate, $\dot{\epsilon}_{ij}$, to the stress, $\tau_{ij}$, in the ice sheet is

$$\dot{\epsilon}_{ij} = EA\tau_{\text{e}}^{n-1}\tau_{ij}, \tag{5.5}$$

where $E$ is the enhancement factor, $\tau_{\text{e}}$ is the effective deviatoric stress, $n$ is the creep exponent, and $A$ is the ice softness which depends on temperature, pressure, and water content of the ice. The enhancement factor and the creep exponents are taken to be different for the SIA and the SSA, and we use $E_{\text{SSA}} = 1.3, n_{\text{SIA}} = 3$ while we vary $E_{\text{SIA}}$ and $n_{\text{SSA}}$. The basal sliding velocity $\mathbf{u}_{\text{b}}$ in the SSA is related to the basal shear stress $\tau_{\text{b}}$ through the pseudo-plastic power law:

$$\tau_{\text{b}} = -\tan(\phi)N_{\text{till}}\frac{\mathbf{u}_{\text{b}}}{u_{\text{th}}^q|\mathbf{u}_{\text{b}}|^{1-q}}, \tag{5.6}$$

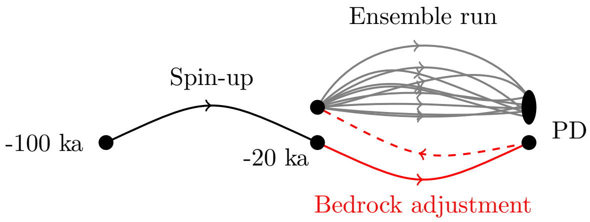

**Figure 5.2:** Schematic of the model ensemble experiment. The ice sheet is initialized at -100 ka using present-day geometry and run through the last glacial at 20 km resolution. The bedrock is then iteratively updated at -20 ka to reduce the modeled present-day bedrock topography deviation. After finding a suitable bedrock topography, the ice sheet model is branched off at -20 ka, and an ensemble of simulations is run at 10 km resolution.

where $q$ is the sliding exponent, $u_{\text{th}} = 100$ m a$^{-1}$ is a characteristic speed. The till friction angle, $\phi$, is parameterized as a continuous function of bedrock topography that increases linearly from $\phi_{\text{min}}$ to $\phi_{\text{max}}$ between $z_{\text{min}}$ and $z_{\text{max}}$. The effective pressure on the till $N_{\text{till}}$ depends on the water level in the till, $W_{\text{till}}$, and the overburden pressure of the ice, $P_0$:

$$N_{\text{till}} = \min\left\{P_0, \tilde{N}_0\left(\frac{\delta P_0}{\tilde{N}_0}\right)^{W_{\text{till}}/W_{\text{till}}^{\text{max}}}\right\}, \tag{5.7}$$

where $W_{\text{till}}^{\text{max}} = 2$ m is the maximal water level in the till and $\tilde{N}_0 = 5.6 \times 10^8$ Pa is a reference pressure simplified from the original formulation of Bueler and van Pelt, 2015 to include the dependence of the till compressibility and the till void ratio. $\delta$ controls the lower bound of the effective pressure, which we will vary in our simulations.

## 3.5 Earth deformation and initialization

The bedrock responds to changes in ice load by the visco-elastic bed deformation model by Lingle and Clark, 1985 and Bueler et al., 2007 with flexural rigidity $D = 5 \times 10^{24}$ N m and upper mantle viscosity $\eta = 1 \times 10^{21}$ Pa s.

We initialize the GrIS by running the model from -100 ka to -20 ka (all times are relative to 2 ka CE) at 20 km grid resolution with initial bedrock topography taken to be the same as the present day (Morlighem, 2022; Jakobsson et al., 2020; GEBCO Bathymetric Compilation Group, 2023). To get a modeled bedrock topography at the end of the simulations as close to the observed present-day bedrock topography as possible we iteratively adjust the bedrock at -20 ka as depicted in Fig. 5.2. A simulation in 20 km resolution is run from -20 ka to present day, after which the modeled bedrock deviation from the observed is used to update the bedrock at -20 ka according to

$$b_{i+1}^0 = b_i^0 + K(b^{\text{obs}} - b_i^1), \tag{5.8}$$

where $b^{\text{obs}}$ is the observed present-day topography (Morlighem, 2022; Jakobsson et al., 2020; GEBCO Bathymetric Compilation Group, 2023), $b_i^0$ is the modeled bedrock topography at -20 ka and $b_i^1$ is the modeled bedrock topography at present day. The relaxation parameter $K = 0.7$

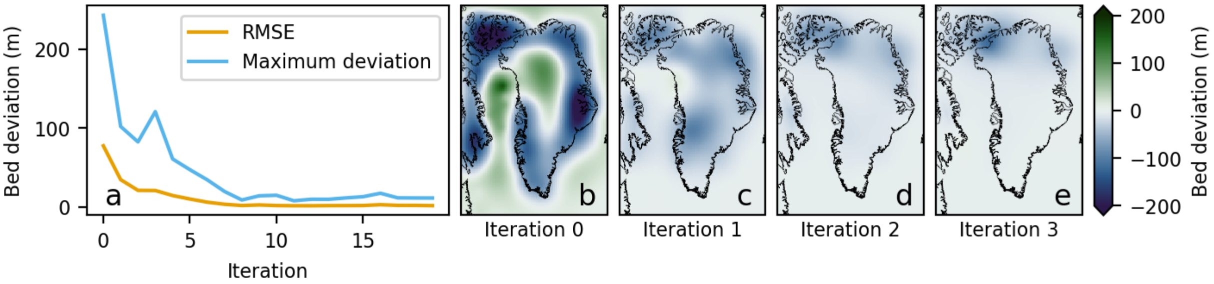

**Figure 5.3:** Iterative bedrock adjustment. (a) The modeled present-day bedrock elevation deviation compared to (Morlighem, 2022; Jakobsson et al., 2020; GEBCO Bathymetric Compilation Group, 2023). (b–e) shows the zeroth to the third iteration of the modeled present-day bedrock elevation deviation from observed.

is used to prevent overcompensation that leads to unwanted deglaciation. Using this method, the RMSE of the bedrock went from 77.4 m to 3.3 m after 20 iterations, as shown in Fig. 5.3.

At -20 ka, the run is branched using the best $b^0$ from the bedrock adjustment, and an ensemble of simulations is run at 10 km grid resolution until the present day, varying the 20 key parameters listed in Table 5.1.

## 4 Bayesian inference

| Parameter | Description | Range | Estimates | | | | |
|---|---|---|---|---|---|---|---|
| | | | Combined | CC | NGRIP | GRIP | Dye 3 |
| Atmosphere | | | | | | | |
| $\Delta T$ | Temperature reconstruction | 1—5 | 1 | 1 | 4 | 2 | 3 |
| $f_s$ | PDD parameter for snow (mm K$^{-1}$ d$^{-1}$) | 5.7—8.9 | 6.5±0.7 | 7.1±0.8 | 7±1 | 7.5±0.7 | 7.8±1.0 |
| $f_i$ | PDD parameter for ice (mm K$^{-1}$ d$^{-1}$) | 7—10 | 7.7±0.6 | 8.5±0.8 | 8.6±0.8 | 8.7±0.9 | 8.4±0.7 |
| $\Gamma$ | Atmospheric lapse rate (K km$^{-1}$) | 4—9 | 5.4±0.7 | 7±1 | 6±1 | 6±1 | 6±1 |
| $\omega_\downarrow$ | Precipitation scaling south of 60°N (% K$^{-1}$) | 0—4.5 | 2±1 | 2±1 | 2±1 | 2±1 | 2±1 |
| $\omega_\uparrow$ | Precipitation scaling north of 75°N (% K$^{-1}$) | 0—9 | 2±1 | 3±2 | 2±1 | 4±2 | 3±2 |
| Ocean | | | | | | | |
| $H_{\mathrm{cr}}$ | Threshold for thickness calving (m) | 50—150 | 96±17 | 87±25 | 97±30 | 112±30 | 106±30 |
| $\sigma_{\mathrm{max}}$ | Characteristic stress (MPa) | 0.8—1.2 | 0.92±0.09 | 1.03±0.10 | 1.0±0.1 | 1.0±0.1 | 1.0±0.1 |
| $\dot{m}_\downarrow$ | Melt rate south of 71°N (m a$^{-1}$) | 300—500 | 394±29 | 409±65 | 400±56 | 391±56 | 391±50 |
| $\dot{m}_\uparrow$ | Melt rate north of 80°N (m a$^{-1}$) | 10—30 | 20±6 | 19±6 | 21±6 | 19±6 | 19±5 |
| $\tau$ | Ocean melt onset (ka) | 4—8 | 5.6±0.6 | 5.5±0.7 | 6±1 | 6±1 | 6±1 |
| $\Delta\tau$ | Ocean melt set in time (ka) | 0—2 | 1.1±0.5 | 1.1±0.6 | 0.9±0.6 | 1.0±0.6 | 0.7±0.6 |
| Dynamics | | | | | | | |
| $n_{\mathrm{SSA}}$ | Creep exponent for the SSA (1) | 3.2—3.4 | 3.28±0.04 | 3.35±0.04 | 3.33±0.04 | 3.25±0.04 | 3.23±0.03 |
| $E_{\mathrm{SIA}}$ | Enhancement factor for the SIA (1) | 2.5—3.3 | 3.0±0.2 | 2.7±0.2 | 2.9±0.2 | 3.1±0.2 | 3.1±0.2 |
| $q$ | Basal sliding power coefficient (1) | 0.7—0.9 | 0.82±0.05 | 0.79±0.05 | 0.81±0.06 | 0.80±0.06 | 0.83±0.06 |
| $\delta$ | Effective pressure parameter (%) | 1.5—2.5 | 2.1±0.2 | 2.0±0.2 | 2.0±0.3 | 2.0±0.3 | 2.1±0.3 |
| $\phi_{\mathrm{min}}$ | Minimal till friction angle (°) | 5—10 | 8±1 | 8±1 | 7±1 | 7±1 | 8±1 |
| $\phi_{\mathrm{max}}$ | Maximal till friction angle (°) | 40—45 | 43±1 | 43±2 | 42±1 | 43±1 | 43±1 |
| $z_{\mathrm{min}}$ | Till friction cutoff elevation (m) | -600—-300 | -421±60 | -481±80 | -443±84 | -433±80 | -447±77 |
| $z_{\mathrm{max}}$ | Till friction cutoff elevation (m) | 0—500 | 271±172 | 238±118 | 231±134 | 252±154 | 271±146 |

**Table 5.1:** List of the 20 parameters that are varied in our ensemble of simulations. The temperature reconstruction is sampled discretely. The estimated parameter values are given as the mean plus minus the standard deviation of the posterior PDFs except for the temperature reconstruction, which is the mode of the posterior PDFs.

To account for model uncertainty and determine the importance of the model parameters, we run an ensemble of simulations from -20 ka to present day, varying the 20 parameters listed in Table

5.1. The 20 parameters share the same dynamical parameters as those varied by Aschwanden and Brinkerhoff, 2022, while the oceanic and atmospheric parameters chosen reflect the change in our model setup. To effectively sample the parameter space, 841 parameters are drawn using the second-order orthogonal Latin Hypercube Sampling (LHS) design (Tang, 1993). This ensures that all pairs of parameters are sampled uniformly and reduces the risk of clustering. The parameters are sampled uniformly over the ranges specified in Table 5.1 which are based on the calibration by Aschwanden and Brinkerhoff, 2022 and our previous model attempts.

For each of the four ice core sites, we calculate the likelihood, which is the probability of observing the ice-core-derived elevation history given the modeled elevation change with model parameters $\mathbf{m}$

$$\rho(\mathbf{h}_i^{\text{obs}}|\mathbf{m}) \propto \prod_j \exp\left(-\frac{\left(h_{i,j}(\mathbf{m}) - h_{i,j}^{\text{obs}}\right)^2}{2\sigma_i^2\beta}\right), \tag{5.9}$$

where $i$ denotes the ice core site and $j$ is the time step of the ice core samples to which the modeled elevations are interpolated. $\sigma_i$ are the uncertainties given by Vinther et al., 2009 which are constant in time. In this way, present-day and past surface elevations are given equal weight, and the likelihoods are thus not biased toward present-day configuration. Following Aschwanden and Brinkerhoff, 2022, the parameter $\beta = 100$ is introduced to account for the autocorrelation of the uncertainties such that estimated surface elevation has a standard deviation that is similar to the observed uncertainties $\sigma_i$. This effectively reduces the number of degrees of freedom by a factor of 100 such that the decorrelation time becomes 2000 years.

Additionally, we calculate the combined likelihood of the ice-core-derived elevation changes to agree with the modeled elevation change for all sites. This likelihood is taken to be proportional to the product of the four individual likelihoods, neglecting any spatial correlation between the drill sites:

$$\rho(\mathbf{h}^{\text{obs}}|\mathbf{m}) \propto \prod_{i=1}^{4} \rho(\mathbf{h}_i^{\text{obs}}|\mathbf{m}). \tag{5.10}$$

The posterior joint probability density functions are then given by Bayes's theorem

$$\rho(\mathbf{m}|\mathbf{h}_i^{\text{obs}}) = \frac{\rho(\mathbf{h}_i^{\text{obs}}|\mathbf{m})}{\rho(\mathbf{h}_i^{\text{obs}})}\rho(\mathbf{m}), \tag{5.11}$$

where the prior distribution $\rho(\mathbf{m})$ is taken to be uniform within the intervals listed in Table 5.1. From the five posteriors, we get five probability density functions of ice sheet evolution through the Holocene from which we estimate relevant observables listed in Table 5.2. Unless otherwise specified, all model results are given using the estimates from the combined posterior probability density function.

To evaluate the effectiveness of the sampling, we compute the effective sampling size for each of

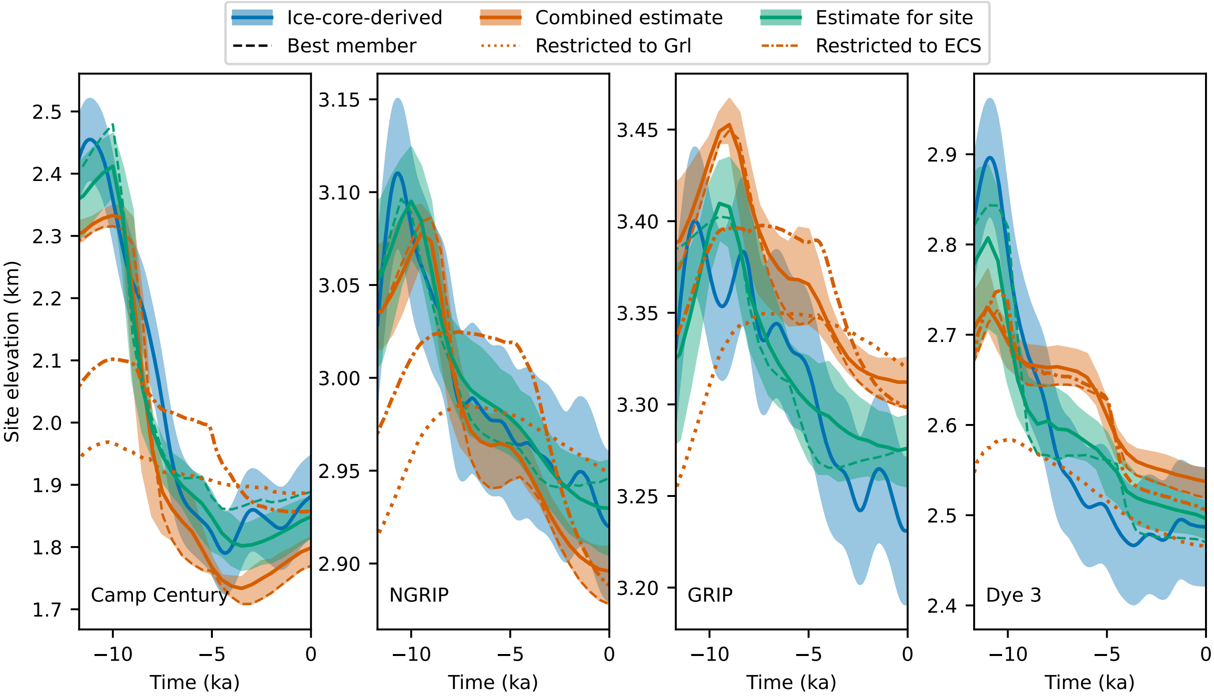

**Figure 5.4:** Observed and modeled surface elevation over the last 11.7 ka for the ice core sites, CC, NGRIP, GRIP, and Dye 3. The blue lines are the ice-core-derived surface elevations from Vinther et al., 2009, and the blue envelopes denote one standard deviation. The orange solid lines represent the combined estimate for all sites, while the green solid lines are the individual estimates for each ice core site. The shaded orange and green envelopes denote the estimated 16-84 quantile ranges. The dashed lines are the ensemble members with the highest likelihood for each site (green) and the highest combined likelihood (orange). The orange dotted and dash-dotted lines are simulations with the same parameters as the best ensemble member but restricted to ECS (dash-dotted) and the present-day land margin of the GrIS (dotted).

our five posteriors:

$$n_{\text{eff}} = \frac{\left(\sum_k \rho(\mathbf{h}_i^{\text{obs}}|\mathbf{m}_k)\right)^2}{\sum_k \rho(\mathbf{h}_i^{\text{obs}}|\mathbf{m}_k)^2}, \tag{5.12}$$

where $k$ denotes the sample member.

# 5 Results

## 5.1 Surface elevation evolution

Figure 5.4 shows the modeled and the ice-core-derived surface elevations during the Holocene for the four ice-core sites. The individual estimates (green) for each site match the observed (blue) and reproduce the large thinning observed at CC and Dye 3 as well as the more moderate thinning in the interior at GRIP and NGRIP with RMSEs between 12 and 53.6 m. The combined estimated elevation (orange) is lower at CC and Dye 3 at the Holocene onset, while it is too high at GRIP compared to the individual estimates. Two simulations were restricted from advancing beyond the present-day GrIS coast, and the ECS mask was run with the same parameters as the ensemble member with the highest combined likelihood. The simulation restricted to the present-day GrIS coast could not reproduce the observed thinning at CC, NGRIP, and Dye 3,

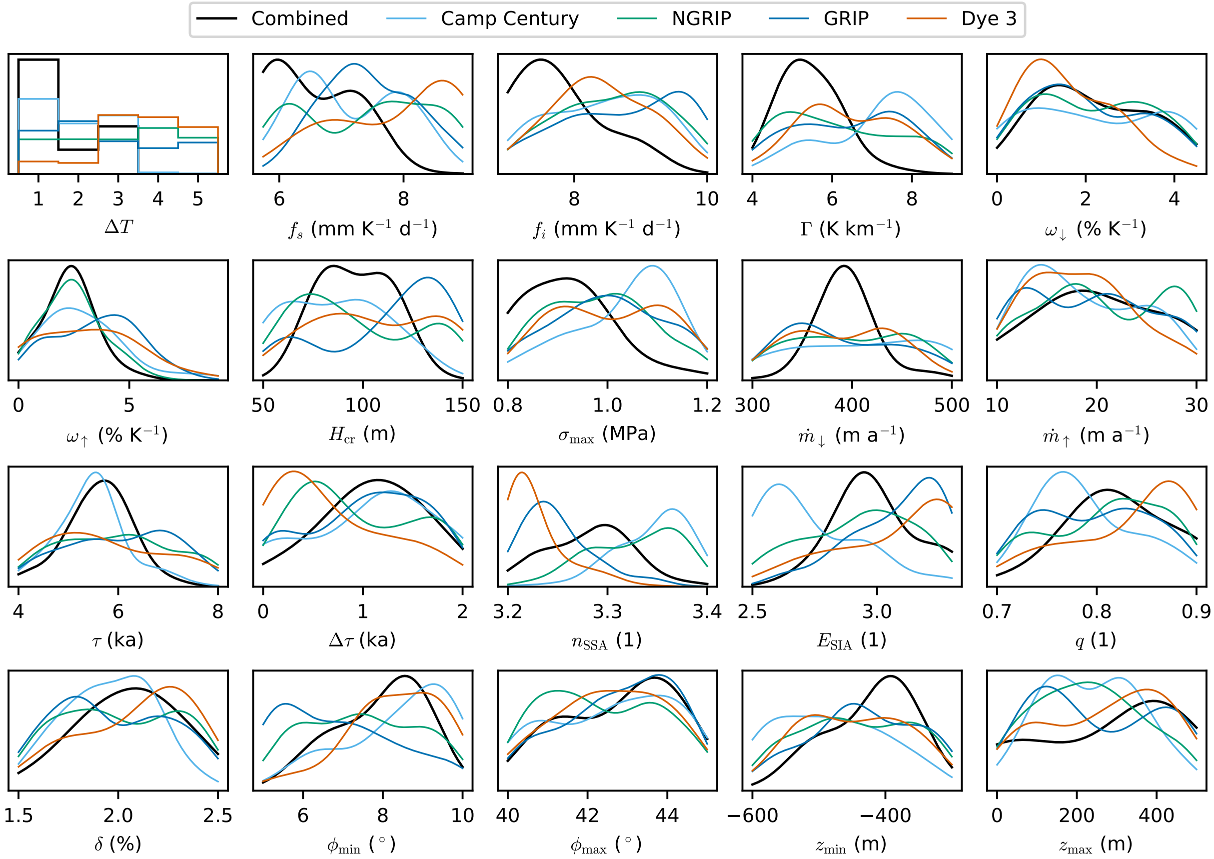

**Figure 5.5:** Kernel density estimates of the inferred marginal probability densities for the 20 model parameters that we varied. The units on the y-axes are the inverse of that of the x-axes.

showing the importance of a dynamic grounding line. The simulation restricted to not advancing beyond the ECS performed better but also failed to reproduce the thinning at CC, showing the effect of including the IIS when modeling the GrIS Holocene history. The RMSEs to the four ice-core-derived elevation histories are listed in Table 5.2 for the five estimates.

## 5.2 Inferred parameters

The ice-core-derived surface elevation histories constrain the model parameters, and the marginal distributions for each of the five posteriors are shown in Fig. 5.5, and the estimated parameters are listed in Table 5.1. The inferred parameters are not equally well constrained and are constrained differently for each ice core site.

Notably, the estimated enhancement factor of the SIA, $E_\mathrm{SIA}$, differs substantially between the sites. At CC, it is estimated to be 2.7±0.2, while at GRIP, it is estimated to be 3.1±0.2. The estimated creep exponent for the SSA, $n_\mathrm{SSA}$ also varies between the sites and has a higher estimate for CC and NGRIP than for GRIP and Dye 3.

Of the five different temperature reconstructions, the first temperature reconstruction from GRIP is the coldest through the Holocene and does not have a clear signal of the Holocene Thermal Maximum. It has the highest combined likelihood at 61% and the highest likelihood for CC at 40%, where the largest thinning is happening. The second temperature reconstruction from GRIP is more than a degree warmer in the early Holocene and does not perform as well as the first one. The fourth and fifth temperature reconstructions are the warmest trough the Holocene and have near zero likelihood at CC, while the fourth is the most likely for NGRIP and Dye 3.

The northern accumulation parameter, $\omega_{\uparrow}$, is more constrained by the northern sites CC and NGRIP, where it has the most influence. Likewise, the southern accumulation parameter, $\omega_{\downarrow}$, is most constrained by Dye 3. Both parameters are estimated to be $2 \pm 1\%\ \mathrm{K}^{-1}$ which is substantially lower than the default of $7.3\%\ \mathrm{K}^{-1}$ introduced by Huybrechts, 2002 resulting in less accumulation in the warm periods of the Holocene and more accumulation in the cold glacial where the ice sheet builds up.

The onset of sub-shelf ocean melt seems very well constrained by the CC surface elevation history and is estimated to happen at 5.6±0.6 ka before present. In the sections below, we will refer to the combined estimate (Fig. 5.5).

## 5.3 Modeled Holocene evolution

From the branch-off point at -20 ka until the onset of the Holocene (11.7 ka ago), the modeled ice sheet bridges the gap between Canada and Greenland over the Baffin Bay and the Nares Strait. Figure 5.6 shows the ice sheet configuration at -12 ka, -9 ka, and at present day, and Fig. 5.7 shows the volume and area evolution from the branch-off point until present day. At -12 ka, the ice sheet reaches its glacial maximum extent and is grounded to the continental shelf and through the Nares Strait. We will take this time step to represent the GrIS at the LGM in the following.

At the LGM, the GrIS has a modeled grounded area of $2.96 \pm 0.03\ \mathrm{km}^2$, within the ECS. This is 49% or $0.98 \pm 0.05 \times 10^6\ \mathrm{km}^2$ larger than the present-day modeled area and it is 0.9% larger than the minimum LGM extent and 5.6% smaller than the maximum LGM extent from Leger et al., 2024. Compared to the modeled present-day GrIS, the modeled grounded volume is 6.6±0.4 m SLE larger during the LGM. Additionally, the grounded volume above flotation is 5.3±0.3 m SLE larger, which contributed to the global mean sea level rise.

Outside the ECS the IIS and Laurentide Ice Sheet are cut off at the domain boundary with a Dirichlet boundary condition of zero thickness. This moves the ice divide at Baffin Island further to the east than if it had been connected to a complete Laurentide Ice Sheet. Together they have a grounded area of $1.20 \pm 0.03 \times 10^6\ \mathrm{km}^2$ and a grounded volume of 5.0±0.2 m SLE.

During the Holocene collapse of the IIS, the ice divide at the GrIS moves towards the west and the ice streams reorganize in northern Greenland as shown in Fig. 5.6.

Figure 5.8 shows the rate of change of grounded ice for the ensemble member with the highest combined likelihood for the seven basins of the GrIS. The GrIS rate of change becomes negative at -10.7 ka and peaks at -7.8 ka with a mass loss rate of $548\ \mathrm{Gt\ a}^{-1}$ and after the onset of the sub-shelf melting at 4.95 ka with a mass loss rate of 511 Gt $a^{-1}$. It continues to be negative for the rest of the Holocene except for a few times during the last 2 ka, where the average mass loss rate is 23.7 Gt $a^{-1}$. The mass loss rates are averaged over 50 years.

### 5.4 Present-day configuration

The modeled present-day extent of grounded ice deviates from the observed as shown in Fig. 5.9a. Most notably, it is larger at the Canadian Archipelago, while it fails to cover 0.08±0.01 $km^2$ and falsely covers 0.19±0.01 $km^2$ compared to the observed GrIS extent, including peripheral glaciers and neglecting ice thinner than 10 meters which is taken to be seasonal.

The modeled GrIS at present day has a grounded volume of 9.1±0.1 m SLE, which is 1.5 m SLE larger than the observed grounded volume, including peripheral glaciers (Morlighem, 2022). This can be explained by the ice thickness deviation at the margin of the GrIS shown in Fig. 5.9b.

Figure 5.10 shows the modeled surface speeds and the deviation compared to Solgaard and Kusk, 2023. In the northwest, the modeled ice sheet is thinner than observed at the Humboldt Glacier, where the modeled surface speed is larger than observed. In the northeast, the model fails to capture the flow of the Northeast Greenland Ice Stream but has a faster-flowing ice stream north of it.

The modeled present-day uplift rates are shown in Fig. 5.11a together with GPS-derived GIA uplift rates from Schumacher et al., 2018. Figure 5.11b shows the difference between the modeled present-day bedrock topography and the observed. At present, the bedrock topography has a maximal deviation of 93 m in the area covered by the IIS and an RMSE of 27 m. Figure 5.11c shows the modeled bedrock topography uplift from the LGM at -12 ka to present day, which has a maximum of 509 m over the area covered by the IIS. At Agassiz, the bed uplift is 345±9 m while at Renland, it is 168±9 m, which is a little larger than the bed uplifts of 275 and 110 m respectively used by Vinther et al., 2009 for deriving the surface elevation histories.

## 6 Discussion

### 6.1 Innuitian ice bridge and the present-day response

To accurately model the ice-core-derived elevation history of the GrIS, we included the Canadian Arctic Archipelago in our domain. This inclusion supports the ice bridge connecting the GrIS and the IIS during the last glacial period. In our model, the IIS meets the GrIS at Nares Strait during the LGM. The ice then diverges into two streams: one flowing southwestward, similar to the Smith Ice Stream as suggested by England et al., 2006, and another flowing northeastward. The Smith Ice Stream discharges into the Baffin Bay, which, as proposed by Couette et al., 2022, is covered by an extensive ice shelf that provides buttressing for the western GrIS.

Figure 5.9c illustrates the modeled isochrones of areas last covered by grounded ice. The modeled collapse of the ice bridge in Nares Strait occurs at 4.9±0.5 ka before present, 0.7 ka after the

| Observable | Estimates | | | | | | Restricted | |
|---|---|---|---|---|---|---|---|---|
| | Combined | CC | NGRIP | GRIP | Dye 3 | Prior | Grl | ECS |
| Elevation history RMSE | | | | | | | | |
| CC (m) | 88.1 | 53.6 | 116.8 | 154.3 | 170.7 | 119 | 223.4 | 165.9 |
| NGRIP (m) | 26.8 | 44.9 | 12 | 69.8 | 69.4 | 34.9 | 67.8 | 49.9 |
| GRIP (m) | 58.6 | 123 | 86 | 27.2 | 29.5 | 62 | 64.5 | 59.5 |
| Dye 3 (m) | 99.1 | 153.4 | 116.4 | 87.2 | 55.4 | 106.1 | 123.5 | 88.5 |
| Present-day configuration | | | | | | | | |
| Grounded ice volume (m SLE) | 9.0±0.1 | 9.5±0.3 | 9.1±0.3 | 8.7±0.3 | 8.7±0.2 | 9.0±0.4 | 8.55 | 9.08 |
| Grounded area ($10^6$ km$^2$) | 1.99±0.02 | 2.00±0.03 | 1.94±0.05 | 1.95±0.05 | 1.93±0.04 | 1.95±0.06 | 1.82 | 1.98 |
| Falsely grounded ($10^6$ km$^2$) | 0.19±0.01 | 0.21±0.02 | 0.17±0.03 | 0.18±0.03 | 0.17±0.03 | 0.18±0.04 | 0.07 | 0.19 |
| Missing grounded ($10^6$ km$^2$) | 0.08±0.01 | 0.08±0.01 | 0.11±0.02 | 0.11±0.02 | 0.12±0.02 | 0.10±0.02 | 0.13 | 0.08 |
| Ice thickness RMSE$^\dagger$ (m) | 420.8 | 495.2 | 435.9 | 396.4 | 394.9 | 428 | 313.4 | 418.7 |
| Bed topography RMSE (m) | 27 | 42.2 | 19 | 18.5 | 17.5 | 20.2 | 58.3 | 58.3 |
| Surface speed RMSE$^\dagger$ (ma$^{-1}$) | 84.4 | 80.7 | 79.5 | 82.7 | 82 | 79.1 | 95.3 | 96.3 |
| LGM configuration | | | | | | | | |
| Grounded ice volume (m SLE) | 15.7±0.3 | 16.0±0.7 | 15.8±0.5 | 15.1±0.6 | 15.8±0.7 | 15.3±0.9 | 9.03 | 14.31 |
| Grounded area ($10^6$ km$^2$) | 2.96±0.03 | 2.93±0.03 | 2.93±0.04 | 2.96±0.05 | 3.01±0.05 | 2.93±0.05 | 2.08 | 2.87 |
| dvdt last 500 a (mm SLE ka$^{-1}$) | -23±26 | -31±27 | -74±133 | -52±106 | -75±143 | -60±112 | -18.19 | -70.81 |
| Time of collapse (ka b2k) | 4.9±0.5 | 4.9±0.7 | 6±1 | 6±1 | 5±1 | 6±1 | | |
| $n_{\text{eff}}$ | 9.28 | 41.36 | 151.87 | 99.67 | 28.56 | 841.00 | | |

**Table 5.2:** Estimates of key observables for the past and present of the GrIS, as well as observables for the simulations restricted to the present-day Greenland mask (Grl) and the ECS. All observables are calculated within the ECS mask and do not include Canada. $^\dagger$ RMSEs are calculated within the present-day observed grounded mask.

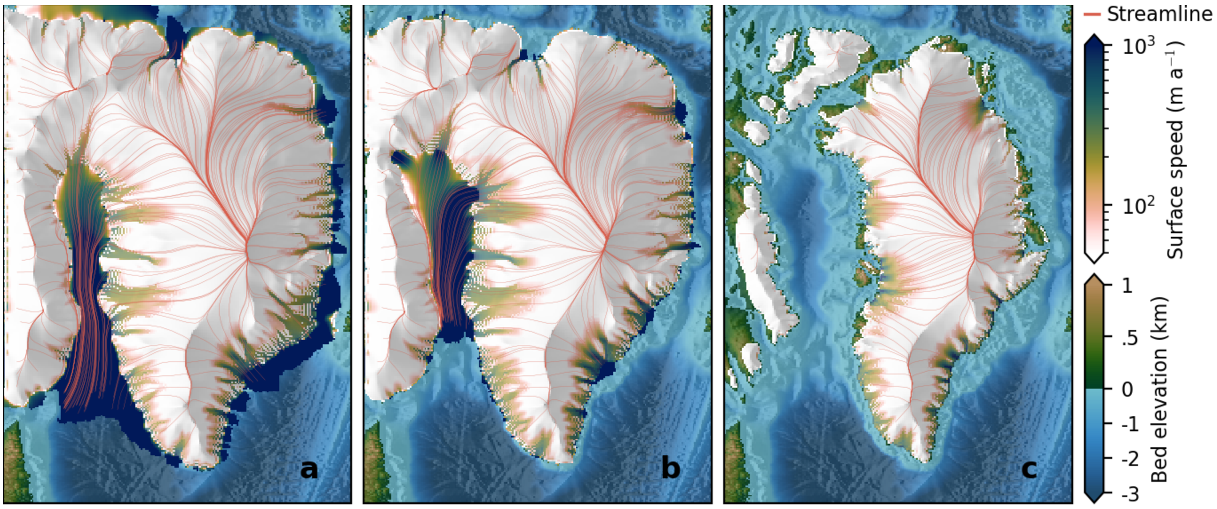

**Figure 5.6:** Time slices showing modeled surface speed, streamlines, bed topography, and ice shelf extent for the ensemble member with the highest combined likelihood at -12 ka (a), -9 ka (b), and present day (c).

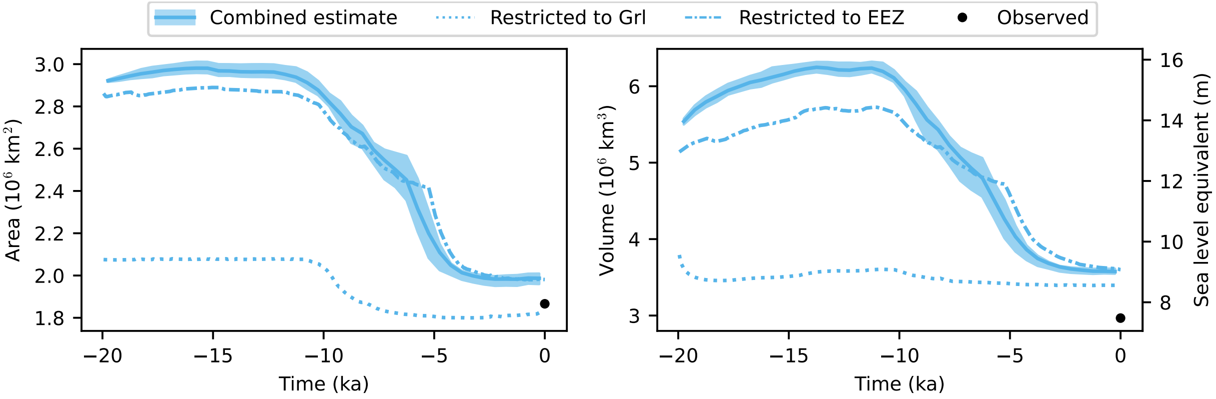

**Figure 5.7:** Modeled evolution of the GrIS grounded area (a) and volume (b). The shaded area denotes the estimated standard deviation.

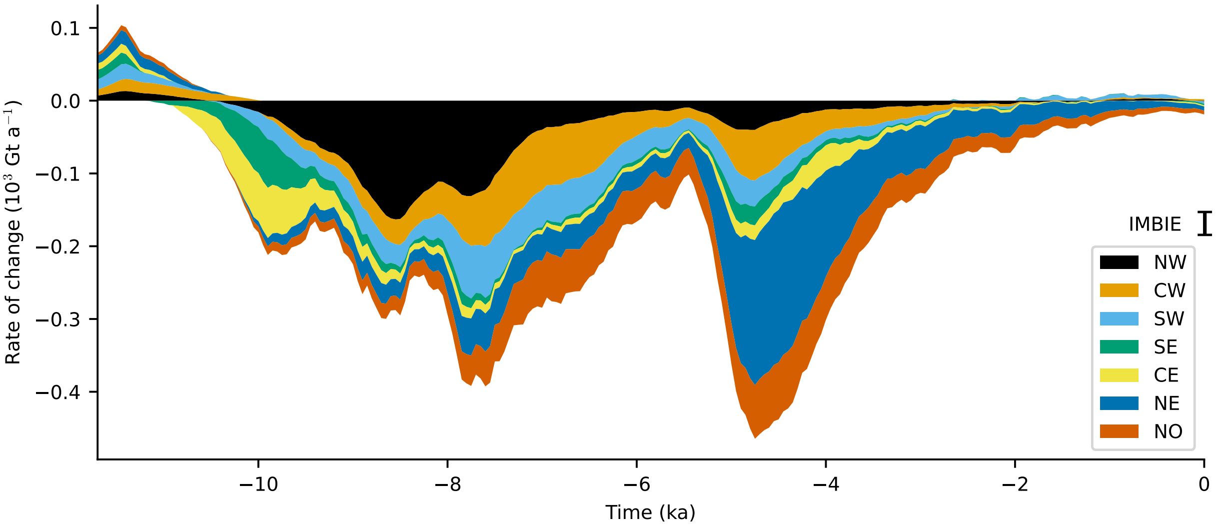

**Figure 5.8:** Rate of change of grounded ice by basin for the ensemble member with the highest likelihood. The mass change is smoothed using a running mean of 500 years, then divided into gain and loss, and then accumulated by basin. The 1992-2020 estimated mass loss rate from The IMBIE Team, 2020 is shown for comparison.

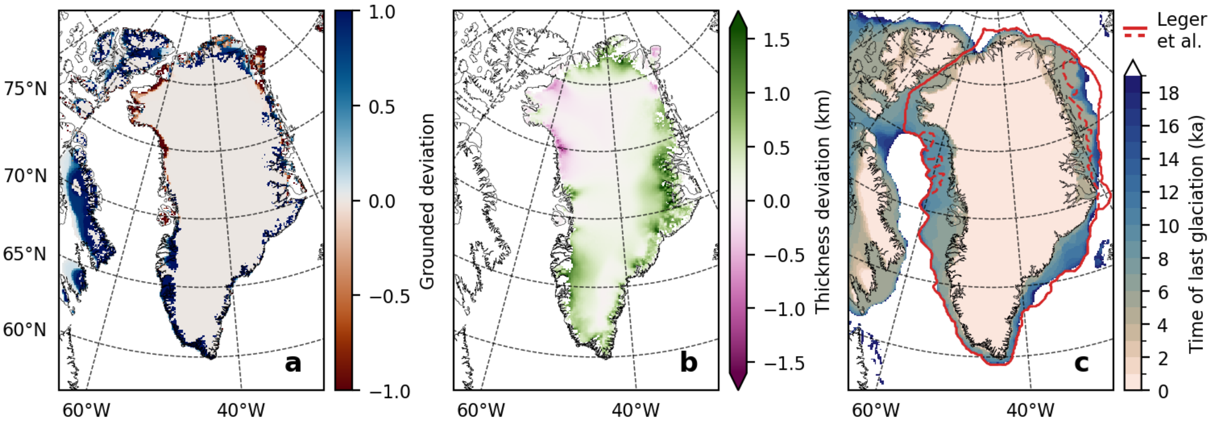

**Figure 5.9:** (a) Modeled present-day grounded extent deviation (modeled-obs) where one corresponds to grounded and zero corresponds to not grounded. (b) Modeled present-day thickness deviation from observed. (c) Isochrones showing the modeled time of the last glaciation together with the maximum (solid line) and minimum (dashed line) LGM extent from Leger et al., 2024.

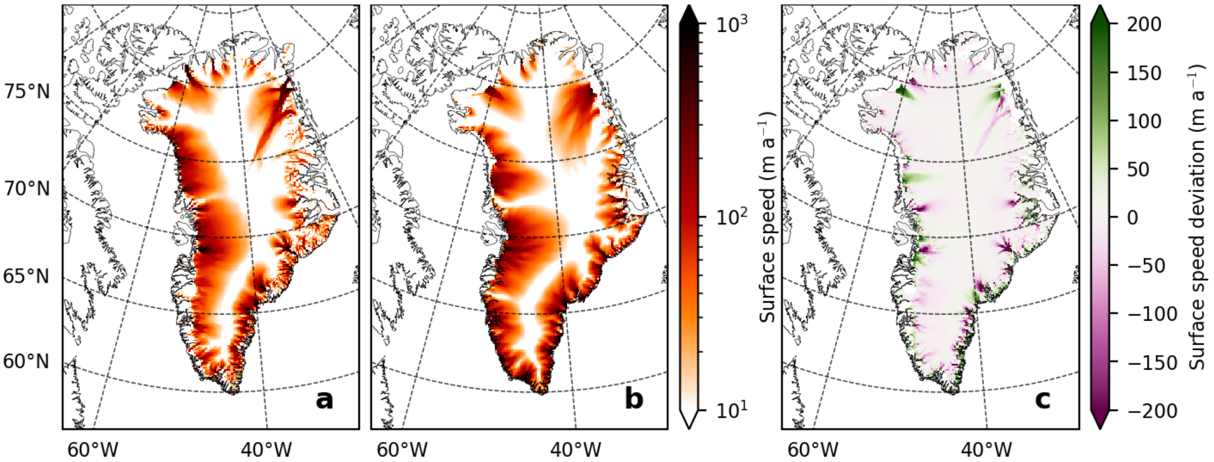

**Figure 5.10:** (a) Observed surface speeds over the GrIS from Solgaard et al., 2021. (b) Modeled present-day surface speeds. (c) Present-day surface speed deviation (mod-obs).

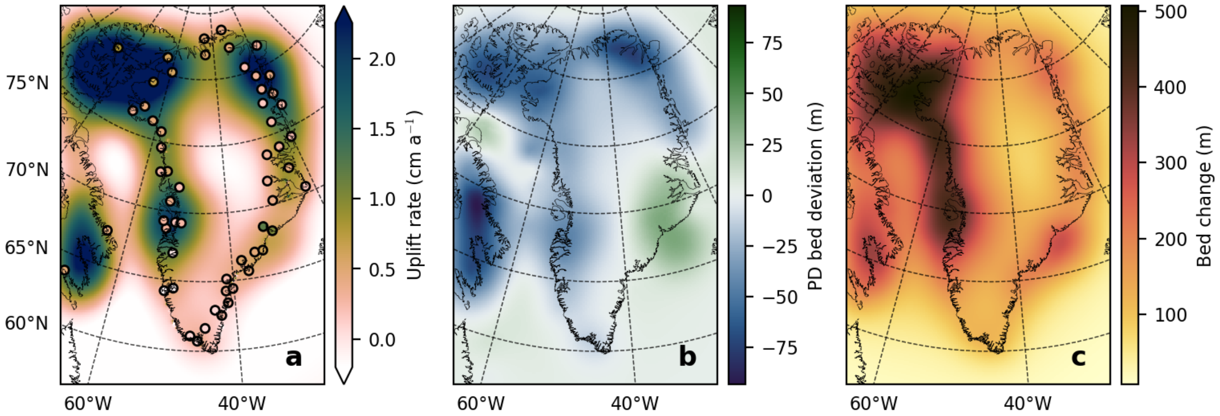

**Figure 5.11:** (a) Modeled present-day bedrock topography uplift rates and GPS-derived uplift rates from Schumacher et al., 2018. (b) Modeled present-day bedrock topography deviation from observed. (c) Modeled bed uplift between -12 ka and present-day.

onset of sub-shelf melting, and about 3 ka later than the findings by England et al., 2006. The ensemble members with earlier onsets of sub-shelf ocean melting become too thin at Camp Century (CC) in the middle of the Holocene, while those with later onsets remain too thick at present (Fig. 5.16). Although not the focus of this study, it may be possible to align the ice sheet evolution with both the elevation histories and the timing of the collapse by increasing the Holocene precipitation beyond present-day levels.

However, the importance of calibrating the GrIS evolution with paleo constraints is underscored when examining the mass change rates of the GrIS over the last 500 years. These rates range from a decrease of 487 mm ka$^{-1}$ to an increase of 105 mm ka$^{-1}$ across the ensemble of simulations. Excluding the simulations that utilize the temperature reconstruction from Gkinis et al., 2014, where the temperature anomaly peaks at 4.5 K during this period, we find that the remaining mass loss rates primarily depend on the timing of the onset of ocean forcing, $\tau$ (Fig. 5.15). This relationship exhibits a strong Pearson correlation coefficient of 0.8. Consequently, the estimated mass loss rate shifts from a prior of -12±40 mm ka$^{-1}$ to a posterior of -23±26 mm ka$^{-1}$. This adjustment highlights the critical role of historical calibration in accurately modeling ice sheet dynamics.

## 6.2 Bedrock uplift

The present-day bedrock RMSE of the ensemble members varies between 11.9 and 70.9 m. This is less than the initial RMSE of 77.4 m before applying any bedrock adjustment but more than the RMSE of 1.47 m that was found for the 12th iteration of the bedrock adjustment scheme. This could partly be because the bedrock adjustment was done at a resolution of 20 km instead of the 10 km resolution of our ensemble, but the spread of the bedrock RMSE indicates that the modeled bedrock topography is very sensitive to the history of the ice load. One way to get a better agreement between the modeled present-day bedrock and the observed could be to make a few bedrock adjustment iterations for each ensemble member, although this would be computationally much more demanding. However, the reported error of Morlighem, 2022 is up to 1000 m at the interior, where the data coverage is sparse, and the RMSE is 145 m over land, so getting a better agreement is of limited value due to the uncertainties in the bedrock topography.

The modeled uplift rates are larger than the GPS-derived GIA uplift rates from Schumacher et al., 2018 in most places. This could be explained by the modeled collapse happening too late and thus not providing enough time for the bed to relax or by the assumed viscosity of the upper mantle being too low. A higher viscosity would, in turn, make the past elevation change smaller, resulting in an earlier collapse.

The viscosity of the upper mantle was not varied in our ensemble, but the default of $10^{21}$ Pa s from Lingle and Clark, 1985 was used. Estimates of the viscosity range several orders of magnitude (Bagherbandi et al., 2022) and Albrecht et al., 2020b identifies a plausible range of viscosities to be $10^{20} - 10^{22}$ Pa s for Antarctica. Varying the viscosity would change the bedrock topography history of the ensemble members even further, giving additional reason for adjusting the bedrock for each member individually.

## 6.3 Validity of elevation histories

The analysis made by Vinther et al., 2009 simplifies the relationships between the O-18 content of ice, temperature, and elevation changes. In particular, it does not account for the effect of an ice shelf over Baffin Bay or the influence of the IIS on the fractionation process along the moisture trajectory from the ocean to the ice core. Lecavalier et al., 2013 presented revised estimates of elevation histories, arguing that the bedrock history along the eastern coastline of Ellesmere Island should be used rather than at the Agassiz location itself while arguing that the IIS complicated the elevation correction before -8 ka.

Using the assumption that the elevation correction to the O-18 signal at the Agassiz ice cores should be taken from the shores, Lecavalier et al., 2017 presented revised temperature anomalies for the Agassiz ice core that, in turn, increased the ice-core-derived surface elevation at CC by 400 m at the Holocene onset.

The elevation histories presented by Vinther et al., 2009 have already been corrected for upstream effects due to ice flow. Ideally, the ice sheet model should be coupled to an atmosphere model that tracks the moisture from evaporation at the ocean to precipitation over the ice sheet and the fractionation of O-18. The modeled O-18 should then be compared directly to that of the observed at the time-dependent ice core site location.

The assumption that the thickness of the Renland ice cap does not change during the Holocene is not consistent with our model results, and we find that the Renland ice cap thins by 399 ± 56 m from the Holocene onset to present day. We believe that this can be explained by the low resolution of the model resolution since the Renland ice cap is only 1200 km$^2$ (Johnsen et al., 1992) and the model cannot capture the topography-sensitive steep descents that limit its lateral extent.

## 6.4 Sampling technique

We used the second-order orthogonal LHS technique to effectively explore the 20 unknown model parameters critical to modeling the ice-core-derived surface elevation histories. This sampling strategy was chosen for its efficiency in covering a high-dimensional parameter space more uniformly compared to simple random sampling, thereby reducing errors in the estimation process. The effective sample size of the combined estimate is only 9.28, suggesting a significant concentration of weight among the samples, and the two most likely members contribute 42% to the estimates. One way to improve upon this could be to implement an adaptive sampling technique that concentrates the sampling density in the parts of the parameter space that have the highest contribution to the estimates, which we only did in an ad-hoc way, arriving at the sample ranges given in Table 5.1.

## 6.5 Inferred parameters

Our analysis revealed that the estimated model parameters differed based on the ice core location used for their constraint. In particular, the enhancement factor for the SIA, the creep exponent for the SSA, the sliding exponent, $q$, and the climate history were constrained differently by the four ice core sites. The estimated parameters constrained by Camp Century (CC) in the northwest stand out with a lower enhancement factor for the SIA and a lower sliding exponent than elsewhere. The estimated parameters constrained by Dye 3 in the southwest stand out by a less sensitive southern precipitation scaling in the past and a smaller creep exponent for the SSA than elsewhere. The choice of temperature anomaly history also substantially impacted the modeled surface elevation histories. The temperature reconstructions without a Holocene Thermal Maximum were found to agree better with the ice-core-derived elevation history at CC, while the temperature reconstructions that did include a Holocene Thermal Maximum were found to agree well with the elevation histories at Dye 3 in the southeast. The ice sheet evolution in the Holocene is a complex result of many dynamical processes and climate forcings. While we have found a plausible range of ice sheet simulations constrained by the ice-core-derived surface elevation histories at four ice core sites, the difference in the individual estimates of model parameters suggests spatial differences that our analysis did not account for, e.g., in the basal geology and sliding, the lithosphere viscosity, or the accumulation rate in the early Holocene (e.g. Nielsen et al., 2018). The differences in the estimated ice flow parameters might also be explained by the poorly resolved outlet glaciers, which result in a lower ice flux. This is often compensated by increasing the enhancement factors. Notably, the Kangerlussuaq Gletscher in eastern Greenland and Sermeq Kujalleq in western Greenland require a resolution of less than 3.6 km, as suggested by Aschwanden et al., 2016, to be properly resolved, which is not feasible for this study. Additionally, it is possible that the ice-core-derived surface elevation records do not provide sufficient constraints for all model parameters.

## 6.6 Climatic forcing

The atmospheric conditions and spatial patterns of temperature and precipitation during the glacial and the early Holocene were possibly quite different from that of present day. The Laurentide Ice Sheet is thought to have both shielded Ellesmere Island from precipitation and, at the same time, deflected the jet stream such that more moisture was transported north of the Laurentide Ice Sheet from the North Pacific Ocean to the Polar regions, making the amount of precipitation over Greenland uncertain (England et al., 2006). Furthermore, the ice shelf at Baffin Bay has likely affected the temperature and precipitation nonuniformly. A full coupling of ice sheets to the atmosphere and ocean would be needed to understand and investigate this effect in detail. However, the probability distributions for the five ice-core-derived temperature reconstructions do provide some insights into this. As mentioned above, the southern surface elevation history at Dye 3 was best fitted with a warm Holocene Thermal Maximum, while the northern CC site was best fitted with a constant Holocene climate. However, due to the bedrock elevation being depressed by up to 500 m in northern Greenland (Fig. 5.11c), the impact on temperature would be in the order of 3-5°C (using the best fit atmospheric lapse rate for CC, see Fig. 5.5), similar to the impact proposed by other studies (e.g. Axford et al., 2021).

Lecavalier et al., 2017 also modeled the Holocene surface elevation change at CC. They used revised temperature anomalies from Agassiz that were 7 K warmer in the early Holocene than the present day, questioning the idea that a Greenland-wide temperature signal could accurately model the ice-core-derived elevation changes. They did, however, not include the buttressing effect of the IIS, which we find to be necessary. We also tried to use the temperature anomalies from Lecavalier et al., 2017 but found that although it did give an elevation change that was similar to the ice-core-derived, the modeled present-day elevation was far too low with the ice sheet retreating far inland in the northwest. However, our assumption of a uniform temperature change over the GrIS is a simplification, but further investigations are beyond the scope of this work.

## 6.7 Holocene evolution and ice mass loss

Overall, our simulations show that the deglaciation in Greenland occurred between around 10 ka and 3.5 ka, where the total area and volume of the GrIS dramatically decreased from its glacial maximum values to approximately the present-day volume and extent (Fig. 5.7). The minimum ice-covered area occurred approximately at -2 ka and slightly increased towards the present, while the ice volume has remained relatively constant over the last millennia. Our simulation shows no clear evidence of a minimum ice volume during the Holocene Thermal Maximum. It ends at the present day with a simulated area and volume that exceed the observed values by 5.9% and 20.5%, respectively (Fig. 5.7).

A previous study by Nielsen et al., 2018 showed that the evolution of the GrIS depends on the assumed climate history through the Holocene. Nielsen et al., 2018 found that the GrIS retreated to a smaller than present-day volume at around 8 ka ago when forced by temperature anomalies that contain the Holocene Thermal Maximum, but their simulations did not include Canada in the domain, and thus initiated their simulation with a GrIS of similar size as at present day. In our simulations, we used the same climate forcing histories as in the study by Nielsen et al., 2018, but we do not find a similar minimum in our simulations for the ensemble members that include the Holocene Thermal Maximum, most likely because the GrIS is too far from equilibrium during the Holocene Thermal Maximum due to the large initial ice sheet. In fact, the simulations that best fit all surface elevation histories are those forced with the climate reconstruction history number 1 (see Fig. 5.5), which did not show any Holocene Thermal Maximum. For this climate reconstruction, our simulated Holocene ice volume follows a similar pattern as found in Nielsen et al., 2018.

The spatial pattern of mass loss rates from the GrIS has shifted significantly during the Holocene (Fig. 5.8). In the earliest part of the Holocene, the rate of mass change was slightly positive in all basins due to an increase in snow accumulation over the GrIS. During the first deglaciation phase between 10 and 5.5 ka ago, the mass loss rate was large in all basins, with the largest mass loss rate in the northwest basin, being about the same rate as all other basins combined. The central west basin also had significant mass loss rates, followed by the north and southwest basins. Towards 5.5 ka, the mass loss rates decreased towards zero, which is also seen in the volume record as a temporary stabilization. Between 5.5 ka and 3.5 ka, after the onset of the sub-shelf melt, a second phase in the deglaciation occurred, with a total higher mass loss rate than the first phase, and now dominated by high mass loss rates from the northeast basin and to a lesser extent from the north and central west basins. These two deglaciation phases are also seen in the total volume (Fig. 7b), with a kink around 5.5 ka ago separating the two phases.

Our simulated Holocene mass loss rates exceed the mass loss rates estimated in a previous study (Briner et al., 2020). Briner et al., 2020 simulated the Holocene evolution of the CW and SW basins and assumed that regions are representative of the entire GrIS. They found the maximal values of mass loss during the Holocene to be 60 Gt $a^{-1}$ and that it would most likely be exceeded within this century with rates of mass loss of 8.8 to 359 Gt $a^{-1}$ depending on the climate scenario which is less than our maximal Holocene rate of mass loss at 548 Gt $a^{-1}$ for the ensemble member with the highest likelihood. Our results show that the spatial pattern of retreat has shifted geographically during the Holocene, and the mass loss rates from the GrIS basins have peaked thousands of years earlier in the northwest and west than in the northeast. We conclude that one basin cannot be representative of the entire GrIS, and thus, our results are not directly comparable to the results by Briner et al., 2020.

# 7 Conclusions

We considered an ensemble of ice sheet model simulations covering both Greenland and the Canadian Arctic Archipelago through the Holocene. In these simulations, we varied 20 key parameters to constrain the ice sheet evolution to ice-core-derived surface elevation histories at four ice-core sites in Greenland. We showed that the inclusion of Canada in the model domain and the ability of the ice sheet to advance beyond the present-day land margin are necessary for accurately modeling the ice-core-derived elevation history.

We found that during LGM, the Greenland ice sheet was connected to the IIS with an ice bridge over Nares Strait. Within the Extended Continental Shelf (ECS), the GrIS had an extent that was 49% larger than the present-day modeled area during the LGM, and it was found to have contributed 5.3±0.3 m SLE to the global mean sea level from LGM to present day. The collapse of the ice bridge at Nares Strait was found to have occurred at 4.9±0.5 ka before the present.

We show that the present mass loss rate is a combined short-term response to the recent climate forcing and long-term dynamical response on millennia timescales due to the deglaciation history. Ignoring outliers with excessive temperature anomalies over the past half-millennium, we find that the mass loss rates over the last 500 years primarily depend on the timing of the onset of ocean forcing during the deglaciation. Bayesian inference modifies our understanding of the previous 500 years' mass loss from a prior estimation of 12±40 mm $ka^{-1}$ to a posterior of 23±26 mm $ka^{-1}$, which is about 5% of the 1992-2020 estimated mass loss rate (The IMBIE Team, 2020) and 7% of the estimated 21st-century committed mass loss rate (Nias et al., 2023). This adjustment underscores the significance of historical calibration in accurately modeling ice sheet behavior and including its long-term response to past climatic changes.

While our study was able to model the ice-core derived surface elevation histories, the most probable ice sheet simulations did not match the timing of the collapse of the ice bridge found by England et al., 2006 or the timing of the retreat found by Leger et al., 2024. We propose that these geologically derived datings could be added as further constraints to the GrIS Holocene evolution in future simulations. This would help reveal limitations in the model and assess the sensitivity of model parameters. We also found that our modeled present-day uplift rates deviated from the GPS-derived uplift rates in northwest Greenland, which is further in line with the timing of our model collapse happening too late. In future studies, these deviations should be used to constrain the mantle viscosity in tandem with accurately determining the timing of the retreat. Overall, our results show that the present-day Greenland ice sheet still responds to the history of deglaciation. This long-term dynamical response is significant and should be included in studies of the present and future mass loss from the Greenland ice sheet.

*Code and data availability.* PISM is an open source software that can be downloaded from github.com/pism/pism (Bueler and Brown, 2009; Winkelmann et al., 2011). Surface elevation data from the four ice core locations are available upon request. The presented RACMO data are available upon request and without conditions from B. Noël (bnoel@uliege.be). Temperature reconstructions can be downloaded from iceandclimate.nbi.ku.dk/data/.

*Video supplement.* A video showing the GrIS evolution trough the Holocene for the most likely ensemble member can be found at doi.org/10.5446/68337

# Appendix

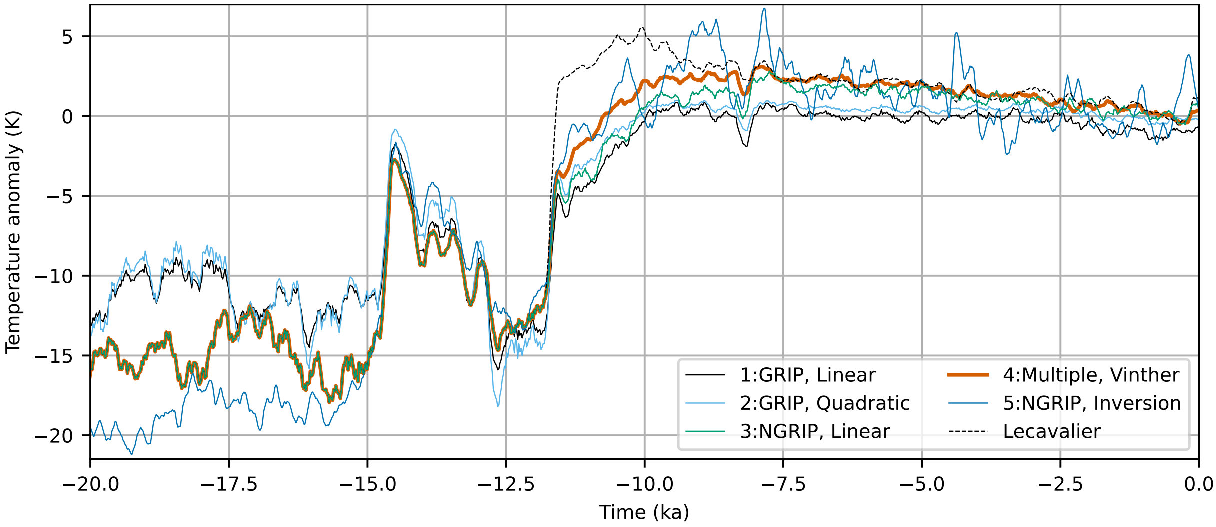

**Figure 5.12:** Paleoclimatic temperature anomalies derived from O-18 measurements at GRIP and NGRIP using linear transfer function (Huybrechts, 2002) and quadratic transfer function from Johnsen et al., 1995 and O-18 measurements at Renland and Agassiz (Vinther et al., 2009) and O-18 measurements at NGRIP using an inversion scheme (Gkinis et al., 2014).

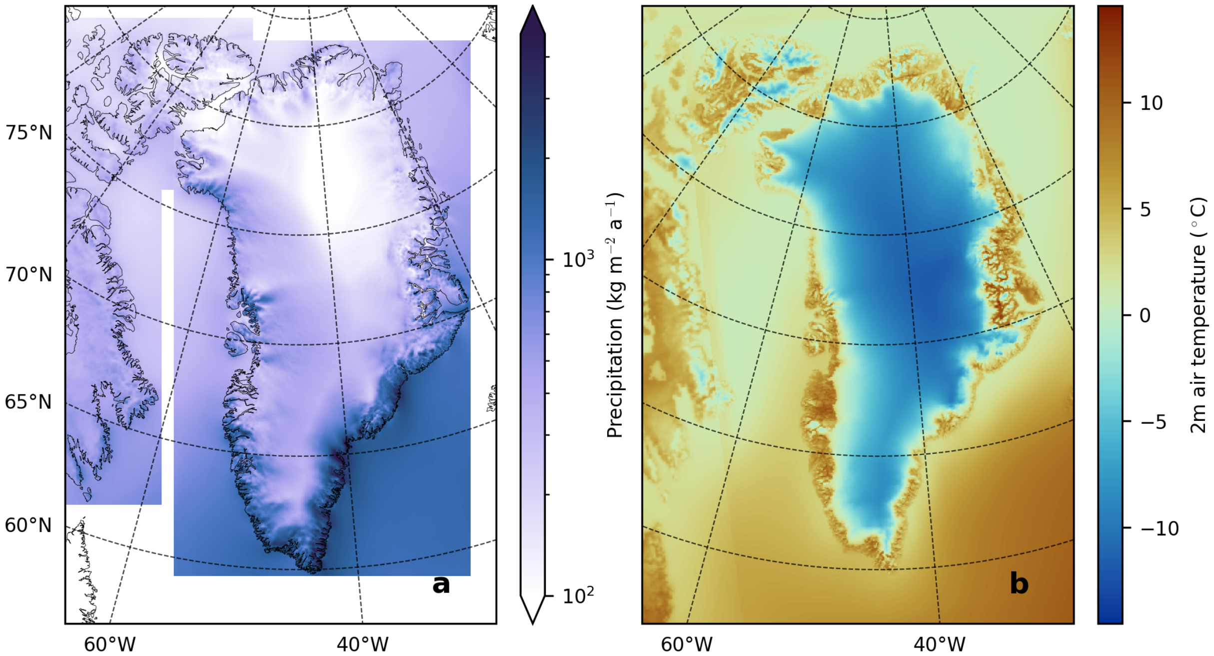

**Figure 5.13:** (a) Annual mean precipitation and (b) summer (June, July, and August) mean 2 m temperatures for our 30-year reference climatology.

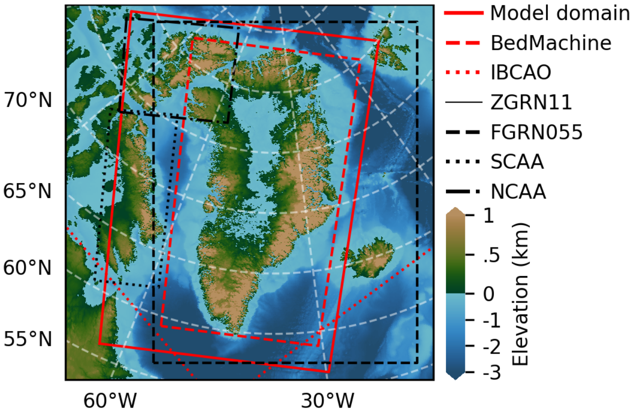

**Figure 5.14:** Overview of different domain boundaries used to patch together the 30-year reference climatology (ZGRN11, FGRN055, SCAA, NCAA) and the bedrock topography (BedMachine, IBCAO, GEBCO).

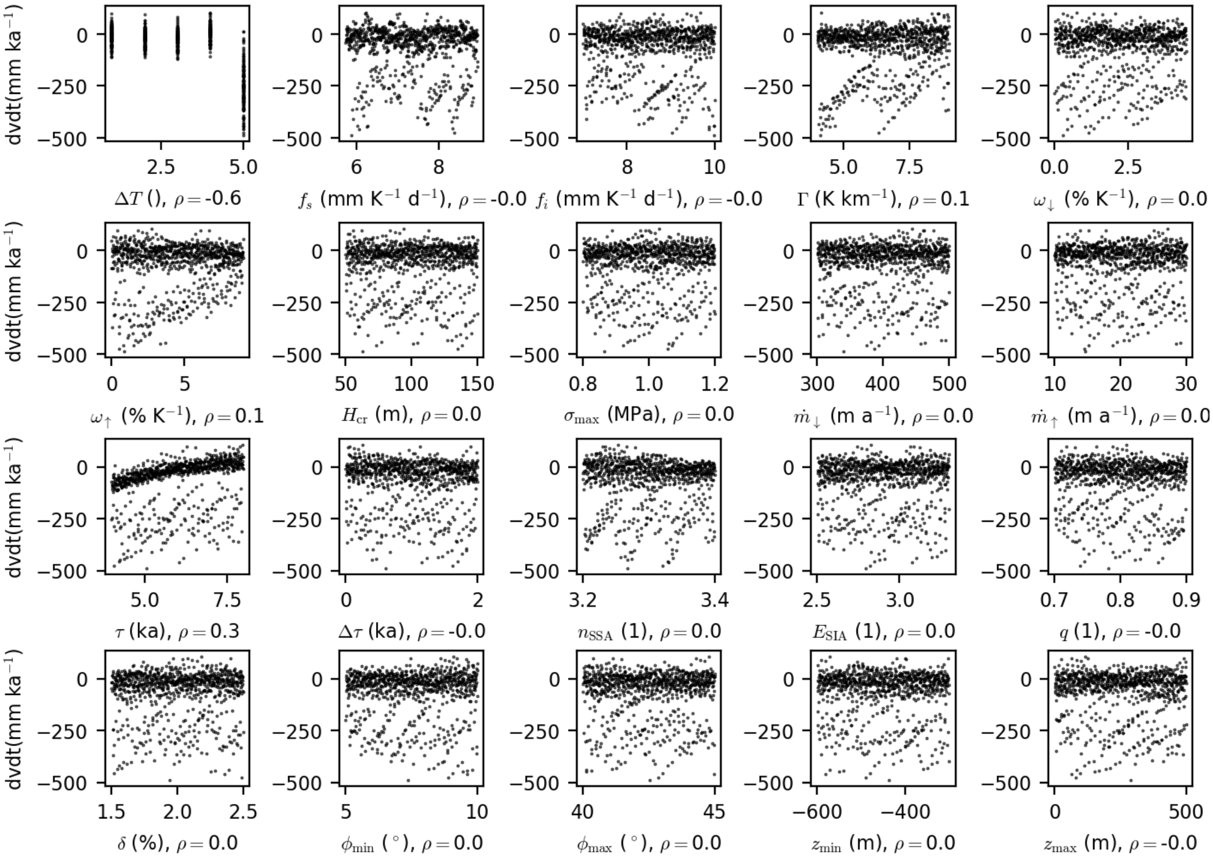

**Figure 5.15:** Scatterplot of the last 500 years of mass loss rates vs each parameter varied in our ensemble. $\rho$ is the Pearson correlation.

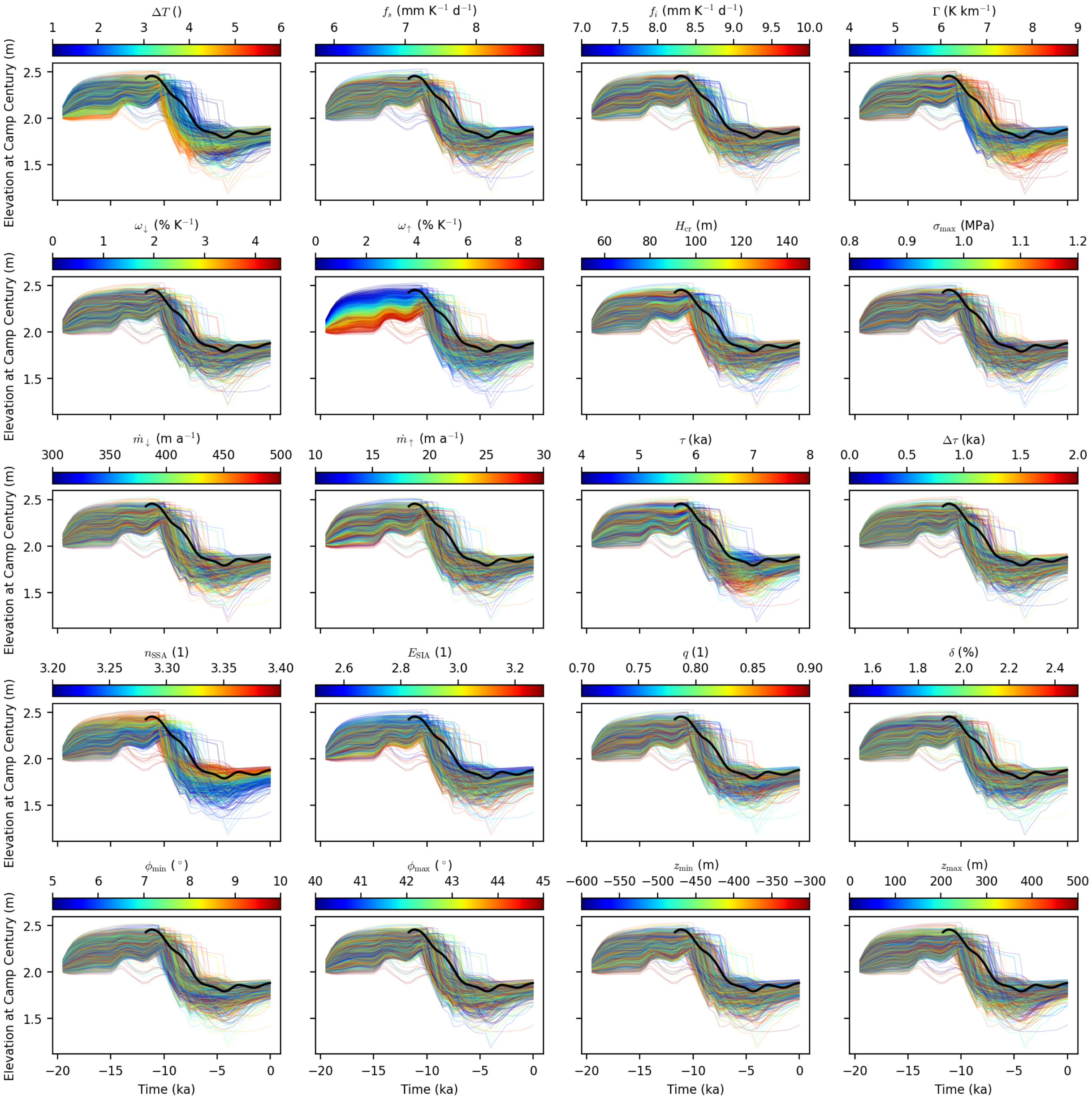

**Figure 5.16:** Modeled surface elevation at Camp Century color coded for each parameter.

Author contributions. ML, CH, and AS designed the study. ML prepared the data, performed the model runs, and carried out the subsequent analysis. All authors discussed and improved the paper.

Competing interests. The authors declare that they have no conflict of interest.

Acknowledgments. ML was funded by the Independent Research Fund Denmark through the project GreenPlanning, grant no. 0217-00244B. CH, NR, and AG received funding from the Novo Nordisk Foundation, grant no. NNF23OC0081251, the Independent Research Fund Denmark (DFF), grant no. 2032-00364B, and the Villum Foundation, grant no. 23261. BN was funded by the Fonds de la Recherche Scientifique de Belgique (F.R.S.-FNRS). We would also like to thank Benoit Lecavalier for providing the temperature anomalies derived from the Agassiz ice core in Lecavalier et al., 2017.

# Chapter 6

# Discussion

Ice flow models are widely used in glaciology and climate science as simplified representations of the physical world. Despite their simplicity, these models display complex, nonlinear responses to changes in their numerous uncertain model parameters and boundary conditions. Designed to mirror the actual system's behavior, they can be tested in idealized scenarios. This allows for a better understanding of individual processes and their reactions to changing conditions, as explored in chapter 3. They can also be constrained by observations to enhance their accuracy and reliability as demonstrated in chapter 5.

Furthermore, estimates of future mass losses from the cryosphere, such as those conducted in the ISMIP and GlacierMIP model runs (Goelzer et al., 2020; Hock et al., 2019), are of high societal importance. These estimates are crucial for societies dependent on glacier melt, reliable sea level rise predictions to properly secure coastlines, and for their impacts on weather systems, which remain not fully understood. To make accurate and precise estimates, it is essential to correctly account for uncertainties. These uncertainties can be divided into two types: epistemic uncertainty, which is attributed to missing information, and aleatoric uncertainty, which arises from random processes like the inter-annual temperature variability.

In this chapter the preceding chapters are discussed in a more general context and ideas on how to improve on them are explored.

## 6.1 The variability of climate forcing

The first manuscript presented in chapter 3, explored the influence of inter-annual temperature variability, an aleatoric uncertainty, on the Greenland Ice Sheet evolution. We found the inter-annual temperature variability to not only result in a spread of ensemble volumes but also to induce a drift on the equilibrium volume. As mentioned in the manuscript our work was inspired by the work from Mikkelsen et al. (2018) who forced an equilibrium model from Oerlemans (2003) with similar inter-annual temperature forcing. Compared to their work, we found the response to be much smaller most likely because in our more complex model a reduction in SMB leads to thinning which in turn leads to reduced discharge across the grounding line and this negative discharge feedback dampens the response. This underlines the necessity to use a more complex model for evaluating responses in ice sheet modeling.

Our study also showed that temperature variability affects the Greenland Ice Sheet's transient response to instantaneous changes in temperature. Future projections of mass loss, à la ISMIP, which depend on both future climate forcing and the initial state of the ice sheet, should therefore consider how to account for inter-annual temperature variability in both the spinup and the projection phases of the simulation.

## 6.2 Bayesian calibration

To account for epistemic uncertainty, we need to identify the known unknowns and quantify our level of knowledge about them, i.e., we need to construct prior probability density functions. To make the predictions more reliable, the range of possible scenarios is constrained by observations through Bayesian inference. To ensure that the calibration is accurate, the range of possible scenarios must cover the uncertainty of the observations to remove the bias of the models while the precision of the calibration is governed by the precision of the observations.

In the manuscript presented in chapter 5, we accounted for 20 unknown parameters to calibrate the Holocene history of the Greenland Ice Sheet based on ice-core-derived elevation histories. However, we did not account for the aleatoric uncertainty associated with temperature variability. This omission was strategic; the uncertainty in mass balance can likely be adequately addressed within the uncertainty of the PDD parameters. Including temperature variability would not have expanded our range of possible scenarios and would have made it more difficult to constrain this additional parameter.

The prior beliefs used was obtained from a mixture of different sources. First of all it was based on the posterior distributions found by Aschwanden and Brinkerhoff (2022) where they calibrated the Greenland Ice Sheet mass loss to observations of present day surface speeds and mass change over the IMBIE period. Secondly, it was based on on the calibration of the PDD parameters we did in chapter 4. Finally, the newly introduced parameters that controlled the timing of ocean melt was inspired by the sudden onset of ocean forcing found by Clark et al. (2020).

Given the vast and mostly empty sampling space and the computational cost of running the ice sheet model, we employed the Latin Hypercube Sampling (LHS) technique. The parameter ranges were subsequently updated in an ad hoc manner, guided by the initial posterior distributions. This adjustment ensured that the ensemble represented the uncertainty range of the observations adequately, while avoiding areas with low likelihood. Alternatively, employing an iterative approach such as the MISER algorithm (Press and Farrar, 1990), which samples more densely in areas of high likelihood, could potentially improve the statistics compared to our simpler approach although it would increase the computational cost. The process was slightly complicated by the fact that parameters were constrained differently at each of the four ice core sites, and the individual likelihoods peaked in different regions of the parameter space having only some overlap. Despite these challenges, the final LHS covered the likelihoods associated with each site to a satisfactory level, quantified by the effective sample sizes ($n_{\text{eff}}$) calculated for each ice core site.

## 6.3 Multiple constraints

The decision to use ice-core-derived elevation histories as a constraint in our model was based on two factors. Firstly, to our knowledge, this approach has not previously been applied to the entire Greenland Ice Sheet, although Lecavalier et al. (2017) employed it for the Camp Century ice core site, excluding the buttressing effect of the Inuitian Ice Sheet. Secondly, the discrepancies between modeled and observed elevations were easily evaluated at each site, allowing us to compute the likelihoods of the model runs. While the elevation histories for the interior likely serve as good local constraints, they may be less effective in constraining the extent of the ice sheet, since the equilibrium ice sheet geometry depends on both the mass balance and the flow parameters as is evident from the Vialov Profile (Vialov, 1958). This raises the question: what other constraints could inform the Greenland Ice Sheet during this period, and how might we combine multiple constraints?

In their study, Briner et al. (2020) modeled the Holocene evolution of the Greenland Ice Sheet within a western subdomain. Although the model runs were not directly constrained, they validated the retreat of the ice sheet against moraine line datings in Western Greenland with promising results. They conducted a goodness-of-fit analysis comparing the glaciated area in the model with the area delineated by the moraine lines. This approach is promising; however, a potentially better method might involve minimizing both the area erroneously glaciated by the model and the area it fails to glaciate, to ensure these deviations do not compensate for each other.

Earlier this year Leger et al. (2024) published a more complete Greenland wide reconstruction of lateral retreat since the LGM based on moraine line datings. The dataset was specifically intended to be used for constraining the Greenland Ice Sheet although it did not include the datings by England et al. (2006) from where the Inuitian Ice Sheet used to be. Constraining our model to this dataset seems like an obvious next step although, as mentioned in the manuscript in chapter 5, our modeled evolution of the Greenland Ice Sheet constrained to the ice-core-derived elevation histories was not consistent with the timing of the retreat.

If multiple constraints *are* consistent, how should we compare their likelihoods? Ideally, stated uncertainties would accurately reflect true observational uncertainties. However, as with ice-core-derived elevations, they are often derived from true observations of proxy signals. Therefore, the declared observational error is contingent on the assumptions underlying the model used to derive these constraints. Notably, the elevation histories from Vinther et al. (2009) were revised by Lecavalier et al. (2013) using more accurate land uplift histories, although the assumptions for the revised estimates might be questioned again as the fractionation history is highly complex. As the different constraints used to inform *our* model might not be trusted it might prove informative to compare them on a more equal footing. We might be better of following the approach of Pollard et al. (2016, Sect. 2.4.1) were they compare squared misfits separately normalized for each observable. This would also allow us to use the present day elevation and velocities whose uncertainties are smaller than what we can hope to model.

Initially, we also considered constraining our model to measurements of annual deposition of sand grains obtained from marine sediment cores as this might be a very good proxy for the local ice discharge (Andresen et al., 2012). However, we found that the individual outlet glaciers in our model showed asynchronous behavior similar to what was found by Larsen et al. (2016) and found it unlikely that we could capture the exact timing of the surging events. We also explored using borehole temperature measurements to constrain horizontal advection. However, we found that the upper borehole temperatures were colder than the 1960-1990 mean surface temperatures reported by RACMO (Noël et al., 2019), and the slope of lower borehole temperatures did not match the heat flux data from Shapiro (2004). Despite these challenges, the vision remains to use multiple constraints to construct a coherent history of the Greenland Ice Sheet evolution through the Holocene period.

## 6.4 Paleoclimatic forcing of an ice sheet model

In our model, we applied past temperature anomalies uniformly across the spatial domain, aligning with Vinther et al. (2009)'s assumption that spatial differences in temperature anomalies result from elevation feedback. Although only the temperature reconstruction by Vinther et al. (2009) accounted for elevation changes, we incorporated all five temperature reconstructions from Nielsen et al. (2018) to explore the potential heterogeneous temperature anomalies. Our findings indicated that the temperature anomalies that best matched the elevation histories varied across the four ice core sites, possibly reflecting the heterogeneity of the actual temperature anomalies.

Despite our approach, there are existing reconstructions that acknowledge heterogeneous temperature anomalies. For instance, Badgeley et al. (2020) developed a surface temperature assimilation product based on multiple ice core isotopes and spatial relationships from transient climate model simulations (TraCE-21ka; Liu et al., 2009). These simulations utilize the ICE-5G isostatic topography reconstruction of the Greenland Ice Sheet by (Peltier, 2004). Although this climate model lacks an ice shelf component, incorporating these temperatures into our model could provide valuable insights into how our simulations might change under different temperature forcing scenarios.

## 6.5 Qualitative features of the ice sheet

Having quantitatively calibrated our model to the elevation changes, it is worthwhile to look at the time slices of Figure 5.6 and examine some of the qualitative features of our modeled Holocene Greenland Ice Sheet.

As discussed in chapter 5 we see a reconfiguration of flow patterns and the movement of the ice divide as the ice sheet retreated during the Holocene. Although our model does not resolve the well-defined localized flow of the Northeast Greenland Ice Stream (NEGIS), it does illustrate a southward migration of the flow pattern from the Last Glacial Maximum (LGM) to the present day as the ice sheet retreats from the continental shelf. This flow pattern migration is consistent with the hypothesized paleo ice stream identified by Franke et al. (2022) through airborne radar observations, located north of the current NEGIS whose onset might have been as recent as two millennia ago (Jansen et al., 2024). A recent study by Tabone et al. (2024) also modeled the evolution of the Greenland Ice Sheet throughout the Holocene. Their model *does* capture the localized flow pattern of NEGIS at present, although this is achieved only by locally tuning the basal friction, which complicates the interpretation of what drives the onset of NEGIS. Properly resolving both the present-day and paleo-NEGIS might require an anisotropic ice flow model (Gerber et al., 2023).

Another qualitative feature of our modeled ice sheet is the extensive ice shelf covering the Baffin Bay at the LGM. This ice shelf is similar to the one proposed by Couette et al. (2022) based on bathymetric data from Baffin Island at the western part of the ice shelf. Recently Batchelor et al. (2024) presented new bathymetric data from the Melville Bay at the eastern margin of the alleged ice shelf. Their study suggested that the ice sheet grounding line extended all the way to the continental shelf in agreement with the maximum LGM extent from Leger et al. (2024) and our model simulations. They find that the ice shelf scoured the ocean floor at depths down to at least 1220 meters below present-day sea level. This is also consistent with our modeled ice sheets where the ice thickness is around 900-1200 meters in that area during the LGM.

Jakobsson et al. (2016) presented similar bathymetric evidence suggesting that the entire Arctic Ocean north of Greenland was covered by an ice shelf. This evidence is supported by isotopic measurements from ocean sediments, which suggest that the Arctic Ocean might have been filled with freshwater during the last ice age. This indicates that ice shelves could have isolated the area from the saline seawater of the North Atlantic Ocean (Hoffmann, 2021). To accurately model such an extensive ice shelf, we would need to substantially extend our domain. Gasson et al. (2018) actually did this and were able to model an ice shelf extending across the Arctic Ocean, providing buttressing that elevated the surrounding ice sheets. However, they did not model the ice shelf in Baffin Bay. Thus, simulating both the Baffin Bay and Arctic Ocean ice shelves seems to be the next goal.

## 6.6 From past to present: Importance of initialization

To make accurate estimates of future mass losses, it is important that the ice sheet model is on the correct state trajectory. Despite achieving accurate surface velocities and thicknesses, the model may still possess incorrect internal energy and momentum states, leading to a calibration that is far from equilibrium and a transient calibration can thus reduce drift in future projections, addressing discrepancies caused by reliance only on present-day observables (Aschwanden et al., 2013).

In chapter 5 we explored the effects of calibrating the ice sheet throughout the Holocene period. We found that this calibration decreased the uncertainty in the state trajectories, thus refining the estimates of mass loss over the last 500 years from a prior of $12 \pm 40$ mm $\text{ka}^{-1}$ to a posterior of $23 \pm 26$ mm $\text{ka}^{-1}$. However, the present-day states still misrepresent the observed velocities and thicknesses. Improving these mismatches, while capturing the transient changes, would likely result in a present-day state that is highly reliable for modeling future mass losses. Nevertheless, achieving this would probably require a model resolution finer than 10 km to adequately capture the flow in narrow outlet glaciers (Aschwanden et al., 2016).

# Chapter 7

# Conclusion

This thesis used the Parallel Ice Sheet Model (PISM) to investigate the Greenland ice sheet's response to past and present climate conditions.

In our first study, a large ensemble of model simulations was run to assess the Greenland Ice Sheet's response to inter-annual temperature variability. These simulations were forced by different realizations of a first-order auto-regressive model derived from the statistics of the NOAA-CIRES 20th Century Reanalysis product. Our findings revealed that including inter-annual temperature variability led to a reduction in the steady-state ice sheet volume by 1.9±0.4 cm SLE, compared to a simulation without inter-annual temperature variability. This reduction was more pronounced by 11.5±1.4 cm SLE when the standard deviation of the temperature variability was doubled. This sensitivity varied spatially, with the northern basin accounting for 40% Additionally, we found that temperature variability significantly affects future projections under scenarios of abrupt temperature increases. In the control scenarios where the temperature forcing was abruptly changed by different increments, the rate of ice mass loss was 0.15 mm SLE $a^{-1}$ $K^{-1}$. This rate increased by 0.014–0.17 mm SLE $a^{-1}$ $K^{-1}$ when including the temperature variability. This underscores the critical importance of accounting for temperature variability in projections of future mass loss from the Greenland Ice Sheet.

In the second study, we conducted a Bayesian calibration of a positive degree day (PDD) model against the modeled surface mass balance from RACMO based on the average seasonal climatology for Greenland from 1960 to 1989. We accounted for constant and uniform refreezing and intra-monthly temperature variability and integrated the surface mass balance across the Greenland Ice Sheet. Through this approach, we calibrated the PDD parameters for snow and ice to be respectively $f_\mathrm{s} = 7.35 \pm 1.61$ mm $\mathrm{K}^{-1}$ $\mathrm{d}^{-1}$ and $f_\mathrm{i} = 10.21 \pm 2.65$ mm $\mathrm{K}^{-1}$ $\mathrm{d}^{-1}$. This calibrated probability density function is useful as a prior belief when doing long paleoclimatic simulations where the mass balance changes with the ice sheet's topography.

In the third and final study, we modeled the evolution of the Greenland Ice Sheet through the Holocene period. Again, we considered an ensemble of ice sheet simulations by systematically varying 20 key model parameters using the Latin Hypercube Sampling technique. We used this ensemble to calibrate the evolution to ice-core-derived surface elevation histories for four different ice-core sites. We found that the inclusion of the Canadian Arctic Archipelago in the modeling domain significantly affected the surface elevation history at the northern ice core sites as the Greenland Ice Sheet was buttressed against the Inuitian Ice Sheet and a large ice shelf covering the Baffin Bay during the LGM in our simulations.

We found that the modeled ice bridge connecting the Greenland Ice Sheet to the Innuitian Ice Sheet through the Nares Strait collapsed 4.9±0.5 ka before the present. At the LGM, the modeled Greenland Ice Sheet had an extent that was 49% larger than the present-day modeled extent, and through its Holocene deglaciation, it contributed 5.3±0.3 m SLE to the global mean sea level. Furthermore, we found that the Greenland Ice Sheet is still responding to its past history and that the last 500 years of mass loss primarily depend on the timing of the onset of oceanic forcing when excluding simulations forced by extreme temperature anomalies. The Bayesian calibration updates the last 500 years of mass loss from a prior estimate of 12±40 mm $\mathrm{ka}^{-1}$ to a posterior estimate of 23±26 mm $\mathrm{ka}^{-1}$, which is about 5% of the 1992-2020 estimated mass loss rate (The IMBIE Team, 2020). This inference stresses the importance of including the Greenland Ice Sheet's long-term response to past climatic changes when making projections of future mass loss.

# Bibliography

Aðalgeirsdóttir, G., A. Aschwanden, C. Khroulev, F. Boberg, R. Mottram, P. Lucas-Picher, and J.H. Christensen (2014). "Role of Model Initialization for Projections of 21st-Century Greenland Ice Sheet Mass Loss". In: *Journal of Glaciology* 60.222, pp. 782–794. DOI: `10.3189/2014JoG13J202` (cit. on p. 43).

Albrecht, Torsten, Ricarda Winkelmann, and Anders Levermann (2020a). "Glacial-Cycle Simulations of the Antarctic Ice Sheet with the Parallel Ice Sheet Model (PISM) – Part 1: Boundary Conditions and Climatic Forcing". In: *The Cryosphere* 14.2, pp. 599–632. DOI: `10.5194/tc-14-599-2020` (cit. on p. 21).

– (2020b). "Glacial-Cycle Simulations of the Antarctic Ice Sheet with the Parallel Ice Sheet Model (PISM) – Part 2: Parameter Ensemble Analysis". In: *The Cryosphere* 14.2, pp. 633–656. DOI: `10.5194/tc-14-633-2020` (cit. on p. 59).

Andersen, K. K., N. Azuma, J.-M. Barnola, M. Bigler, P. Biscaye, N. Caillon, J. Chappellaz, H. B. Clausen, D. Dahl-Jensen, H. Fischer, J. Flückiger, D. Fritzsche, Y. Fujii, K. Goto-Azuma, K. Grønvold, N. S. Gundestrup, M. Hansson, C. Huber, C. S. Hvidberg, S. J. Johnsen, U. Jonsell, J. Jouzel, S. Kipfstuhl, A. Landais, M. Leuenberger, R. Lorrain, V. Masson-Delmotte, H. Miller, H. Motoyama, H. Narita, T. Popp, S. O. Rasmussen, D. Raynaud, R. Rothlisberger, U. Ruth, D. Samyn, J. Schwander, H. Shoji, M.-L. Siggard-Andersen, J. P. Steffensen, T. Stocker, A. E. Sveinbjörnsdóttir, A. Svensson, M. Takata, J.-L. Tison, Th. Thorsteinsson, O. Watanabe, F. Wilhelms, J. W. C. White, and North Greenland Ice Core Project members (2004). "High-Resolution Record of Northern Hemisphere Climate Extending into the Last Interglacial Period". In: *Nature* 431.7005, pp. 147–151. DOI: `10.1038/nature02805` (cit. on pp. 1, 43).

Andresen, Camilla S., Fiammetta Straneo, Mads Hvid Ribergaard, Anders A. Bjørk, Thorbjørn J. Andersen, Antoon Kuijpers, Niels Nørgaard-Pedersen, Kurt H. Kjær, Frands Schjøth, Kaarina Weckström, and Andreas P. Ahlstrøm (2012). "Rapid Response of Helheim Glacier in Greenland to Climate Variability over the Past Century". In: *Nature Geoscience* 5.1, pp. 37–41. DOI: `10.1038/ngeo1349` (cit. on p. 74).

Appenzeller, C., T. F. Stocker, and M. Anklin (1998). "North Atlantic Oscillation Dynamics Recorded in Greenland Ice Cores". In: *Science* 282.5388, pp. 446–449. DOI: `10.1126/science.282.5388.446` (cit. on p. 2).

Aschwanden, A., G. Aðalgeirsdóttir, and C. Khroulev (2013). “Hindcasting to Measure Ice Sheet Model Sensitivity to Initial States”. In: *The Cryosphere* 7.4, pp. 1083–1093. DOI: `10.5194/tc-7-1083-2013` (cit. on p. 75).

Aschwanden, A. and D. J. Brinkerhoff (2022). “Calibrated Mass Loss Predictions for the Greenland Ice Sheet”. In: *Geophysical Research Letters* 49.19, e2022GL099058. DOI: `10.1029/2022GL099058` (cit. on pp. 3, 43, 51, 72).

Aschwanden, Andy, Timothy C. Bartholomaus, Douglas J. Brinkerhoff, and Martin Truffer (2021). “Brief Communication: A Roadmap towards Credible Projections of Ice Sheet Contribution to Sea Level”. In: *The Cryosphere* 15.12, pp. 5705–5715. DOI: `10.5194/tc-15-5705-2021` (cit. on pp. 2, 21, 43).

Aschwanden, Andy, Ed Bueler, Constantine Khroulev, and Heinz Blatter (2012). “An Enthalpy Formulation for Glaciers and Ice Sheets”. In: *Journal of Glaciology* 58.209, pp. 441–457. DOI: `10.3189/2012JoG11J088` (cit. on pp. 15, 22).

Aschwanden, Andy, Mark A. Fahnestock, and Martin Truffer (2016). “Complex Greenland Outlet Glacier Flow Captured”. In: *Nature Communications* 7.1, p. 10524. DOI: `10.1038/ncomms10524` (cit. on pp. 22, 61, 76).

Aschwanden, Andy, Mark A. Fahnestock, Martin Truffer, Douglas J. Brinkerhoff, Regine Hock, Constantine Khroulev, Ruth Mottram, and S. Abbas Khan (2019). “Contribution of the Greenland Ice Sheet to Sea Level over the next Millennium”. In: *Science Advances* 5.6, eaav9396. DOI: `10.1126/sciadv.aav9396` (cit. on pp. 13, 18, 48).

Axford, Yarrow, Anne De Vernal, and Erich C. Osterberg (2021). “Past Warmth and Its Impacts During the Holocene Thermal Maximum in Greenland”. In: *Annual Review of Earth and Planetary Sciences* 49.1, pp. 279–307. DOI: `10.1146/annurev-earth-081420-063858` (cit. on p. 62).

Badgeley, Jessica A., Eric J. Steig, Gregory J. Hakim, and Tyler J. Fudge (2020). “Greenland Temperature and Precipitation over the Last 20 000 Years Using Data Assimilation”. In: *Climate of the Past* 16.4, pp. 1325–1346. DOI: `10.5194/cp-16-1325-2020` (cit. on p. 74).

Bagherbandi, Mohammad, Hadi Amin, Linsong Wang, and Masoud Shirazian (2022). “Mantle Viscosity Derived From Geoid and Different Land Uplift Data in Greenland”. In: *Journal of Geophysical Research: Solid Earth* 127.8, e2021JB023351. DOI: `10.1029/2021JB023351` (cit. on p. 59).

Bamber, J. L., J. A. Griggs, R. T. W. L. Hurkmans, J. A. Dowdeswell, S. P. Gogineni, I. Howat, J. Mouginot, J. Paden, S. Palmer, E. Rignot, and D. Steinhage (2013). “A New Bed Elevation Dataset for Greenland”. In: *The Cryosphere* 7.2, pp. 499–510. DOI: `10.5194/tc-7-499-2013` (cit. on p. 22).

Batchelor, Christine L., Diana W. Krawczyk, Elaina O’Brien, and Joyce Mulder (2024). “Shelf-Break Glaciation and an Extensive Ice Shelf beyond Northwest Greenland at the Last Glacial Maximum”. In: *Marine Geology* 476, p. 107375. DOI: `10.1016/j.margeo.2024.107375` (cit. on p. 75).

Beckmann, Johanna and Ricarda Winkelmann (2023). “Effects of Extreme Melt Events on Ice Flow and Sea Level Rise of the Greenland Ice Sheet”. In: *The Cryosphere* 17.7, pp. 3083–3099. DOI: `10.5194/tc-17-3083-2023` (cit. on pp. 2, 21).

Bindschadler, Robert A., Sophie Nowicki, Ayako Abe-Ouchi, Andy Aschwanden, Hyeungu Choi, Jim Fastook, Glen Granzow, Ralf Greve, Gail Gutowski, Ute Herzfeld, Charles Jackson, Jesse Johnson, Constantine Khroulev, Anders Levermann, William H. Lipscomb, Maria A. Martin, Mathieu Morlighem, Byron R. Parizek, David Pollard, Stephen F. Price, Diandong Ren, Fuyuki Saito, Tatsuru Sato, Hakime Seddik, Helene Seroussi, Kunio Takahashi, Ryan Walker, and Wei Li Wang (2013). "Ice-Sheet Model Sensitivities to Environmental Forcing and Their Use in Projecting Future Sea Level (the SeaRISE Project)". In: *Journal of Glaciology* 59.214, pp. 195–224. DOI: `10.3189/2013JoG12J125` (cit. on p. 44).

Bjørk, A. A., S. Aagaard, A. Lütt, S. A. Khan, J. E. Box, K. K. Kjeldsen, N. K. Larsen, N. J. Korsgaard, J. Cappelen, W. T. Colgan, H. Machguth, C. S. Andresen, Y. Peings, and K. H. Kjær (2018). "Changes in Greenland's Peripheral Glaciers Linked to the North Atlantic Oscillation". In: *Nature Climate Change* 8.1, pp. 48–52. DOI: `10.1038/s41558-017-0029-1` (cit. on p. 2).

Blatter, Heinz (1995). "Velocity and Stress Fields in Grounded Glaciers: A Simple Algorithm for Including Deviatoric Stress Gradients". In: *Journal of Glaciology* 41.138, pp. 333–344. DOI: `10.3189/S002214300001621X` (cit. on p. 10).

Braithwaite, R. J. (1985). "Calculation of Degree-Days for Glacier-Climate Research". In: *Zeitschrift für Gletscherkunde und Glazialgeologie* 20/1984, pp. 1–8 (cit. on p. 47).

Braithwaite, R. J. and O. B. Olesen (1989). "Calculation of Glacier Ablation from Air Temperature, West Greenland". In: *Glacier Fluctuations and Climatic Change*. Kluwer Academic Publishers, pp. 219–233 (cit. on pp. 12, 36).

Briner, Jason P., Joshua K. Cuzzone, Jessica A. Badgeley, Nicolás E. Young, Eric J. Steig, Mathieu Morlighem, Nicole-Jeanne Schlegel, Gregory J. Hakim, Joerg M. Schaefer, Jesse V. Johnson, Alia J. Lesnek, Elizabeth K. Thomas, Estelle Allan, Ole Bennike, Allison A. Cluett, Beata Csatho, Anne De Vernal, Jacob Downs, Eric Larour, and Sophie Nowicki (2020). "Rate of Mass Loss from the Greenland Ice Sheet Will Exceed Holocene Values This Century". In: *Nature* 586.7827, pp. 70–74. DOI: `10.1038/s41586-020-2742-6` (cit. on pp. 63, 73).

Bueler, E. and W. van Pelt (2015). "Mass-Conserving Subglacial Hydrology in the Parallel Ice Sheet Model Version 0.6". In: *Geoscientific Model Development* 8.6, pp. 1613–1635. DOI: `10.5194/gmd-8-1613-2015` (cit. on pp. 9, 49).

Bueler, Ed and Jed Brown (2009). "Shallow Shelf Approximation as a "Sliding Law" in a Thermomechanically Coupled Ice Sheet Model". In: *Journal of Geophysical Research* 114.F3, F03008. DOI: `10.1029/2008JF001179` (cit. on pp. 11, 14, 22, 37, 46, 64).

Bueler, Ed, Craig S. Lingle, and Jed Brown (2007). "Fast Computation of a Viscoelastic Deformable Earth Model for Ice-Sheet Simulations". In: *Annals of Glaciology* 46, pp. 97–105. DOI: `10.3189/172756407782871567` (cit. on pp. 15, 49).

Clark, Peter U., Feng He, Nicholas R. Golledge, Jerry X. Mitrovica, Andrea Dutton, Jeremy S. Hoffman, and Sarah Dendy (2020). "Oceanic Forcing of Penultimate Deglacial and Last Interglacial Sea-Level Rise". In: *Nature* 577.7792, pp. 660–664. DOI: `10.1038/s41586-020-1931-7` (cit. on pp. 48, 72).

Colgan, William, Kenneth D. Mankoff, Kristian K. Kjeldsen, Anders A. Bjørk, Jason E. Box, Sebastian B. Simonsen, Louise S. Sørensen, S. Abbas Khan, Anne M. Solgaard, Rene Forsberg, Henriette Skourup, Lars Stenseng, Steen S. Kristensen, Sine M. Hvidegaard, Michele Citterio, Nanna Karlsson, Xavier Fettweis, Andreas P. Ahlstrøm, Signe B. Andersen, Dirk van As, and Robert S. Fausto (2019). “Greenland Ice Sheet Mass Balance Assessed by PROMICE (1995–2015)”. In: *GEUS Bulletin* 43. DOI: 10.34194/GEUSB-201943-02-01 (cit. on p. 37).

Compo, G. P., J. S. Whitaker, P. D. Sardeshmukh, N. Matsui, R. J. Allan, X. Yin, B. E. Gleason, R. S. Vose, G. Rutledge, P. Bessemoulin, S. Brönnimann, M. Brunet, R. I. Crouthamel, A. N. Grant, P. Y. Groisman, P. D. Jones, M. C. Kruk, A. C. Kruger, G. J. Marshall, M. Maugeri, H. Y. Mok, Ø. Nordli, T. F. Ross, R. M. Trigo, X. L. Wang, S. D. Woodruff, and S. J. Worley (2011). “The Twentieth Century Reanalysis Project: The Twentieth Century Reanalysis Project”. In: *Quarterly Journal of the Royal Meteorological Society* 137.654, pp. 1–28. DOI: 10.1002/qj.776 (cit. on pp. 21, 23, 24).

Conway, H., B. L. Hall, G. H. Denton, A. M. Gades, and E. D. Waddington (1999). “Past and Future Grounding-Line Retreat of the West Antarctic Ice Sheet”. In: *Science* 286.5438, pp. 280–283. DOI: 10.1126/science.286.5438.280 (cit. on p. 10).

Copernicus (2024). *June 2024 Marks 12th Month of Global Temperatures at 1.5°C above Pre-Industrial Levels*. URL: https://climate.copernicus.eu/june-2024-marks-12th-month-global-temperatures-15degc-above-pre-industrial-levels (visited on 09/12/2024) (cit. on p. 2).

Couette, Pierre-Olivier, Patrick Lajeunesse, Jean-François Ghienne, Boris Dorschel, Catalina Gebhardt, Dierk Hebbeln, and Etienne Brouard (2022). “Evidence for an Extensive Ice Shelf in Northern Baffin Bay during the Last Glacial Maximum”. In: *Communications Earth & Environment* 3.1, p. 225. DOI: 10.1038/s43247-022-00559-7 (cit. on pp. 55, 75).

Cuffey, Kurt and W. S. B. Paterson (2010). *The Physics of Glaciers*. 4th ed. Burlington, MA: Butterworth-Heinemann/Elsevier. 693 pp. (cit. on pp. 5, 7, 8, 11).

Dansgaard, W., S. J. Johnsen, J. Møller, and C. C. Langway (1969). “One Thousand Centuries of Climatic Record from Camp Century on the Greenland Ice Sheet”. In: *Science* 166.3903, pp. 377–381. DOI: 10.1126/science.166.3903.377 (cit. on p. 44).

Ditlevsen, Peter and Susanne Ditlevsen (2023). “Warning of a Forthcoming Collapse of the Atlantic Meridional Overturning Circulation”. In: *Nature Communications* 14.1, p. 4254. DOI: 10.1038/s41467-023-39810-w (cit. on p. 2).

Edwards, Tamsin L., Mark A. Brandon, Gael Durand, Neil R. Edwards, Nicholas R. Golledge, Philip B. Holden, Isabel J. Nias, Antony J. Payne, Catherine Ritz, and Andreas Wernecke (2019). “Revisiting Antarctic Ice Loss Due to Marine Ice-Cliff Instability”. In: *Nature* 566.7742, pp. 58–64. DOI: 10.1038/s41586-019-0901-4 (cit. on pp. 2, 18).

England, J., N. Atkinson, J. Bednarski, A.S. Dyke, D.A. Hodgson, and C. Ó Cofaigh (2006). “The Innuitian Ice Sheet: Configuration, Dynamics and Chronology”. In: *Quaternary Science Reviews* 25.7-8, pp. 689–703. DOI: 10.1016/j.quascirev.2005.08.007 (cit. on pp. 43, 55, 59, 61, 64, 73).

Eyring, V., N.P. Gillett, K.M. Achuta Rao, R. Barimalala, M. Barreiro Parrillo, N. Bellouin, C. Cassou, P.J. Durack, Y. Kosaka, S. McGregor, S. Min, O. Morgenstern, and Y. Sun (2021). “Human Influence on the Climate System”. In: *Climate Change 2021: The Physical Science Basis. Contribution of Working Group I to the Sixth Assessment Report of the Intergovernmental*

*Panel on Climate Change*. Ed. by V. Masson-Delmotte, P. Zhai, A. Pirani, S.L. Connors, C. Péan, S. Berger, N. Caud, Y. Chen, L. Goldfarb, M.I. Gomis, M. Huang, K. Leitzell, E. Lonnoy, J.B.R. Matthews, T.K. Maycock, T. Waterfield, O. Yelekçi, R. Yu, and B. Zhou. Cambridge, United Kingdom and New York, NY, USA: Cambridge University Press, pp. 423–552. DOI: `10.1017/9781009157896.005` (cit. on pp. 2, 43).

Fettweis, Xavier, Stefan Hofer, Uta Krebs-Kanzow, Charles Amory, Teruo Aoki, Constantijn J. Berends, Andreas Born, Jason E. Box, Alison Delhasse, Koji Fujita, Paul Gierz, Heiko Goelzer, Edward Hanna, Akihiro Hashimoto, Philippe Huybrechts, Marie-Luise Kapsch, Michalea D. King, Christoph Kittel, Charlotte Lang, Peter L. Langen, Jan T. M. Lenaerts, Glen E. Liston, Gerrit Lohmann, Sebastian H. Mernild, Uwe Mikolajewicz, Kameswarrao Modali, Ruth H. Mottram, Masashi Niwano, Brice Noël, Jonathan C. Ryan, Amy Smith, Jan Streffing, Marco Tedesco, Willem Jan Van De Berg, Michiel Van Den Broeke, Roderik S. W. Van De Wal, Leo Van Kampenhout, David Wilton, Bert Wouters, Florian Ziemen, and Tobias Zolles (2020). “GrSMBMIP: Intercomparison of the Modelled 1980–2012 Surface Mass Balance over the Greenland Ice Sheet”. In: *The Cryosphere* 14.11, pp. 3935–3958. DOI: `10.5194/tc-14-3935-2020` (cit. on pp. 36, 37).

Fichtner, Andreas (2021). *Lecture Notes on Inverse Theory*. DOI: `10.33774/coe-2021-qpq2j`. URL: `https://www.cambridge.org/engage/coe/article-details/60e6a70d609d0d7fa3d893a7` (visited on 09/06/2024). Pre-published (cit. on p. 15).

Fichtner, Andreas, Coen Hofstede, Brian L. N. Kennett, Niels F. Nymand, Mikkel L. Lauritzen, Dimitri Zigone, and Olaf Eisen (2023). “Fiber-Optic Airplane Seismology on the Northeast Greenland Ice Stream”. In: *The Seismic Record* 3.2, pp. 125–133. DOI: `10.1785/0320230004` (cit. on p. viii).

Flanders Marine Institute (VLIZ), Belgium (2023). *Maritime Boundaries Geodatabase: Maritime Boundaries and Exclusive Economic Zones (200NM), Version 12*. DOI: `10.14284/632` (cit. on pp. 45, 46).

Foreman-Mackey, Daniel, David W. Hogg, Dustin Lang, and Jonathan Goodman (2013). “Emcee: The MCMC Hammer”. In: *Publications of the Astronomical Society of the Pacific* 125.925, p. 306. DOI: `10.1086/670067` (cit. on p. 38).

Fox-Kemper, B., H.T. Hewitt, C. Xiao, G. Aðalgeirsdóttir, S.S. Drijfhout, T.L. Edwards, N.R. Golledge, M. Hemer, R.E. Kopp, G. Krinner, A. Mix, D. Notz, S. Nowicki, I.S. Nurhati, L. Ruiz, J.-B. Sallée, A.B.A. Slangen, and Y. Yu (2021). “Ocean, Cryosphere and Sea Level Change”. In: *Climate Change 2021: The Physical Science Basis. Contribution of Working Group I to the Sixth Assessment Report of the Intergovernmental Panel on Climate Change*. Ed. by V. Masson-Delmotte, P. Zhai, A. Pirani, S.L. Connors, C. Péan, S. Berger, N. Caud, Y. Chen, L. Goldfarb, M.I. Gomis, M. Huang, K. Leitzell, E. Lonnoy, J.B.R. Matthews, T.K. Maycock, T. Waterfield, O. Yelekçi, R. Yu, and B. Zhou. Cambridge, United Kingdom and New York, NY, USA: Cambridge University Press, pp. 1211–1362. DOI: `10.1017/9781009157896.011` (cit. on pp. 1, 20).

Franke, Steven, Paul D. Bons, Julien Westhoff, Ilka Weikusat, Tobias Binder, Kyra Streng, Daniel Steinhage, Veit Helm, Olaf Eisen, John D. Paden, Graeme Eagles, and Daniela Jansen (2022).

"Holocene Ice-Stream Shutdown and Drainage Basin Reconfiguration in Northeast Greenland". In: *Nature Geoscience* 15.12, pp. 995–1001. DOI: 10.1038/s41561-022-01082-2 (cit. on p. 75).

Frankignoul, Claude and Klaus Hasselmann (1977). "Stochastic Climate Models, Part II Application to Sea-Surface Temperature Anomalies and Thermocline Variability". In: *Tellus* 29.4, pp. 289–305. DOI: 10.1111/j.2153-3490.1977.tb00740.x (cit. on p. 24).

Frederikse, Thomas, Felix Landerer, Lambert Caron, Surendra Adhikari, David Parkes, Vincent W. Humphrey, Sönke Dangendorf, Peter Hogarth, Laure Zanna, Lijing Cheng, and Yun-Hao Wu (2020). "The Causes of Sea-Level Rise since 1900". In: *Nature* 584.7821, pp. 393–397. DOI: 10.1038/s41586-020-2591-3 (cit. on p. 20).

Gasson, Edward G. W., Robert M. DeConto, David Pollard, and Chris D. Clark (2018). "Numerical Simulations of a Kilometre-Thick Arctic Ice Shelf Consistent with Ice Grounding Observations". In: *Nature Communications* 9.1, p. 1510. DOI: 10.1038/s41467-018-03707-w (cit. on p. 75).

GEBCO Bathymetric Compilation Group (2023). *The GEBCO_2023 Grid - a Continuous Terrain Model of the Global Oceans and Land.* Version 1. NERC EDS British Oceanographic Data Centre NOC. DOI: 10.5285/F98B053B-0CBC-6C23-E053-6C86ABC0AF7B (cit. on pp. 45, 46, 49, 50).

Gerber, Tamara Annina, David A. Lilien, Nicholas Mossor Rathmann, Steven Franke, Tun Jan Young, Fernando Valero-Delgado, M. Reza Ershadi, Reinhard Drews, Ole Zeising, Angelika Humbert, Nicolas Stoll, Ilka Weikusat, Aslak Grinsted, Christine Schøtt Hvidberg, Daniela Jansen, Heinrich Miller, Veit Helm, Daniel Steinhage, Charles O'Neill, John Paden, Siva Prasad Gogineni, Dorthe Dahl-Jensen, and Olaf Eisen (2023). "Crystal Orientation Fabric Anisotropy Causes Directional Hardening of the Northeast Greenland Ice Stream". In: *Nature Communications* 14.1, p. 2653. DOI: 10.1038/s41467-023-38139-8 (cit. on p. 75).

Gervais, Melissa, Jeffrey Shaman, and Yochanan Kushnir (2019). "Impacts of the North Atlantic Warming Hole in Future Climate Projections: Mean Atmospheric Circulation and the North Atlantic Jet". In: DOI: 10.1175/JCLI-D-18-0647.1 (cit. on p. 2).

Gkinis, V., S.B. Simonsen, S.L. Buchardt, J.W.C. White, and B.M. Vinther (2014). "Water Isotope Diffusion Rates from the NorthGRIP Ice Core for the Last 16,000 Years – Glaciological and Paleoclimatic Implications". In: *Earth and Planetary Science Letters* 405, pp. 132–141. DOI: 10.1016/j.epsl.2014.08.022 (cit. on pp. 44, 59, 65).

Gladstone, R. M., A. J. Payne, and S. L. Cornford (2010). "Parameterising the Grounding Line in Flow-Line Ice Sheet Models". In: *The Cryosphere* 4.4, pp. 605–619. DOI: 10.5194/tc-4-605-2010 (cit. on pp. 15, 46).

Glen, J. W. (1952). "Experiments on the Deformation of Ice". In: *Journal of Glaciology* 2.12, pp. 111–114. DOI: 10.3189/S0022143000034067 (cit. on pp. 6, 7).

– (1955). "The Creep of Polycrystalline Ice". In: *Proceedings of the Royal Society of London Series A* 228, pp. 519–538. DOI: 10.1098/rspa.1955.0066 (cit. on pp. 7, 22).

Goelzer, Heiko, Sophie Nowicki, Anthony Payne, Eric Larour, Helene Seroussi, William H. Lipscomb, Jonathan Gregory, Ayako Abe-Ouchi, Andrew Shepherd, Erika Simon, Cécile Agosta, Patrick Alexander, Andy Aschwanden, Alice Barthel, Reinhard Calov, Christopher Chambers, Youngmin Choi, Joshua Cuzzone, Christophe Dumas, Tamsin Edwards, Denis Felikson, Xavier

Fettweis, Nicholas R. Golledge, Ralf Greve, Angelika Humbert, Philippe Huybrechts, Sebastien Le Clec'H, Victoria Lee, Gunter Leguy, Chris Little, Daniel P. Lowry, Mathieu Morlighem, Isabel Nias, Aurelien Quiquet, Martin Rückamp, Nicole-Jeanne Schlegel, Donald A. Slater, Robin S. Smith, Fiamma Straneo, Lev Tarasov, Roderik Van De Wal, and Michiel Van Den Broeke (2020). "The Future Sea-Level Contribution of the Greenland Ice Sheet: A Multi-Model Ensemble Study of ISMIP6". In: *The Cryosphere* 14.9, pp. 3071–3096. DOI: `10.5194/tc-14-3071-2020` (cit. on pp. 2, 21, 29, 71).

Goldsby, D. L. and D. L. Kohlstedt (2001). "Superplastic Deformation of Ice: Experimental Observations". In: *Journal of Geophysical Research: Solid Earth* 106.B6, pp. 11017–11030. DOI: `10.1029/2000JB900336` (cit. on p. 7).

Gulev, S.K., P.W. Thorne, J. Ahn, F.J. Dentener, C.M. Domingues, S. Gerland, D. Gong, D.S. Kaufman, H.C. Nnamchi, J. Quaas, J.A. Rivera, S. Sathyendranath, S.L. Smith, B. Trewin, K. von Schuckmann, and R.S. Vose (2021). "Changing State of the Climate System". In: *Climate Change 2021: The Physical Science Basis. Contribution of Working Group I to the Sixth Assessment Report of the Intergovernmental Panel on Climate Change*. Ed. by V. Masson-Delmotte, P. Zhai, A. Pirani, S.L. Connors, C. Péan, S. Berger, N. Caud, Y. Chen, L. Goldfarb, M.I. Gomis, M. Huang, K. Leitzell, E. Lonnoy, J.B.R. Matthews, T.K. Maycock, T. Waterfield, O. Yelekçi, R. Yu, and B. Zhou. Cambridge, United Kingdom and New York, NY, USA: Cambridge University Press, pp. 287–422. DOI: `10.1017/9781009157896.004` (cit. on pp. 2, 43).

Hasselmann, K. (1976). "Stochastic Climate Models Part I. Theory". In: *Tellus* 28.6, pp. 473–485. DOI: `10.1111/j.2153-3490.1976.tb00696.x` (cit. on p. 24).

Hastings, W. K. (1970). "Monte Carlo Sampling Methods Using Markov Chains and Their Applications". In: *Biometrika* 57.1, pp. 97–109. DOI: `10.1093/biomet/57.1.97` (cit. on p. 17).

Hill, Emily A., Sebastian H. R. Rosier, G. Hilmar Gudmundsson, and Matthew Collins (2021). "Quantifying the Potential Future Contribution to Global Mean Sea Level from the Filchner–Ronne Basin, Antarctica". In: *The Cryosphere* 15.10, pp. 4675–4702. DOI: `10.5194/tc-15-4675-2021` (cit. on p. 18).

Hock, Regine, Andrew Bliss, Ben Marzeion, Rianne H. Giesen, Yukiko Hirabayashi, Matthias Huss, Valentina Radić, and Aimée B. A. Slangen (2019). "GlacierMIP – A Model Intercomparison of Global-Scale Glacier Mass-Balance Models and Projections". In: *Journal of Glaciology* 65.251, pp. 453–467. DOI: `10.1017/jog.2019.22` (cit. on pp. 2, 71).

Hoffmann, Sharon (2021). "The Arctic Ocean Might Have Been Filled with Freshwater during Ice Ages". In: *Nature* 590.7844, pp. 37–38. DOI: `10.1038/d41586-021-00208-7` (cit. on p. 75).

Hugonnet, Romain, Robert McNabb, Etienne Berthier, Brian Menounos, Christopher Nuth, Luc Girod, Daniel Farinotti, Matthias Huss, Ines Dussaillant, Fanny Brun, and Andreas Kääb (2021). "Accelerated Global Glacier Mass Loss in the Early Twenty-First Century". In: *Nature* 592.7856, pp. 726–731. DOI: `10.1038/s41586-021-03436-z` (cit. on p. 2).

Huybrechts, Philippe (2002). "Sea-Level Changes at the LGM from Ice-Dynamic Reconstructions of the Greenland and Antarctic Ice Sheets during the Glacial Cycles". In: *Quaternary Science Reviews*. EPILOG 21.1, pp. 203–231. DOI: `10.1016/S0277-3791(01)00082-8` (cit. on pp. 44, 54, 65).

Imbrie, John D and Andrew McIntyre (2006). *SPECMAP Time Scale Developed by Imbrie et al., 1984 Based on Normalized Planktonic Records (Normalized O-18 vs Time, Specmap.017).* PANGAEA. DOI: `10.1594/PANGAEA.441706` (cit. on p. 48).

Jakobsson, Martin, Larry A. Mayer, Caroline Bringensparr, Carlos F. Castro, Rezwan Mohammad, Paul Johnson, Tomer Ketter, Daniela Accettella, David Amblas, Lu An, Jan Erik Arndt, Miquel Canals, José Luis Casamor, Nolwenn Chauché, Bernard Coakley, Seth Danielson, Maurizio Demarte, Mary-Lynn Dickson, Boris Dorschel, Julian A. Dowdeswell, Simon Dreutter, Alice C. Fremand, Dana Gallant, John K. Hall, Laura Hehemann, Hanne Hodnesdal, Jongkuk Hong, Roberta Ivaldi, Emily Kane, Ingo Klaucke, Diana W. Krawczyk, Yngve Kristoffersen, Boele R. Kuipers, Romain Millan, Giuseppe Masetti, Mathieu Morlighem, Riko Noormets, Megan M. Prescott, Michele Rebesco, Eric Rignot, Igor Semiletov, Alex J. Tate, Paola Travaglini, Isabella Velicogna, Pauline Weatherall, Wilhelm Weinrebe, Joshua K. Willis, Michael Wood, Yulia Zarayskaya, Tao Zhang, Mark Zimmermann, and Karl B. Zinglersen (2020). "The International Bathymetric Chart of the Arctic Ocean Version 4.0". In: *Scientific Data* 7.1, p. 176. DOI: `10.1038/s41597-020-0520-9` (cit. on pp. 45, 46, 49, 50).

Jakobsson, Martin, Johan Nilsson, Leif Anderson, Jan Backman, Göran Björk, Thomas M. Cronin, Nina Kirchner, Andrey Koshurnikov, Larry Mayer, Riko Noormets, Matthew O'Regan, Christian Stranne, Roman Ananiev, Natalia Barrientos Macho, Denis Cherniykh, Helen Coxall, Björn Eriksson, Tom Flodén, Laura Gemery, Örjan Gustafsson, Kevin Jerram, Carina Johansson, Alexey Khortov, Rezwan Mohammad, and Igor Semiletov (2016). "Evidence for an Ice Shelf Covering the Central Arctic Ocean during the Penultimate Glaciation". In: *Nature Communications* 7.1, p. 10365. DOI: `10.1038/ncomms10365` (cit. on p. 75).

Jansen, Daniela, Steven Franke, Catherine C. Bauer, Tobias Binder, Dorthe Dahl-Jensen, Jan Eichler, Olaf Eisen, Yuanbang Hu, Johanna Kerch, Maria-Gema Llorens, Heinrich Miller, Niklas Neckel, John Paden, Tamara de Riese, Till Sachau, Nicolas Stoll, Ilka Weikusat, Frank Wilhelms, Yu Zhang, and Paul D. Bons (2024). "Shear Margins in Upper Half of Northeast Greenland Ice Stream Were Established Two Millennia Ago". In: *Nature Communications* 15.1, p. 1193. DOI: `10.1038/s41467-024-45021-8` (cit. on p. 75).

Johnsen, Sigfus J., Henrik B. Clausen, Willi Dansgaard, Niels S. Gundestrup, Margareta Hansson, Peter Jonsson, Jørgen P. Steffensen, and Arny E. Sveinbjørnsdottir (1992). "A "Deep" Ice Core from East Greenland". In: *Meddelelser om Grønland. Geoscience* 29, 22 pp.–22 pp. DOI: `10.7146/moggeosci.v29i.140329` (cit. on p. 60).

Johnsen, Sigfus J., Dorthe Dahl-Jensen, Willi Dansgaard, and Niels Gundestrup (1995). "Greenland Palaeotemperatures Derived from GRIP Bore Hole Temperature and Ice Core Isotope Profiles". In: *Tellus B: Chemical and Physical Meteorology* 47.5, pp. 624–629. DOI: `10.3402/tellusb.v47i5.16077` (cit. on pp. 3, 44, 65).

Joughin, Ian, David E. Shean, Benjamin E. Smith, and Dana Floricioiu (2020). "A Decade of Variability on Jakobshavn Isbræ: Ocean Temperatures Pace Speed through Influence on Mélange Rigidity". In: *The Cryosphere* 14.1, pp. 211–227. DOI: `10.5194/tc-14-211-2020` (cit. on p. 1).

Kuiper, Ernst-Jan N., Johannes H. P. De Bresser, Martyn R. Drury, Jan Eichler, Gill M. Pennock, and Ilka Weikusat (2020). "Using a Composite Flow Law to Model Deformation in the NEEM

Deep Ice Core, Greenland – Part 2: The Role of Grain Size and Premelting on Ice Deformation at High Homologous Temperature". In: *The Cryosphere* 14.7, pp. 2449–2467. DOI: `10.5194/tc-14-2449-2020` (cit. on p. 7).

Larour, E., M. Morlighem, H. Seroussi, J. Schiermeier, and E. Rignot (2012). "Ice Flow Sensitivity to Geothermal Heat Flux of Pine Island Glacier, Antarctica". In: *Journal of Geophysical Research: Earth Surface* 117.F4. DOI: `10.1029/2012JF002371` (cit. on p. 18).

Larsen, Signe Hillerup, Shfaqat Abbas Khan, Andreas Peter Ahlstrøm, Christine Schøtt Hvidberg, Michael John Willis, and Signe Bech Andersen (2016). "Increased Mass Loss and Asynchronous Behavior of Marine-Terminating Outlet Glaciers at Upernavik Isstrøm, NW Greenland". In: *Journal of Geophysical Research: Earth Surface* 121.2, pp. 241–256. DOI: `10.1002/2015JF003507` (cit. on p. 74).

Lauritzen, Mikkel, Guðfinna Aðalgeirsdóttir, Nicholas Rathmann, Aslak Grinsted, Brice Noël, and Christine S. Hvidberg (2023). "The Influence of Inter-Annual Temperature Variability on the Greenland Ice Sheet Volume". In: *Annals of Glaciology*, pp. 1–8. DOI: `10.1017/aog.2023.53` (cit. on pp. viii, 2, 19, 43).

Lauritzen, Mikkel Langgaard, Anne Munck Solgaard, Nicholas Mossor Rathmann, Bo Møllesøe Vinther, Aslak Grindsted, Brice Noël, Guðfinna Aðalgeirsdóttir, and Christine Schøtt Hvidberg (2024). "Modeled Greenland Ice Sheet Evolution Constrained by Ice-Core-Derived Holocene Elevation Histories". In: *EGUsphere*, pp. 1–29. DOI: `10.5194/egusphere-2024-2223` (cit. on pp. viii, 3, 41).

Lecavalier, Benoit S., David A. Fisher, Glenn A. Milne, Bo M. Vinther, Lev Tarasov, Philippe Huybrechts, Denis Lacelle, Brittany Main, James Zheng, Jocelyne Bourgeois, and Arthur S. Dyke (2017). "High Arctic Holocene Temperature Record from the Agassiz Ice Cap and Greenland Ice Sheet Evolution". In: *Proceedings of the National Academy of Sciences* 114.23, pp. 5952–5957. DOI: `10.1073/pnas.1616287114` (cit. on pp. 44, 60, 62, 70, 73).

Lecavalier, Benoit S., Glenn A. Milne, Bo M. Vinther, David A. Fisher, Arthur S. Dyke, and Matthew J.R. Simpson (2013). "Revised Estimates of Greenland Ice Sheet Thinning Histories Based on Ice-Core Records". In: *Quaternary Science Reviews* 63, pp. 73–82. DOI: `10.1016/j.quascirev.2012.11.030` (cit. on pp. 44, 60, 73).

Leger, Tancrède P. M., Christopher D. Clark, Carla Huynh, Sharman Jones, Jeremy C. Ely, Sarah L. Bradley, Christiaan Diemont, and Anna L. C. Hughes (2024). "A Greenland-wide Empirical Reconstruction of Paleo Ice Sheet Retreat Informed by Ice Extent Markers: PaleoGrIS Version 1.0". In: *Climate of the Past* 20.3, pp. 701–755. DOI: `10.5194/cp-20-701-2024` (cit. on pp. 3, 54, 57, 64, 73, 75).

Lesnek, A. J., J. P. Briner, N. E. Young, and J. K. Cuzzone (2020). "Maximum Southwest Greenland Ice Sheet Recession in the Early Holocene". In: *Geophysical Research Letters* 47.1, e2019GL083164. DOI: `10.1029/2019GL083164` (cit. on p. 3).

Lewis, E. L. and R. G. Perkin (1986). "Ice Pumps and Their Rates". In: *Journal of Geophysical Research: Oceans* 91.C10, pp. 11756–11762. DOI: `10.1029/JC091iC10p11756` (cit. on p. 13).

Lingle, Craig S. and James A. Clark (1985). "A Numerical Model of Interactions between a Marine Ice Sheet and the Solid Earth: Application to a West Antarctic Ice Stream". In: *Journal of*

*Geophysical Research: Oceans* 90.C1, pp. 1100–1114. DOI: `10.1029/JC090iC01p01100` (cit. on pp. 15, 49, 59).

Lisiecki, Lorraine E. and Maureen E. Raymo (2005). "A Pliocene-Pleistocene Stack of 57 Globally Distributed Benthic $\delta$18O Records". In: *Paleoceanography* 20.1. DOI: `10.1029/2004PA001071` (cit. on p. 1).

Liu, Z., B. L. Otto-Bliesner, F. He, E. C. Brady, R. Tomas, P. U. Clark, A. E. Carlson, J. Lynch-Stieglitz, W. Curry, E. Brook, D. Erickson, R. Jacob, J. Kutzbach, and J. Cheng (2009). "Transient Simulation of Last Deglaciation with a New Mechanism for Bølling-Allerød Warming". In: *Science* 325.5938, pp. 310–314. DOI: `10.1126/science.1171041` (cit. on p. 74).

Lliboutry, L. and P. Duval (1985). "Various Isotropic and Anisotropic Ices Found in Glaciers and Polar Ice Caps and Their Corresponding Rheologies". In: *International Journal of Rock Mechanics and Mining Sciences & Geomechanics Abstracts* 22.6, p. 198. DOI: `10.1016/0148-9062(85)90267-0` (cit. on pp. 8, 22).

Lowrie, William and Andreas Fichtner (2020). *Fundamentals of Geophysics*. Third edition. Cambridge, United Kingdom ; New York: Cambridge University Press (cit. on p. 13).

MacAyeal, Douglas R. (1989). "Large-Scale Ice Flow over a Viscous Basal Sediment: Theory and Application to Ice Stream B, Antarctica". In: *Journal of Geophysical Research: Solid Earth* 94.B4, pp. 4071–4087. DOI: `10.1029/JB094iB04p04071` (cit. on p. 10).

Mankoff, Kenneth D., Brice Noël, Xavier Fettweis, Andreas P. Ahlstrøm, William Colgan, Ken Kondo, Kirsty Langley, Shin Sugiyama, Dirk van As, and Robert S. Fausto (2020). "Greenland Liquid Water Discharge from 1958 through 2019". In: *Earth System Science Data* 12.4, pp. 2811–2841. DOI: `10.5194/essd-12-2811-2020` (cit. on p. 37).

McKay, M. D., R. J. Beckman, and W. J. Conover (1979). "A Comparison of Three Methods for Selecting Values of Input Variables in the Analysis of Output from a Computer Code". In: *Technometrics* 21.2, pp. 239–245. DOI: `10.2307/1268522`. JSTOR: `1268522` (cit. on p. 17).

Metropolis, Nicholas, Arianna W. Rosenbluth, Marshall N. Rosenbluth, Augusta H. Teller, and Edward Teller (1953). "Equation of State Calculations by Fast Computing Machines". In: *The Journal of Chemical Physics* 21.6, pp. 1087–1092. DOI: `10.1063/1.1699114` (cit. on p. 17).

Mikkelsen, Troels Bøgeholm, Aslak Grinsted, and Peter Ditlevsen (2018). "Influence of Temperature Fluctuations on Equilibrium Ice Sheet Volume". In: *The Cryosphere* 12.1, pp. 39–47. DOI: `10.5194/tc-12-39-2018` (cit. on pp. 2, 21, 24, 27, 29, 32, 33, 71).

Milanković, Milutin (1941). *Kanon Der Erdbestrahlung Und Seine Anwendung Auf Des Eiszeitenproblem*. Royal Serbian Academy, Section of Mathematical and Natural Sciences, 33, Belgrade (cit. on p. 1).

Miller, Julie Z., Riley Culberg, David G. Long, Christopher A. Shuman, Dustin M. Schroeder, and Mary J. Brodzik (2022). "An Empirical Algorithm to Map Perennial Firn Aquifers and Ice Slabs within the Greenland Ice Sheet Using Satellite L-band Microwave Radiometry". In: *The Cryosphere* 16.1, pp. 103–125. DOI: `10.5194/tc-16-103-2022` (cit. on p. 11).

Morland, L. W. (1987). "Unconfined Ice-Shelf Flow". In: *Dynamics of the West Antarctic Ice Sheet*. Ed. by C. J. Van der Veen and J. Oerlemans. Dordrecht: Springer Netherlands, pp. 99–116. DOI: `10.1007/978-94-009-3745-1_6` (cit. on p. 10).

Morland, L. W. and I. R. Johnson (1980). “Steady Motion of Ice Sheets”. In: *Journal of Glaciology* 25.92, pp. 229–246. DOI: `10.3189/S0022143000010467` (cit. on p. 10).

Morlighem, M., J. Bondzio, H. Seroussi, E. Rignot, E. Larour, A. Humbert, and S. Rebuffi (2016). “Modeling of Store Gletscher’s Calving Dynamics, West Greenland, in Response to Ocean Thermal Forcing”. In: *Geophysical Research Letters* 43.6, pp. 2659–2666. DOI: `10.1002/2016GL067695` (cit. on pp. 13, 48).

Morlighem, M., C. N. Williams, E. Rignot, L. An, J. E. Arndt, J. L. Bamber, G. Catania, N. Chauché, J. A. Dowdeswell, B. Dorschel, I. Fenty, K. Hogan, I. Howat, A. Hubbard, M. Jakobsson, T. M. Jordan, K. K. Kjeldsen, R. Millan, L. Mayer, J. Mouginot, B. P. Y. Noël, C. O’Cofaigh, S. Palmer, S. Rysgaard, H. Seroussi, M. J. Siegert, P. Slabon, F. Straneo, M. R. van den Broeke, W. Weinrebe, M. Wood, and K. B. Zinglersen (2017). “BedMachine v3: Complete Bed Topography and Ocean Bathymetry Mapping of Greenland From Multibeam Echo Sounding Combined With Mass Conservation”. In: *Geophysical Research Letters* 44.21. DOI: `10.1002/2017GL074954` (cit. on pp. 1, 3, 20, 25).

Morlighem, Mathieu (2022). *IceBridge BedMachine Greenland, Version 5*. NASA National Snow and Ice Data Center Distributed Active Archive Center. DOI: `10.5067/GMEVBWFLWA7X` (cit. on pp. 45, 46, 49, 50, 55, 59).

Mouginot, Jeremie and Eric Rignot (2019). *Glacier Catchments/Basins for the Greenland Ice Sheet*. Version 1. Dryad. DOI: `10.7280/D1WT11` (cit. on pp. 26, 45, 46).

Nias, Isabel J., Sophie Nowicki, Denis Felikson, and Bryant Loomis (2023). “Modeling the Greenland Ice Sheet’s Committed Contribution to Sea Level During the 21st Century”. In: *Journal of Geophysical Research: Earth Surface* 128.2, e2022JF006914. DOI: `10.1029/2022JF006914` (cit. on pp. 3, 18, 63).

Nielsen, Lisbeth T., Guðfinna Aðalgeirsdóttir, Vasileios Gkinis, Roman Nuterman, and Christine S. Hvidberg (2018). “The Effect of a Holocene Climatic Optimum on the Evolution of the Greenland Ice Sheet during the Last 10 Kyr”. In: *Journal of Glaciology* 64.245, pp. 477–488. DOI: `10.1017/jog.2018.40` (cit. on pp. 43, 44, 47, 61, 62, 74).

Noël, B., W. J. Van De Berg, E. Van Meijgaard, P. Kuipers Munneke, R. S. W. Van De Wal, and M. R. Van Den Broeke (2015). “Evaluation of the Updated Regional Climate Model RACMO2.3: Summer Snowfall Impact on the Greenland Ice Sheet”. In: *The Cryosphere* 9.5, pp. 1831–1844. DOI: `10.5194/tc-9-1831-2015` (cit. on pp. 12, 47).

Noël, Brice, Willem Jan van de Berg, Stef Lhermitte, Bert Wouters, Nicole Schaffer, and Michiel R. van den Broeke (2018). “Six Decades of Glacial Mass Loss in the Canadian Arctic Archipelago”. In: *Journal of Geophysical Research: Earth Surface* 123.6, pp. 1430–1449. DOI: `10.1029/2017JF004304` (cit. on p. 47).

Noël, Brice, Willem Jan Van De Berg, Stef Lhermitte, and Michiel R. Van Den Broeke (2019). “Rapid Ablation Zone Expansion Amplifies North Greenland Mass Loss”. In: *Science Advances* 5.9, eaaw0123. DOI: `10.1126/sciadv.aaw0123` (cit. on pp. 21, 23, 33, 36, 37, 47, 74).

Nowicki, Sophie, Heiko Goelzer, Hélène Seroussi, Anthony J. Payne, William H. Lipscomb, Ayako Abe-Ouchi, Cécile Agosta, Patrick Alexander, Xylar S. Asay-Davis, Alice Barthel, Thomas J. Bracegirdle, Richard Cullather, Denis Felikson, Xavier Fettweis, Jonathan M. Gregory, Tore Hattermann, Nicolas C. Jourdain, Peter Kuipers Munneke, Eric Larour, Christopher M. Little, Mathieu Morlighem, Isabel Nias, Andrew Shepherd, Erika Simon, Donald Slater, Robin S. Smith, Fiammetta Straneo, Luke D. Trusel, Michiel R. Van Den Broeke, and Roderik Van De Wal (2020). "Experimental Protocol for Sea Level Projections from ISMIP6 Stand-Alone Ice Sheet Models". In: *The Cryosphere* 14.7, pp. 2331–2368. DOI: `10.5194/tc-14-2331-2020` (cit. on pp. 23, 43).

Nye, J. F. (1957). *Physical Properties of Crystals: Their Representation by Tensors and Matrices.* Oxford University Press (cit. on p. 7).

Nye, John Frederick and Max Ferdinand Perutz (1997). "The Distribution of Stress and Velocity in Glaciers and Ice-Sheets". In: *Proceedings of the Royal Society of London. Series A. Mathematical and Physical Sciences* 239.1216, pp. 113–133. DOI: `10.1098/rspa.1957.0026` (cit. on p. 22).

Oerlemans, J. (1981). "Some Basic Experiments with a Vertically-Integrated Ice Sheet Model". In: *Tellus* 33.1, pp. 1–11. DOI: `10.1111/j.2153-3490.1981.tb01726.x` (cit. on p. 14).

– (2003). "A Quasi-Analytical Ice-Sheet Model for Climate Studies". In: *Nonlinear Processes in Geophysics* 10.4/5, pp. 441–452. DOI: `10.5194/npg-10-441-2003` (cit. on pp. 2, 29, 71).

Olbers, Dirk and Hartmut Hellmer (2010). "A Box Model of Circulation and Melting in Ice Shelf Caverns". In: *Ocean Dynamics* 60.1, pp. 141–153. DOI: `10.1007/s10236-009-0252-z` (cit. on p. 13).

Pattyn, Frank (2003). "A New Three-Dimensional Higher-Order Thermomechanical Ice Sheet Model: Basic Sensitivity, Ice Stream Development, and Ice Flow across Subglacial Lakes". In: *Journal of Geophysical Research: Solid Earth* 108.B8. DOI: `10.1029/2002JB002329` (cit. on p. 10).

Payne, A. J., P. Huybrechts, A. Abe-Ouchi, R. Calov, J. L. Fastook, R. Greve, S. J. Marshall, I. Marsiat, C. Ritz, L. Tarasov, and M. P. A. Thomassen (2000). "Results from the EISMINT Model Intercomparison: The Effects of Thermomechanical Coupling". In: *Journal of Glaciology* 46.153, pp. 227–238. DOI: `10.3189/172756500781832891` (cit. on p. 23).

Peltier, W. R. (2004). "GLOBAL GLACIAL ISOSTASY AND THE SURFACE OF THE ICE-AGE EARTH: The ICE-5G (VM2) Model and GRACE". In: *Annual Review of Earth and Planetary Sciences* 32 (Volume 32, 2004), pp. 111–149. DOI: `10.1146/annurev.earth.32.082503.144359` (cit. on p. 74).

Peltier, W. R., P. Wu, and D. A. Yuen (1981). "The Viscosities of the Earth's Mantle". In: *Anelasticity in the Earth.* American Geophysical Union (AGU), pp. 59–77. DOI: `10.1029/GD004p0059` (cit. on p. 14).

Pollard, David, Won Chang, Murali Haran, Patrick Applegate, and Robert DeConto (2016). "Large Ensemble Modeling of the Last Deglacial Retreat of the West Antarctic Ice Sheet: Comparison of Simple and Advanced Statistical Techniques". In: *Geoscientific Model Development* 9.5, pp. 1697–1723. DOI: `10.5194/gmd-9-1697-2016` (cit. on p. 74).

Pollard, David, Robert M. DeConto, and Richard B. Alley (2015). "Potential Antarctic Ice Sheet Retreat Driven by Hydrofracturing and Ice Cliff Failure". In: *Earth and Planetary Science Letters* 412, pp. 112–121. DOI: `10.1016/j.epsl.2014.12.035` (cit. on p. 2).

Press, William H. and Glennys R. Farrar (1990). "Recursive Stratified Sampling for Multidimensional Monte Carlo Integration". In: *Computer in Physics* 4.2, pp. 190–195. DOI: `10.1063/1.4822899` (cit. on p. 72).

Rahmstorf, Stefan, Jason E. Box, Georg Feulner, Michael E. Mann, Alexander Robinson, Scott Rutherford, and Erik J. Schaffernicht (2015). "Exceptional Twentieth-Century Slowdown in Atlantic Ocean Overturning Circulation". In: *Nature Climate Change* 5.5, pp. 475–480. DOI: `10.1038/nclimate2554` (cit. on p. 2).

Ranganathan, Meghana and Brent Minchew (2024). "A Modified Viscous Flow Law for Natural Glacier Ice: Scaling from Laboratories to Ice Sheets". In: *Proceedings of the National Academy of Sciences* 121.23, e2309788121. DOI: `10.1073/pnas.2309788121` (cit. on p. 7).

Rantanen, Mika, Alexey Yu. Karpechko, Antti Lipponen, Kalle Nordling, Otto Hyvärinen, Kimmo Ruosteenoja, Timo Vihma, and Ari Laaksonen (2022). "The Arctic Has Warmed Nearly Four Times Faster than the Globe since 1979". In: *Communications Earth & Environment* 3.1, p. 168. DOI: `10.1038/s43247-022-00498-3` (cit. on pp. 2, 21).

Rasmussen, S. O., K. K. Andersen, A. M. Svensson, J. P. Steffensen, B. M. Vinther, H. B. Clausen, M.-L. Siggaard-Andersen, S. J. Johnsen, L. B. Larsen, D. Dahl-Jensen, M. Bigler, R. Röthlisberger, H. Fischer, K. Goto-Azuma, M. E. Hansson, and U. Ruth (2006). "A New Greenland Ice Core Chronology for the Last Glacial Termination". In: *Journal of Geophysical Research: Atmospheres* 111.D6. DOI: `10.1029/2005JD006079` (cit. on p. 43).

Raymo, Maureen E. and Peter Huybers (2008). "Unlocking the Mysteries of the Ice Ages". In: *Nature* 451.7176, pp. 284–285. DOI: `10.1038/nature06589` (cit. on p. 1).

Raymond, Charles F. (1983). "Deformation in the Vicinity of Ice Divides". In: *Journal of Glaciology* 29.103, pp. 357–373. DOI: `10.3189/S0022143000030288` (cit. on p. 10).

RGI Consortium (2023). *Randolph Glacier Inventory - A Dataset of Global Glacier Outlines, Version 7*. NASA National Snow and Ice Data Center Distributed Active Archive Center. DOI: `10.5067/F6JMOVY5NAVZ` (cit. on p. 45).

Robinson, Alexander, Daniel Goldberg, and William H. Lipscomb (2022). "A Comparison of the Stability and Performance of Depth-Integrated Ice-Dynamics Solvers". In: *The Cryosphere* 16.2, pp. 689–709. DOI: `10.5194/tc-16-689-2022` (cit. on p. 11).

Schoof, Christian (2006). "A Variational Approach to Ice Stream Flow". In: *Journal of Fluid Mechanics* 556, p. 227. DOI: `10.1017/S0022112006009591` (cit. on p. 22).

Schumacher, M, M A King, J Rougier, Z Sha, S A Khan, and J L Bamber (2018). "A New Global GPS Data Set for Testing and Improving Modelled GIA Uplift Rates". In: *Geophysical Journal International* 214.3, pp. 2164–2176. DOI: `10.1093/gji/ggy235` (cit. on pp. 3, 14, 55, 58, 59).

Seguinot, Julien (2013). "Spatial and Seasonal Effects of Temperature Variability in a Positive Degree-Day Glacier Surface Mass-Balance Model". In: *Journal of Glaciology* 59.218, pp. 1202–1204. DOI: `10.3189/2013JoG13J081` (cit. on p. 40).

Seneviratne, S.I., X. Zhang, M. Adnan, W. Badi, C. Dereczynski, A. Di Luca, S. Ghosh, I. Iskandar, J. Kossin, S. Lewis, F. Otto, I. Pinto, M. Satoh, S.M. Vicente-Serrano, M. Wehner, and B. Zhou (2021). "Weather and Climate Extreme Events in a Changing Climate". In: *Climate Change 2021: The Physical Science Basis. Contribution of Working Group I to the Sixth Assessment Report of the Intergovernmental Panel on Climate Change*. Ed. by V. Masson-Delmotte,

P. Zhai, A. Pirani, S.L. Connors, C. Péan, S. Berger, N. Caud, Y. Chen, L. Goldfarb, M.I. Gomis, M. Huang, K. Leitzell, E. Lonnoy, J.B.R. Matthews, T.K. Maycock, T. Waterfield, O. Yelekçi, R. Yu, and B. Zhou. Cambridge, United Kingdom and New York, NY, USA: Cambridge University Press, pp. 1513–1766. DOI: `10.1017/9781009157896.013` (cit. on pp. 2, 21, 34).

Shapiro, N (2004). "Inferring Surface Heat Flux Distributions Guided by a Global Seismic Model: Particular Application to Antarctica". In: *Earth and Planetary Science Letters* 223.1-2, pp. 213–224. DOI: `10.1016/j.epsl.2004.04.011` (cit. on pp. 22, 46, 74).

Slominska, E., W. Marczewski, and J. Slominski (2012). "Iceberg Tracking - SMOS over Antarctica". In: *2012 IEEE International Geoscience and Remote Sensing Symposium.* 2012 IEEE International Geoscience and Remote Sensing Symposium, pp. 4469–4472. DOI: `10.1109/IGARSS.2012.6350479` (cit. on p. 13).

Solgaard, Anne, Anders Kusk, John Peter Merryman Boncori, Jørgen Dall, Kenneth D. Mankoff, Andreas P. Ahlstrøm, Signe B. Andersen, Michele Citterio, Nanna B. Karlsson, Kristian K. Kjeldsen, Niels J. Korsgaard, Signe H. Larsen, and Robert S. Fausto (2021). "Greenland Ice Velocity Maps from the PROMICE Project". In: *Earth System Science Data* 13.7, pp. 3491–3512. DOI: `10.5194/essd-13-3491-2021` (cit. on pp. 3, 58).

Solgaard, Anne Munck and Anders Kusk (2023). *Greenland Ice Velocity from Sentinel-1 Edition 3.* Version 34. GEUS Dataverse. DOI: `10.22008/FK2/ZEGVXU` (cit. on p. 55).

Tabone, Ilaria, Alexander Robinson, Marisa Montoya, and Jorge Alvarez-Solas (2024). "Holocene Thinning in Central Greenland Controlled by the Northeast Greenland Ice Stream". In: *Nature Communications* 15.1, p. 6434. DOI: `10.1038/s41467-024-50772-5` (cit. on p. 75).

Tang, Boxin (1993). "Orthogonal Array-Based Latin Hypercubes". In: *Journal of the American Statistical Association* 88.424, pp. 1392–1397. DOI: `10.2307/2291282`. JSTOR: `2291282` (cit. on pp. 18, 51).

Tarantola, Albert (2005). *Inverse Problem Theory: And Methods for Model Parameter Estimation.* Philadelphia: SIAM, Society for Industrial and Applied Mathematics. 342 pp. (cit. on p. 15).

The IMBIE Team (2020). "Mass Balance of the Greenland Ice Sheet from 1992 to 2018". In: *Nature* 579.7798, pp. 233–239. DOI: `10.1038/s41586-019-1855-2` (cit. on pp. 1–3, 20, 23, 29, 33, 43, 57, 63, 78).

Vialov, SS (1958). "Regularization of Glacial Shields Movement and the Theory of Plastic Viscous Flow". In: *IAHS Publ. 47 (Symposium at Chamonix 1958, Physics of the Movement of the Ice).* (Cit. on p. 73).

Vinther, B. M., S. L. Buchardt, H. B. Clausen, D. Dahl-Jensen, S. J. Johnsen, D. A. Fisher, R. M. Koerner, D. Raynaud, V. Lipenkov, K. K. Andersen, T. Blunier, S. O. Rasmussen, J. P. Steffensen, and A. M. Svensson (2009). "Holocene Thinning of the Greenland Ice Sheet". In: *Nature* 461.7262, pp. 385–388. DOI: `10.1038/nature08355` (cit. on pp. 2, 3, 43, 44, 51, 52, 55, 60, 65, 73, 74).

Vinther, B. M., S. J. Johnsen, K. K. Andersen, H. B. Clausen, and A. W. Hansen (2003). "NAO Signal Recorded in the Stable Isotopes of Greenland Ice Cores". In: *Geophysical Research Letters* 30.7, 2002GL016193. DOI: `10.1029/2002GL016193` (cit. on p. 2).

Winkelmann, R., M. A. Martin, M. Haseloff, T. Albrecht, E. Bueler, C. Khroulev, and A. Levermann (2011). “The Potsdam Parallel Ice Sheet Model (PISM-PIK) – Part 1: Model Description”. In: *The Cryosphere* 5.3, pp. 715–726. DOI: `10.5194/tc-5-715-2011` (cit. on pp. 11, 14, 37, 46, 64).